The Rank-One Rotating Mass Matrix Hypothesis: a General and a Model Specific Study

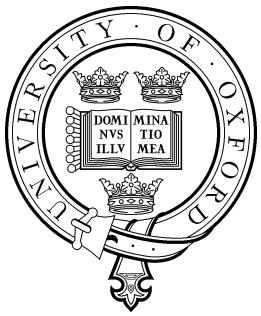

Michael J. Baker

St Cross College

University of Oxford

A thesis submitted for the degree of

Doctor of Philosophy

Hilary Term 2011

Acknowledgements

First and foremost I must acknowledge my supervisor, Tsou Sheung Tsun. She offered unabated guidance and support throughout, with as much patience as kindness. When faced with a problem which I could not approach she would show me, with precision and clarity, the path through the mist. I thank her; without her there would be no thesis.

I would also like to express my thanks to Chan Hong-Mo and José Bordes for many useful discussions on and around this work. Hong-Mo illuminated the background in which this project sits and offered much wisdom. I thank José for helping me maintain the connection between theoretical elegance and experimental reality.

My deepest gratitude goes to my family, especially my mother, whose love, belief and unbounded determination made this possible, my father, for his steadfast support, and Paul, for his efforts to make me think. I also thank my friends, in Oxford and beyond, for helping me maintain perspective. Without any of you I could not have started, let alone completed, this project.

The Rank-One Rotating Mass Matrix Hypothesis: a General and a Model Specific Study

Michael J. Baker

St Cross College
University of Oxford

A thesis submitted for the degree of
Doctor of Philosophy

Hilary Term 2011

In this thesis we investigate whether a rank-one rotating mass matrix extended to solve the strong CP problem can, through the mass leakage mechanism, account for fermion masses, mixing angles and a θ_{CP} term of order unity. In the first part we find restrictions placed on the rotation of the rank-one mass matrix by experimental data. We demonstrate that a smooth rotation of the mass matrix can reproduce the experimentally determined fermion masses and mixing angles and give $\theta_{CP} = 1.45$ radians. We then fit the speed of rotation at high (> 1 GeV) scales. Using this rotation we make predictions for Higgs branching ratios for a range of Higgs masses, finding a suppression of $\Gamma(H \to c\bar{c})$ compared to the standard model and significant flavour violating branching ratios.

In the second part we study the framed standard model (FSM). We calculate the strong framon one-loop contribution to the rotation of its rank-one mass matrix and account for the non-trivial metric on its internal symmetry space. We find that the FSM can reproduce the hierarchy seen in the fermion masses and the CKM matrix, fit $\theta_{CP} \sim 0.3$ radians and find $|U_{\mu 3}| \sim 0.8$. Similar results are found if QCD running is included, except that $|U_{\mu 3}| > 0.95$. We compare the FSM rotation to the rotation found in first part and find they are in good agreement above $\mu = m_c$. We go on to show that the predictions for Higgs decay are comparable to those found in the general study.

In the final part we calculate the framon mass spectrum of the FSM in the hermitian gauge and find that, as expected, it agrees with the calculation performed in the triangular gauge. We find that none of the framons are massless.

Contents

Chapter 1

Introduction

The standard model of particle physics is our best model of particle interactions on the smallest scales (i.e., excluding gravity). It has enjoyed unprecedented experimental confirmation. Measurements of the anomalous magnetic dipole moment show agreement between quantum electrodynamics, which is included in the standard model, and nature to within ten parts in a billion. The standard model has also withstood, without significant change, over 30 years of new experimental data. The only part of the standard model which has not been directly verified is the Higgs boson. The large hadron collider (LHC) will answer this final question in the next few years. However, despite this impressive record the standard model has many puzzling aspects which we would not expect in a fundamental theory of nature. Even though the standard model has no provision for the gravitational force or for dark matter there are still many internal inconsistencies that are not understood, e.g.:

- We would expect a fundamental theory to have one or possibly zero free parameters. The standard model has over 20 free parameters, most of which are related to fermion masses and mixing angles. The fermion masses (with the possible exception of the neutrinos) and the Cabibbo-Kobayashi-Maskawa (CKM) matrix show a hierarchical pattern which is not explained within the standard model.

- The masses of the gauge bosons, on the other hand, are predicted by the strengths of the coupling constants. This is directly related to the fact that the gauge bosons arise very naturally and geometrically within the standard model. The fermions and the scalar Higgs field are introduced in an *ad hoc* manner with no geometric basis.

- In the standard model there are three copies, or generations, of each of the fermion fields which differ only in their mass. Precision electroweak observables suggest that there are no more generations, but it is not understood why there are three.

- The standard model Lagrangian is almost the most general renormalisable gauge and Lorentz invariant Lagrangian you can write down. However, these conditions still admit the inclusion of a topological term containing the $su(3)$ gauge fields which would result in charge-conjugation parity (CP) violating effects which are not seen in experiment. Bounds from measurements of the neutral dipole moment force the coupling constant of this term to be unnaturally small. This is known as the strong CP problem.

- Baryon and lepton number is seen experimentally to be globally conserved. The standard model has no symmetry which explains this conservation, instead it is enforced by hand.

This thesis, which develops some ideas aimed at ameliorating these issues, falls naturally into three parts. The first part investigates the implication of a rank-one rotating fermion mass matrix. This is a general framework (i.e., one which does not specify an underlying quantum field theory (QFT)) which proposes an explanation for the hierarchy seen in the fermion masses and in the CKM matrix and may be extended to solve the strong CP problem.

The hierarchy of the fermion masses and the CKM matrix has inspired many people to investigate the possibility that the fermion mass matrix is rank-one (i.e., has only one non-zero eigenvalue) at tree level and receives extra contributions through loop diagrams. Harald Fritzsch took a nearly rank-one mass matrix as an ansatz and derived relations between fermion masses and mixing angles [16].

It is a well understood part of quantum field theory that the fermion mass parameters, the eigenvalues of the mass matrix, can run with scale. Tsou Sheung Tsun (TST) and Chan Hong-Mo (CHM) suggested that the eigenvectors of the fermion mass matrix may also depend on scale [7], and have further noted [9] that even in the standard model the eigenvectors of the mass matrix are scale dependent, though the effect is small enough that the dependence can be neglected. This does, however, raise the conceptual question as to how the fermion masses are defined when the eigenvectors depend on scale. In, e.g., the standard model the mass of a fermion is defined as the running mass at the scale of the mass, e.g., $m_t(172\text{ GeV}) = 172$

GeV for the top quark. TST and CHM proposed that the eigenvectors should also be taken at the scale of the fermion in question. This idea was combined with the rank-one suggestion and led them to study the rank-one rotating (i.e., scale dependent) mass matrix picture, for which they proposed the mass leakage mechanism. TST, CHM and José Bordes (JB) then developed these ideas in the framework of a phenomenological model, the dualized standard model (DSM) (see, e.g., [7]), but can be discussed independently of any model.

In the first part of this thesis we ask how well the rank-one rotating mass matrix picture can reproduce experimental data. Despite the fact that, since we are not here specifying an underlying QFT, there is a large amount of freedom it is not immediately clear that the scheme can match data. For instance, in surveying a range of similar attempts, Fritzsch concludes [17]:

> "We have given an overview of phenomenological studies of fermion mass and flavor mixing schemes. Particular attention has been paid to the underlying flavor symmetries which can lead to realistic textures of quark and lepton mass matrices.
>
> With the current experimental data on quark masses and flavor mixing angles, we find that only very few specific patterns of quark mass matrices are realistic."

In an attempt to introduce an approximate S_3 flavour symmetry, [21] finds good agreement to data but at the cost of increasing, not reducing as one would like, the number of free parameters. Previous work by TST, CHM and JB has shown that the mass leakage mechanism can match experimental data in the 2 generation approximation (i.e., ignoring the up quark, down quark, electron and lightest neutrino) [8] and in the full 3 generation picture [10]. Since this work it has been realised that the strong CP problem can be resolved in this scheme, and that the resolution introduces a CP violating phase in the CKM matrix [12]. We ask whether, with this extra step, the scheme can still match experimental data. Using the 2 generation approximation [8] it was found [13] that, under moderate assumptions regarding the Yukawa coupling, the rotating mass matrix scheme can make predictions about Higgs decay, which the authors go on to do for a representative Higgs mass of 150 GeV. In this thesis, once we match the scheme to experimental data, we go on to find similar predictions for Higgs decay branching ratios for a wide range of decay modes for a range of Higgs masses.

In the second part of this thesis we ask whether the framed standard model (FSM) [19], a specific quantum field theory which has a rank-one rotating mass matrix, could match experimental data. This model was motivated by the successes of the DSM, but rather than just a phenomenological model it is a fully fledged quantum field theory. The main assumption of the FSM is that the $u(1) \times su(2) \times su(3)$ gauge symmetry of the standard model should be matched to a global $\tilde{u}(1) \times \widetilde{su}(2) \times \tilde{su}(3)$ symmetry (where a tilde denotes a global symmetry). This assumption is motivated by the observation that there is no preferred reference frame in the internal space. The matrices representing the difference between the local configuration and the global frame are then promoted to fields, or so called framon fields. These fields transform as scalar fields under Lorentz transformations, so the scalar fields in this model are somewhat given a geometric basis. These framons, through this geometry, generate a metric on the global internal symmetry space, $\widetilde{su}(3)$. Once fermions are introduced this theory is very similar to the standard model with additional scalar fields. It is well known from Noether's theorem that every symmetry has a conserved quantity associated with it. The new global symmetries lead to baryon minus lepton number conservation and a 3 valued generation index. It is interesting that the FSM conserves baryon minus lepton number, and not baryon and lepton number individually. The same quantity is conserved in many grand unified theories. The FSM also has fewer free parameters than the standard model. It generates fermion mass ratios and mixing angles through the mass leakage mechanism which gives values determined by a smaller number of coupling constants.

We extract a renormalisation group equation (RGE) for the FSM mass matrix from the strong framon one-loop contribution to the fermion self energy. In a similar model [7] this provides the greatest contribution to the rotation. We only consider this term as it will contribute substantially to the rotation and can be thought of as a fairly general model for any heavy insertions in the self energy. Once we have found the RGE for the mass matrix, fixing the constants of integration at a certain scale determines the mass matrix rotation. Searching the parameter space of these constants of integration along with the coupling constants in the theory we attempt to match the theory to the experimental data. However, the mass leakage mechanism cannot be directly applied to the FSM. The non-trivial metric on the theory's internal symmetry space means that care has to be taken to properly define norms, inner products and cross products. We also consider the effect of QCD (quantum chromodynamics) running of the non-zero mass matrix eigenvalue. Once we have

searched the parameter space we consider the choice which gives the best agreement to experimental data and revisit the predictions for Higgs branching ratios.

In the final part of this thesis we explicitly calculate the framon mass spectrum in the hermitian gauge. This calculation has already been performed in the triangular gauge [2] and, as expected, the results are in agreement. Different gauge choices are more convenient for different calculations and it is useful, when possible, to check results in both gauges. None of the framons are massless, so the model is here not in direct disagreement with experiment. The framon which comes from the $\widetilde{su}(2)$ sector plays the role of the Higgs field. The other framons are assumed to be out of the energy reach of current experiments.

Part I

The Rank-One Rotating Mass Matrix Hypothesis: A General Study

Chapter 2

Rank-One Rotating Mass Matrices and the Strong CP Problem

In this chapter we define a rank-one rotating mass matrix and describe the mass leakage mechanism. We outline the strong CP problem and describe a resolution to this problem when one has a rank-one quark mass matrix.

2.1 Preliminaries

2.1.1 Fermion Mass Matrix

Since the notion of a rank-one rotating mass matrix and the mass leakage mechanism are not generally well known we will first offer an outline and introduce some notation. For a more detailed discussion of the steps see, e.g., [10, 19].

We will write the fermion mass terms in the Lagrangian as

$$\begin{aligned} \mathcal{L}_{\mathrm{M}} &= \overline{\Psi}_L m \Psi_R + h.c. \\ &= \overline{\Psi} P_R m P_R \Psi + \overline{\Psi} P_L m^\dagger P_L \Psi, \end{aligned} \tag{2.1}$$

where m is a 3×3 complex matrix, Ψ are spinor valued 3-vectors and $P_{R,L} = \frac{1}{2}(1 \pm \gamma_5)$ are chiral projection operators. We are free to redefine the right handed fields with unitary matrices,

$$P_R \Psi^0 = U P_R \Psi, \tag{2.2}$$

$$\overline{\Psi}^0 P_L = \overline{\Psi} P_L U^\dagger, \tag{2.3}$$

as they are singlets under $su(2)$.

Later it will be useful for us to write m as a hermitian matrix in a way which removes the projection operators from mass term, as is often done, e.g., by Weinberg

[33]. Note that a mass matrix can always be diagonalised by unitary transformations U and V, $UmV^{-1} = \Delta$. Since the eigenvalues of m are real and non-negative we can write

$$\begin{aligned}\Delta^2 &= \Delta\Delta^\dagger \\ &= UmV^{-1}V^{-1\dagger}m^\dagger U^\dagger \\ &= Umm^\dagger U^{-1}. \end{aligned} \tag{2.4}$$

Now we can define $m_W = mV^{-1}U$ so that $m_W = U^{-1}\Delta U$. We can then see that m_W is hermitian. Note that we also have $m_W^2 = m_W m_W^\dagger = mV^{-1}UU^{-1}Vm^\dagger = mm^\dagger$, so we can consider $m_W = \sqrt{mm^\dagger}$. We can then write

$$\begin{aligned}\overline{\Psi}_L m\Psi_R^0 + h.c. &= \overline{\Psi}P_R m P_R \Psi^0 + \overline{\Psi}^0 P_L m^\dagger P_L \Psi \\ &= \overline{\Psi}P_R m V^{-1}U P_R \Psi + \overline{\Psi}P_L U^{-1}V m^\dagger P_L \Psi \\ &= \overline{\Psi}P_R m_W P_R \Psi + \overline{\Psi}P_L m_W^\dagger P_L \Psi \\ &= \overline{\Psi}P_R m_W P_R \Psi + \overline{\Psi}P_L m_W P_L \Psi \\ &= \overline{\Psi}m_W P_R \Psi + \overline{\Psi}m_W P_L \Psi \\ &= \overline{\Psi}m_W \Psi, \end{aligned} \tag{2.5}$$

where we have written $P_R\Psi^0 = V^{-1}UP_R\Psi$.

2.1.2 Rotating Mass Matrix

In the standard model the fermion masses depend on scale, or 'run'. A rotating mass matrix is one whose eigenvectors, as well as its eigenvalues, depend on scale. We will here recall the argument given in [9] that even in the standard model the eigenvectors will not be constant. In [14] it is shown that the matrix of Yukawa couplings, e.g., for the up-type quarks, M_U, has a renormalisation group equation containing non-diagonal terms,

$$(4\pi)^2 \frac{dM_U(t)}{dt} = -\frac{3}{2}M_D M_D^\dagger M_U + \ldots. \tag{2.6}$$

These contributions are not diagonal since the CKM matrix is found to be different to the identity. Since the left handed up-type and down-type quarks are in the same $su(2)$ doublet, we cannot simultaneously diagonalise the up-type and down-type quark mass matrices. So even if M_U were diagonal at a particular scale then it would not remain diagonal as the scale changes. We call this effect 'rotation'. This effect is

usually neglected in the standard model as the CKM matrix is quite close to the identity matrix, resulting in a slow rotation. Nonetheless, the question remains of defining what one means by mass eigenstates when the mass matrix rotates.

2.1.3 Rank-One Rotating Mass Matrix

A rank-one matrix has one non-zero eigenvalue and can be generated by an outer product of the eigenvector associated with this eigenvalue with itself. The mass matrix itself, when diagonalised, will only have one non-zero entry. This is already quite a good approximation to the actually situation seen in the quark and charged lepton sector, where $m_u \ll m_c \ll m_t$; $m_d \ll m_s \ll m_b$; $m_e \ll m_\mu \ll m_\tau$. The rotation of the mass matrix can then be described entirely by the rotation of one eigenvector. For three generations this can be described by six parameters; one length, two angles and three phases. In general there is no relation between the mass matrices of different types, i.e., that for the up-type quarks, the down-type quarks, the charged leptons and the neutrinos. However, we will find that we can accommodate the experimental data by assuming that while the non-zero eigenvalue depends on the type the rotating eigenvector does not.

2.1.4 Mass Leakage Mechanism

If the mass matrix rotates with scale then the definition of masses and mixing angles needs to be made more precise. The mass leakage mechanism provides such a framework. Although the mechanism can be described for an arbitrary mass matrix (not only a rank-one matrix) [10] and a general number of fermions, n, we will here discuss the case where $n = 3$ and the mass matrix is rank-one. This means that for the up-type quarks the mass matrix can be represented as the outer product of a single vector with itself,

$$m_W = m_U \boldsymbol{\alpha}\boldsymbol{\alpha}^\dagger, \tag{2.7}$$

where m_U is the non-vanishing eigenvalue of m_W and $\boldsymbol{\alpha}$ is its normalised eigenvector. We will write m_D for the down-type quarks. We shall here assume that only $\boldsymbol{\alpha}$ changes under renormalisation, not the eigenvalue m_U. In part II we shall relax this assumption. When a particle's mass depends on scale it is usual to define its mass at a scale equal to the mass itself. In the mass leakage mechanism this convention is generalised to apply to the state vector too. The state vector of the top quark, $\mathbf{v}_t$, is defined as the massive eigenvector at the scale of the top quark, $\mathbf{v}_t = \boldsymbol{\alpha}(\mu = m_t)$.

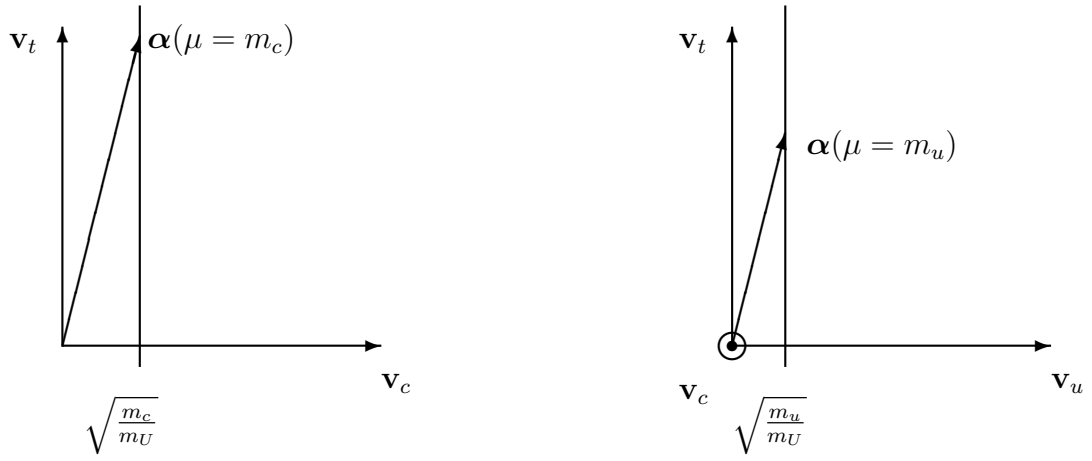

Figure 2.1: On the left (a), the situation at $\mu = m_c$. The vector $\boldsymbol{\alpha}$ has rotated away from $\mathbf{v}_t$. The state vector $\mathbf{v}_c$ is defined parallel to $\text{proj}_{\mathbf{v}_t^\perp}(\boldsymbol{\alpha}_c)$. There is a non-zero projection of $\boldsymbol{\alpha}$ onto $\mathbf{v}_c$. On the right (b), a similar situation occurs when the scale reduces to $\mu = m_u$. $\mathbf{v}_c$ points into the page.

We will denote $\boldsymbol{\alpha}(\mu = m_i)$ by $\boldsymbol{\alpha}_i$. The eigenvalue of the mass matrix at this scale will then give the top quark mass, so $m_U = m_t$. We then run the scale to the mass of the charm quark. The eigenvector $\boldsymbol{\alpha}$ will in general rotate away from the vector $\mathbf{v}_t$ (see figure 2.1a for a schematic picture). The mass leakage mechanism now gives us a way of defining $\mathbf{v}_c$. The particle state vectors $\mathbf{v}_t$ and $\mathbf{v}_c$ must be orthogonal, since otherwise the CKM matrix would not be unitary, but the eigenvector $\boldsymbol{\alpha}_c$ need not be orthogonal to $\mathbf{v}_t$. The mass leakage mechanism takes the charm quark state vector to lie in the subspace orthogonal to $\mathbf{v}_t$ in the direction of $\boldsymbol{\alpha}_c$, i.e., $\mathbf{v}_c \parallel \text{proj}_{\mathbf{v}_t^\perp}(\boldsymbol{\alpha}_c)$. At $\mu = m_c$ the charm quark state vector, $\mathbf{v}_c$, has a component in the direction of the massive eigenvector $\boldsymbol{\alpha}_c$. The particle state acquires some mass via a 'leakage' from the heavy state at $\mu = m_c$, even though it was massless at $\mu = m_t$. One can think of an effective $\boldsymbol{\alpha}^{\text{eff}} \in \mathbf{v}_t^\perp$, $\boldsymbol{\alpha}^{\text{eff}} = \text{proj}_{\mathbf{v}_t^\perp}(\boldsymbol{\alpha})$. This $\boldsymbol{\alpha}^{\text{eff}}$ will correspond to the eigenvector of a 2×2 rank-one matrix, whose eigenvalue at $\mu = m_c$ will be m_c. We then follow a similar procedure to define $\mathbf{v}_u$, i.e., $\mathbf{v}_u \parallel \text{proj}_{\mathbf{v}_t^\perp \cap \mathbf{v}_c^\perp}(\boldsymbol{\alpha}_u)$, figure 2.1b. This process may be understood physically in the following terms: above $\mu = m_t$ all three particles may be created; in the region $m_c < \mu < m_t$ the up and charm quarks can be created but the top quark degree of freedom cannot be excited, restricting possible states to a subspace orthogonal to $\mathbf{v}_t$; for $\mu < m_c$ only the up quark may be excited and the possible states are restricted to the subspace $\mathbf{v}_t^\perp \cap \mathbf{v}_c^\perp$.

Following this scheme and equation (2.7) the masses of the up-type quarks are

given by

$$m_t = m_U, \tag{2.8}$$

$$m_c = m_U|\boldsymbol{\alpha}_c \cdot \mathbf{v}_c|^2, \tag{2.9}$$

$$m_u = m_U|\boldsymbol{\alpha}_u \cdot \mathbf{v}_u|^2. \tag{2.10}$$

In what follows we shall assume that the phases in $\boldsymbol{\alpha}$ do not change with scale. Then, since the masses and mixing angles depend only on the inner products of $\boldsymbol{\alpha}$ and the state vectors, the phases will cancel out of all the quantities of interest. This allows us to take $\boldsymbol{\alpha}$ and the state vectors to be vectors in $\mathbb{R}^3$. Also, as the rotation of $\boldsymbol{\alpha}$ will be driven by some renormalisation group equation we will be interested in finding a smooth trajectory. These properties have been seen in specific models [7, 19] that have been constructed. Although in these models all particle types share the same trajectory, this is not necessary in general. We find, however, that we can well accommodate all particle types on the same trajectory. For this reason we will assume this universality of the trajectory.

2.2 The Strong CP Problem

Previous work has shown that the mass leakage mechanism can accommodate realistic fermion mass and mixing angles. Recent work [3, 11] has suggested a solution to the strong CP problem within the rank-one rotating mass matrix scheme. This approach alters the definition of the CKM matrix. Here we will detail the effect and go on to investigate whether realistic fermion masses and mixing angles can still be accommodated. First we will outline the strong CP problem and its solution, as given in [12]. There is no symmetry which forbids the following renormalisable topological term in the QCD Lagrangian:

$$\mathcal{L}_{\theta_{CP}} = -\frac{\theta_{CP}}{64\pi^2}\epsilon^{\mu\nu\rho\sigma}F_{\mu\nu}F_{\rho\sigma}, \tag{2.11}$$

where $F_{\mu\nu}$ is the $su(3)$ field strength tensor and θ_{CP} is a fundamental coupling constant naturally of order unity. If CP were not conserved there would be a non-zero amplitude for the π^0 to disappear into the vacuum, proportional to m_π^2. This implies that the neutron electric dipole moment, d_n, should be, on dimensional grounds,

$$d_n \sim \frac{|\theta_{CP}|em_\pi^2}{\Lambda_{QCD}^3} \sim 10^{-16}|\theta_{CP}|e \text{ cm}, \tag{2.12}$$

where Λ_{QCD} is the typical QCD mass scale [32]. The most sensitive experiments have found $d_n < 2.9 \times 10^{-26} e$ cm [24], meaning that $|\theta_{CP}| < 3 \times 10^{-10}$. The fine tuning involved in fixing $|\theta_{CP}| < 3 \times 10^{-10}$ is the strong CP problem.

If we redefine the fermion fields,

$$\psi_f \to e^{i\gamma_5 \theta_f} \psi_f, \tag{2.13}$$

where f is a flavour index and θ_f are real constants, then the measure for path integrals over fermion fields changes to

$$\mathcal{D}\psi\mathcal{D}\overline{\psi} \to \exp\left(\frac{-i}{32\pi^2}\int d^4x\ \epsilon_{\mu\nu\rho\sigma}\mathrm{Tr}(H^{\mu\nu}H^{\rho\sigma})\sum_f \theta_f\right)\mathcal{D}\psi\mathcal{D}\overline{\psi}, \tag{2.14}$$

where $H^{\mu\nu}$ is the $su(3)$ field strength tensor and $\epsilon_{\mu\nu\rho\sigma}$ is the totally anti-symmetric tensor. Comparing this to the topological term, equation (2.11), shows that the redefinition is equivalent to shifting

$$\theta_{CP} \to \theta_{CP} + 2\sum_f \theta_f. \tag{2.15}$$

A field redefinition is equivalent to a shift in θ_{CP}. We can chose choose $2\sum_f \theta_f = -\theta_{CP}$ and explicitly remove the topological term from the Lagrangian. This redefinition has no effect on the kinetic terms in the Lagrangian. However, it does shift the mass parameters of the fermions,

$$\overline{\psi}_L m \psi_R + h.c. \to \overline{\psi}_L e^{2i\theta_f} m_f \psi_R + h.c. \tag{2.16}$$

In general the mass parameters become complex. This has the effect of reintroducing CP violation: as expected, a field redefinition does not change the physics. However, if any of the fermions are massless, then this procedure can be followed and the term (2.11) rendered physically irrelevant. This solution to the strong CP problem has been known for a long time, but since all of the quarks have been found to have non-zero mass this redefinition cannot be implemented. A favoured solution is to add a new spontaneously broken global symmetry to the standard model which naturally removes the strong CP problem and results in a new particle, the axion [26, 34]. However, the axion has not been discovered despite many experimental searches. Recent theoretical work has also suggested that its presence may cause a cosmological fine tuning problem as severe as the strong CP problem itself [23]. These tensions provide a good motivation for re-examining the most straightforward solution.

2.2.1 Absorbing θ_{CP}

The transformation introduced above is chiral, whereas in our discussion of the mass leakage mechanism we described state vectors of indefinite chirality. In most of what follows we will be interested in fermion masses and the CKM matrix. Since the CKM matrix involves only the left handed fields we can, and will, consider only the left handed part of the state vectors. This allows us to make the replacement

$$e^{i\gamma_5\theta_f} \to e^{i\theta_f}. \tag{2.17}$$

This is adequate for our present purposes, but we will have to make allowances for this simplification when we discuss Higgs decay.

In the rank-one rotating mass matrix scheme there are, at every scale, two independent massless directions. At a given scale any chiral transformation in this plane will keep the mass matrix hermitian and can absorb the CP violating term. However, the motion of $\boldsymbol{\alpha}$ in an explicit model will be generated by an RGE. The massless plane orthogonal to $\boldsymbol{\alpha}$ will rotate continuously from $\boldsymbol{\alpha}(\mu)$ to $\boldsymbol{\alpha}(\mu + d\mu)$. To ensure that no mass parameters become complex under infinitesimal changes in scale the chiral transformation is made along the line that lies within both of these planes, figure 2.2. We set up a Darboux triad at every scale consisting of the radial vector $\boldsymbol{\alpha}(\mu)$, the tangent vector $\boldsymbol{\tau}(\mu) \,||\, \dot{\boldsymbol{\alpha}}(\mu)$ and the normal vector $\boldsymbol{\nu}(\mu)$ orthogonal to both. The vector $\boldsymbol{\nu}(\mu)$ then lies orthogonal to both $\boldsymbol{\alpha}(\mu)$ and $\boldsymbol{\alpha}(\mu + d\mu)$ in the limit $d\mu \to 0$. Effecting the chiral transformation in the $\boldsymbol{\nu}(\mu)$ direction then ensures hermiticity of the mass matrix at every scale.

Explicitly, we choose a reference frame where

$$\boldsymbol{\alpha}_0 = \boldsymbol{\alpha}(\mu = \infty) = (1, 0, 0)^\dagger, \tag{2.18}$$
$$\boldsymbol{\tau}_0 = \boldsymbol{\tau}(\mu = \infty) = (0, 1, 0)^\dagger, \tag{2.19}$$
$$\boldsymbol{\nu}_0 = \boldsymbol{\nu}(\mu = \infty) = (0, 0, 1)^\dagger, \tag{2.20}$$

figure 2.3a, and then define a rotation $A(\mu)$ such that

$$\boldsymbol{\alpha}(\mu) = A(\mu)\,\boldsymbol{\alpha}_0, \tag{2.21}$$
$$\boldsymbol{\tau}(\mu) = A(\mu)\,\boldsymbol{\tau}_0, \tag{2.22}$$
$$\boldsymbol{\nu}(\mu) = A(\mu)\,\boldsymbol{\nu}_0, \tag{2.23}$$

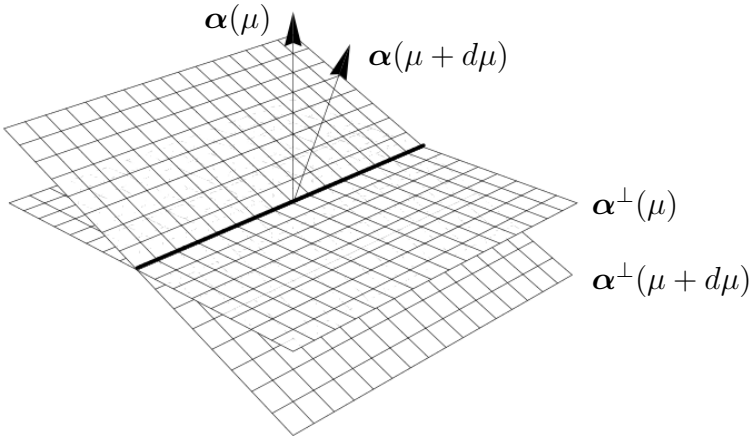

Figure 2.2: The bold line lies orthogonal to both $\boldsymbol{\alpha}(\mu)$ and $\boldsymbol{\alpha}(\mu + d\mu)$. The chiral transformation is performed on this linear combination of quark fields at scale μ.

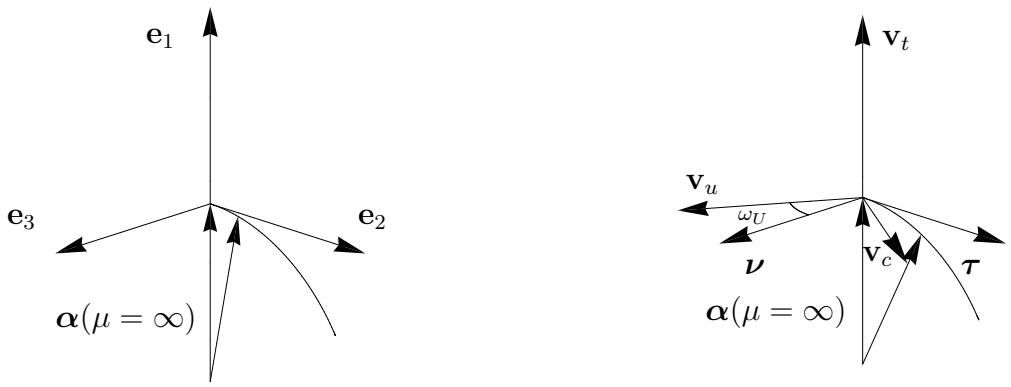

Figure 2.3: On the left (a), we choose a reference frame in terms of $\boldsymbol{\alpha}(\mu)$, equations (2.18) to (2.20). On the right (b), the up-type quark state vector triad and the Darboux triad transported with $A_t^{-1}$to $\mu = \infty$. They are related by a rotation of ω_U in the $\mathbf{e}_2$-$\mathbf{e}_3$ plane, equation (2.28).

where later we will write $A(\mu = m_x)$ as A_x. To effect the chiral transformation in the $\boldsymbol{\nu}(\mu)$ direction we would then want to act on a vector of quark fields with

$$\begin{aligned} P(\mu) &= A(\mu) P_0 A^{-1}(\mu), & (2.24) \\ P_0 &= \begin{pmatrix} 1 & 0 & 0 \\ 0 & 1 & 0 \\ 0 & 0 & e^{-i\theta_{CP}/2} \end{pmatrix}. & (2.25) \end{aligned}$$

If we consider the up-type quarks for a moment, we have already described how the state vector of the top quark is given by $\boldsymbol{\alpha}$ at the scale of the top quark, $\mathbf{v}_t = \boldsymbol{\alpha}(\mu = m_t)$, and that $\mathbf{v}_c$ and $\mathbf{v}_u$ are orthogonal to both $\mathbf{v}_t$ and to each other. At $\mu = m_t$ we thus have that $\boldsymbol{\tau}$ and $\boldsymbol{\nu}$ lie in the same plane as $\mathbf{v}_c$ and $\mathbf{v}_u$, and so the Darboux triad must be related to the state vector triad by a rotation in this plane,

$$\begin{aligned} A_t^{-1} \boldsymbol{\tau}_U &= \Omega_U A_t^{-1} \mathbf{v}_c, & (2.26) \\ A_t^{-1} \boldsymbol{\nu}_U &= \Omega_U A_t^{-1} \mathbf{v}_u, & (2.27) \\ \Omega_U &= \begin{pmatrix} 1 & 0 & 0 \\ 0 & \cos\omega_U & -\sin\omega_U \\ 0 & \sin\omega_U & \cos\omega_U \end{pmatrix}. & (2.28) \end{aligned}$$

Here ω_U is just the angle between $\boldsymbol{\nu}$ and $\mathbf{v}_u$, figure 2.3b. Following [12] we find that the CKM matrix is given by

$$V_{\mathrm{CKM}} = (\Omega_U^{-1} P_0 \Omega_U) V (\Omega_D^{-1} P_0^{-1} \Omega_D), \tag{2.29}$$

where $V = \Omega_U^{-1} A_t^{-1} A_b \Omega_D$ is just the orthogonal matrix relating the real up and down quark state triads. V_{CKM} is independent of scale, as expected. For given V, ω_U and ω_D the experimental limits on the Jarlskog invariant can then be used to fix θ_{CP}.

In this picture [12] argues that, e.g., the charm quark mass is given by

$$\begin{aligned} m_c &= m_U \overline{\Psi} P(m_c) \mathbf{v}_c \mathbf{v}_c^\dagger \boldsymbol{\alpha}(m_c) \boldsymbol{\alpha}^\dagger(m_c) \mathbf{v}_c \mathbf{v}_c^\dagger P(m_c) \Psi \\ &= m_U |\boldsymbol{\alpha}_c \cdot \mathbf{v}_c|^2 \overline{\Psi} P(m_c) \mathbf{v}_c \mathbf{v}_c^\dagger P(m_c) \Psi \\ &= m_U |\boldsymbol{\alpha}_c \cdot \mathbf{v}_c|^2 |\overline{\Psi}_c(\mu = m_c)|^2 \\ &= m_U |\boldsymbol{\alpha}_c \cdot \mathbf{v}_c|^2. \end{aligned} \tag{2.30}$$

The fermion masses formulae, (2.8) to (2.10), are unaltered by this chiral transformation.

Within this framework the assumption that the phases in $\boldsymbol{\alpha}$ do not change with scale is equivalent to assuming that all CP violating effects in the CKM matrix come from the strong theta-angle term in the manner set out above.

The leptonic sector should be considered analogously. However, it is not known whether neutrino oscillations violate CP symmetry. It is also not known if neutrinos are Majorana particles, which would cause extra phases to enter the PMNS matrix. As experiments so far have nothing to say about these points, and very little is known about neutrino masses, we do not consider the neutrinos in this part.

Chapter 3

Modelling the Trajectory of $\alpha(\mu)$ to Fit Experimental Constraints

In this chapter we present the experimental values we used along with their associated experimental and theoretical uncertainties. We discuss the methods we use to place constraints, coming from the experimental data, on the mass matrix rotation and how we automated the search to find a 'best fit' trajectory [4]. We then present the 'best fit' trajectory and model the speed of rotation with scale, which we use in the next chapter to make predictions for Higgs decay.

3.1 Experimental Data

The experimental data used was taken from the particle data group [1] and is summarised below:

$$m_t = 171.3 \pm 1.1 \pm 1.2 \text{ GeV}, \tag{3.1}$$
$$m_c = 1.27^{+0.07}_{-0.11} \text{ GeV}, \tag{3.2}$$
$$m_u = 1.5 \text{ to } 3.3 \text{ MeV } (2 \text{ GeV}), \tag{3.3}$$

$$m_b = 4.20^{+0.17}_{-0.07} \text{ GeV } (\overline{\text{MS}}), \tag{3.4}$$
$$m_s = 105^{+25}_{-35} \text{ MeV } (2 \text{ GeV}), \tag{3.5}$$
$$m_d = 3.5 \text{ to } 6.0 \text{ GeV } (2 \text{ GeV}), \tag{3.6}$$

$$m_\tau = 1.78 \text{ GeV}, \tag{3.7}$$

$$m_\mu = 106 \text{ MeV}, \tag{3.8}$$

$$m_e = 0.511 \text{ MeV}, \tag{3.9}$$

$$|V_{\text{CKM}}| = \begin{pmatrix} 0.97419 \pm 0.00022 & 0.2257 \pm 0.0010 & 0.00359 \pm 0.00016 \\ 0.2256 \pm 0.0010 & 0.97334 \pm 0.00023 & 0.0415^{+0.0010}_{-0.0011} \\ 0.00874^{+0.00026}_{-0.00037} & 0.0407 \pm 0.0010 & 0.999133^{+0.000044}_{-0.000043} \end{pmatrix}, \tag{3.10}$$

$$J = 3.05^{+0.19}_{-0.20} \times 10^{-5}. \tag{3.11}$$

Due to the confining nature of the strong force it is not possible to observe free quarks. This leads to difficulties not only in experimentally determining the masses but also in theoretically defining exactly what this mass means. The standard QCD Lagrangian requires renormalisation to yield finite amplitudes for physical process. The renormalisation necessarily introduces a dimensionful scale parameter, μ. The masses occurring in the Lagrangian depend both on μ and on the renormalisation scheme. Here we shall discuss results relating the the commonly used $\overline{\text{MS}}$ scheme.

The chiral symmetry breaking of the QCD Lagrangian has a scale of around 1 GeV. Above this scale explicit chiral symmetry breaking dominates whereas below spontaneous chiral symmetry breaking is the more important effect. We will call a quark heavy if its mass is greater than 1 GeV (c, b and t are heavy quarks), and light if not (u, d and s). We will consider these two types of quark separately.

The top quark decays before it can hadronise so its mass can easily be measured by its decay products. The mass of the bottom quark can be well estimated by heavy quark effective theory (HQET) simulations and perturbative theoretical calculations. HQET considers hadrons containing one light quark and one heavy quark. The heavy quark is considered as a static source for the gluon field. Perturbative calculations expand in $\alpha_s(m_b)$, the strong coupling constant, with non-perturbative corrections in Λ_{QCD}/m_b. The charm quark is too light to be accurately modelled by HQET and heavy enough to give significant lattice artifacts in lattice gauge theory. Recent quenched lattice gauge theory simulations have resulted in the value we take, but it is expected that this result will be improved upon by future simulations.

For the light quarks chiral perturbation theory can be used to determine quark mass ratios. The breaking of the chiral symmetry leads to eight Goldstone bosons, the π's, the K's and η. These bosons are massless in the massless quark limit. As

the quarks are massive this symmetry is only approximate so the Goldstone bosons acquire some mass, which can be written as explicit functions of the quark masses. The π, K and η, being colourless and so free, have well measured masses. As long as the renormalisation scheme is invariant under a chiral transformation, which is true for the $\overline{\text{MS}}$ scheme, then this method gives the mass ratios of the light quarks in that scheme. These ratios are then independent of the renormalisation scale and, by one loop calculations, have an accuracy of around 25%. The absolute values of the masses are estimated using lattice gauge theory, which also has significant errors. These large uncertainties mean that we have to be cautious in overinterpreting any results which depend on the light quarks. For the majority of this thesis we ignore the up and down quarks. The strange quark has a mass approaching the chiral symmetry breaking scale so we include it on the same footing as the heavy quarks whilst recognising that any results should be interpreted with care.

The CKM matrix, a unitary matrix which describes the mismatch between quark mass eigenstates and weak flavour eigenstates, is a very well measured quantity. The matrix has complex entries but the absolute values of each of the elements is given above. Some experiments measure the absolute values of the elements of the CKM matrix, such as the determination of $|V_{ud}|$ from nuclear beta decays. Other experiments, such as measurements of Kaon mixing, determine the degree of CP violation seen in nature. The Jarlskog invariant [20] gives a convenient, parameterisation independent way of describing the amount of CP violation. It is defined as

$$J = \sum_{m,n} \epsilon_{ikm}\epsilon_{jln}\text{Im}\left[V_{ij}V_{kl}V_{il}^{*}V_{kj}^{*}\right], \tag{3.12}$$

where V_{ij} is an element of the CKM matrix and ϵ_{ijk} is the Levi-Civita symbol.

The charged leptons have very well measured masses. The neutrinos, however, only interact via the weak nuclear force so their properties are more difficult to measure. In its original form the standard model assumed that the neutrinos were massless. Recent experiments have demonstrated neutrino oscillation, which implies that at least two of the neutrinos must be massive. The origin of neutrino mass in the standard model has not yet been determined. If they acquire mass through interaction with a Higgs field then this would predict the existence of right handed neutrinos, which have not been detected. Since neutrinos are singlets under $u(1)$, $su(2)$ and $su(3)$ they could also acquire mass via a Majorana mass term. Both of these mechanisms leave open the question as to why the neutrinos are so light. Various see-saw mech-

anisms have been proposed to explain this, pairing the light left handed neutrinos with heavy right handed neutrinos.

Neutrino oscillation experiments can determine mass squared differences between the neutrinos, $\Delta m^2_{ij} = |m^2_{\nu_i} - m^2_{\nu_j}|$:

$$\Delta m^2_{12} = 8.0^{+0.6}_{-0.4} \times 10^{-5} \text{ eV}^2, \tag{3.13}$$

$$\Delta m^2_{23} = 2.4^{+0.6}_{-0.5} \times 10^{-3} \text{ eV}^2. \tag{3.14}$$

Since only the mass differences have been measured and the two mass differences are quite different there can be two types of hierarchy. Either there are two light neutrinos and one heavier ('normal' hierarchy), or two heavier neutrinos and one lighter ('inverted' hierarchy). Current experiments do not distinguish between these two scenarios. Various direct [22] and indirect [25] experiments give an upper bound on neutrino masses around 2 eV.

The PMNS lepton mixing matrix can be parameterised

$$U_{\text{PMNS}} = \begin{pmatrix} c_{12}c_{13} & s_{12}c_{13} & s_{13}e^{-i\delta} \\ -s_{12}c_{23} - c_{12}s_{23}s_{13}e^{i\delta} & c_{12}c_{23} - s_{12}s_{23}s_{13}e^{-i\delta} & s_{23}c_{13} \\ s_{12}s_{23} - c_{12}c_{23}s_{13}e^{i\delta} & -c_{12}s_{23} - s_{12}c_{23}s_{13}e^{i\delta} & c_{23}c_{13} \end{pmatrix} \times \tag{3.15}$$

$$\times \begin{pmatrix} e^{i\alpha_1/2} & 0 & 0 \\ 0 & e^{i\alpha_2/2} & 0 \\ 0 & 0 & 1 \end{pmatrix}, \tag{3.16}$$

where c_{12} denotes $\cos\theta_{12}$, etc. The phases α_1 and α_2 are non-zero only if neutrinos have Majorana mass terms. Experiments have placed the following constraints on the angles:

$$\sin^2(\theta_{13}) < 0.032, \tag{3.17}$$

$$\tan^2(\theta_{12}) = 0.47^{+0.06}_{-0.05}, \tag{3.18}$$

$$\sin^2(2\theta_{23}) > 0.86, \tag{3.19}$$

where the bounds are given at 1 σ. There are no constraints on the phases. We performed some preliminary studies to see how strong the constraints from this data were. We made several reasonable assumptions for the neutrino masses, e.g., taking the normal hierarchy and $m_{\nu_3} = \sqrt{\Delta m^2_{23}}$, so that

$$m_{\nu_1} = 0.001 \text{ eV}, \tag{3.20}$$

$$m_{\nu_2} = 0.009 \text{ eV}, \tag{3.21}$$

$$m_{\nu_3} = 0.05 \text{ eV}. \tag{3.22}$$

We found that the data weakly constrains the trajectory, so we did not use the neutrino data in placing constraints on the possible trajectories of $\boldsymbol{\alpha}$.

3.2 Inverting the Mass Leakage Mechanism

The mass leakage scheme has $\boldsymbol{\alpha}$ as a fundamental object and the state vectors are derived from this. Here, however, we will start from real orthonormal state vectors and use experimental data to find a consistent trajectory of $\boldsymbol{\alpha}$. We first choose the up-type quarks to have state vectors

$$\mathbf{v}_u = (1,\ 0,\ 0)^\dagger, \tag{3.23}$$

$$\mathbf{v}_c = (0,\ 1,\ 0)^\dagger, \tag{3.24}$$

$$\mathbf{v}_t = (0,\ 0,\ 1)^\dagger, \tag{3.25}$$

which we are free to do. Given the orthogonal matrix relating the real up and down quark state triads, V, we can define the down-type quark state vectors, $\mathbf{v}_{d,s,b} = V\mathbf{v}_{u,c,t}$. There are no explicit physical constraints on the matrix V so we are free to choose any orthogonal matrix. However, there are implicit constraints on V. If there were no contribution from the θ_{CP} phase then V would be the CKM matrix. Since the CKM matrix is close to the identity the non-planarity of the trajectory, and so $\omega_{U,D}$, will be small. We thus expect to find a V which is 'near' to the CKM matrix.

We can fix the position of $\boldsymbol{\alpha}$ at the scale of the top quark easily since $\boldsymbol{\alpha}(\mu = m_t) = \mathbf{v}_t$, and similarly $\boldsymbol{\alpha}(\mu = m_b) = \mathbf{v}_b$. The leakage mechanism then fixes $\boldsymbol{\alpha}_c$ and $\boldsymbol{\alpha}_s$ in terms of the quark masses:

$$\boldsymbol{\alpha}_c = \sqrt{m_c/m_t}\ \mathbf{v}_c + \sqrt{1 - m_c/m_t}\ \mathbf{v}_t, \tag{3.26}$$

$$\boldsymbol{\alpha}_s = \sqrt{m_s/m_b}\ \mathbf{v}_s + \sqrt{1 - m_s/m_b}\ \mathbf{v}_b. \tag{3.27}$$

The two vectors $\mathbf{v}_t$ and $\mathbf{v}_c$ define a plane. All that the mass ratio m_u/m_t tell us about $\boldsymbol{\alpha}_u$ is the angle which it makes with this plane. We can thus restrict $\boldsymbol{\alpha}_u$, and similarly $\boldsymbol{\alpha}_d$, to lie somewhere on a line, parameterised by $x \in [0,\ 2\pi)$:

$$\boldsymbol{\alpha}_u = \sqrt{m_u/m_t}\ \mathbf{v}_u + \sqrt{1-m_u/m_t}\ \mathbf{v}_c \cos(x) + \sqrt{1-m_u/m_t}\ \mathbf{v}_t \sin(x), \tag{3.28}$$

$$\boldsymbol{\alpha}_d = \sqrt{m_d/m_b}\ \mathbf{v}_d + \sqrt{1-m_d/m_b}\ \mathbf{v}_s \cos(x) + \sqrt{1-m_d/m_b}\ \mathbf{v}_b \sin(x), \tag{3.29}$$

where we will choose the signs of the square roots so that $\boldsymbol{\alpha}_{u,d}$ has a positive projection onto $\mathbf{v}_{u,d}$. The restrictions on $\boldsymbol{\alpha}_i$ for the charged leptons were found in an analogous way, replacing (u, c, t) with (e, μ, τ).

Before we give any results we will take a moment to discuss their presentation. The state vectors and $\boldsymbol{\alpha}$ are vectors in $\mathbb{R}^3$ and of unit length so take values on the surface of a unit sphere. We will represent their positions by stereographically projecting onto $\mathbb{R}^2$. It turns out that $\boldsymbol{\alpha}$ does not need to rotate very far from $\mu = m_t$ to $\mu = m_e$ so most of the action happens in a small area on the sphere. We have chosen the south pole of the projection to be at the position of $\mathbf{v}_\tau$. This means that there will not be much distortion introduced by the stereographic projection; geodesics in this region on the sphere will be almost straight lines on the plane. Figure 3.1 shows the unit sphere with the region we will be interested in enclosed in a box. The curve within the box shows the best fit line we find and the point shows the south pole of the projection, $\mathbf{v}_\tau$. The projection itself is shown on the right. The metric on the sphere is given by

$$ds^2 = \frac{4}{(1+u^2+v^2)^2}(du^2 + dv^2) \tag{3.30}$$

for coordinates on the plane u and v. Over the boundary box in figure 3.1 the metric ranges from $4(du^2+dv^2)$ to $3.76(du^2+dv^2)$; there is a maximum distortion of a length in the stereographic projection of 3%.

3.3 Lattice Scan and Simplex Optimisation

Though we assume that the trajectory of $\boldsymbol{\alpha}$ is universal, there is no physical constraint on the relation between the quark and lepton sectors. We thus have the freedom to match these two sectors to give the smoothest trajectory. As mentioned previously we also have some freedom in choosing the matrix V. To find the best matching we ranged over, and then applied simplex optimisation at good regions in, the parameter space of quark-lepton sector matching matrices and quark mixing matrices, V.

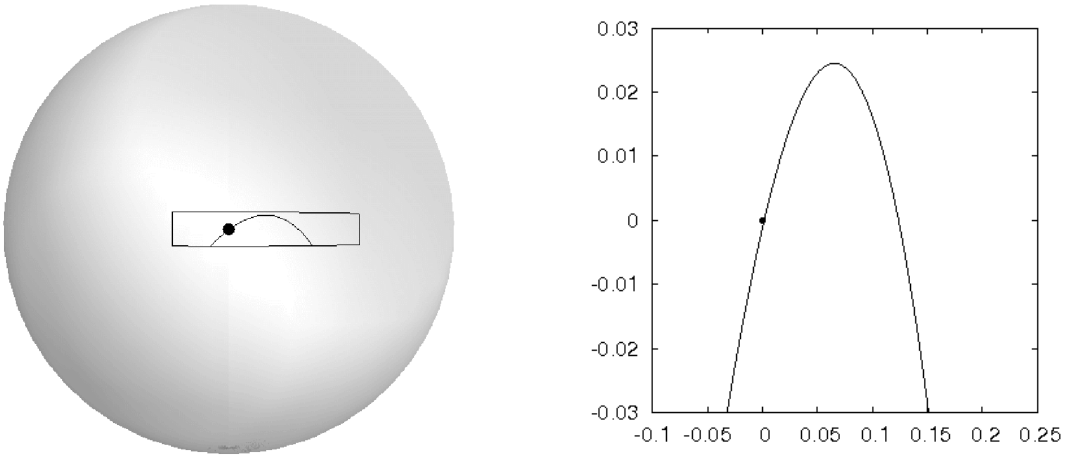

Figure 3.1: The state vectors and $\boldsymbol{\alpha}$ range over a unit sphere in $\mathbb{R}^3$. These are conveniently represented as points on the plane under stereographic projection. The point shown lies at the south pole of the projection. The box on the sphere is the boundary of the plot on the right and the curve shows the best fit line found.

3.3.1 Lattice Scan

Since we are considering right handed triads in $\mathbb{R}^3$ both the quark-lepton sector matching matrix and the quark mixing matrix will be matrices in $SO(3)$, each parameterised by 3 variables. There are no direct experimental constraints on these parameters, only indirectly through the scheme outlined above. It would take a long time to explore this six dimensional parameter space by hand so we developed an automated technique which can scan this space for us. To automate this process we need to produce a number which quantifies how good one point in parameter space is compared to another. We recall that we use the fermion masses and the Jarlskog invariant as inputs to our scheme. As outputs we have the absolute values of the CKM matrix and the 'smoothness' of the trajectory. We can capture the agreement of the CKM matrix with the experimental values through the quantity

$$W_{\text{CKM}} = \sum_{ij} \left| \frac{|V_{ij}| - |V_{ij}^{Exp}|}{|V_{ij}| + |V_{ij}^{Exp}|} \right|. \tag{3.31}$$

To quantify the 'smoothness' we found the R-Squared value of a cubic curve on the plane fitted to the positions of $\boldsymbol{\alpha}$. The R-Squared value of a fit is given by

$$R^2 \equiv 1 - \frac{\sum_i^N (y_i - f_i)^2}{\sum_i^N (y_i - \bar{y})^2}, \tag{3.32}$$

where (x_i, y_i) are the coordinates of N data points, f_i are the y coordinates of the best fit line at x_i and $\bar{y} = \frac{1}{N}\sum_i^N y_i$. This was used to create a quantity

$$W_{\mathrm{RSq}} = 1 - R^2 \tag{3.33}$$

which gives 0 if the fit passes through every point perfectly and approaches 1 as the fit gets worse. To combine the overall quality of a point in our parameter space we constructed the measure

$$W = W_{\mathrm{CKM}} + 40 \cdot W_{\mathrm{RSq}}. \tag{3.34}$$

This measure will be equal to 0 for a perfect fit and will grow as the fit gets worse. The coefficient was, and by necessity must be, chosen quite arbitrarily. We wanted a measure which gave a good balance between favouring a good CKM matrix and favouring a smooth fit. Some preliminary studies showed this choice to be appropriate.

Now we have a measure which can compare different points in parameter space we can automate the search over the parameter space. The most naïve way to search is to create a lattice on the space and search all of these points. This has the benefit that it objectively searches all of parameter space, but has the drawback that when one wants the lattice to be relatively fine it can take an inordinate amount of computing time. To reduce the time we can place restrictions on the viable areas of parameter space. We know that $m_c < m_\tau < m_b < m_t$, so $\boldsymbol{\alpha}_\tau$ and $\boldsymbol{\alpha}_b$ must lie between $\boldsymbol{\alpha}_c$ and $\boldsymbol{\alpha}_t$, and $\boldsymbol{\alpha}_\tau$ must be closer to $\boldsymbol{\alpha}_c$. This in turn places constraints on V and on the quark-lepton matching matrix.

Once the parameter space has been reduced like this we can run the scheme over all these points, figure 3.2. As the lattice spacing, a, is reduced the search does a better job of finding good points in parameter space, but the search takes longer. In a 6 dimensional parameter space it goes as $(1/a)^6$. To allow us to find the best points possible we performed a lattice scan followed by simplex optimisation in the most promising regions.

3.3.2 Simplex Optimisation

Simplex optimisation is an algorithm which walks around the parameter space, always flowing 'downhill' towards the point with the lowest measure. We will illustrate this process in a 2 dimensional parameter space. We first take a point in parameter space $\mathbf{x}_1$, the open circle in figure 3.3a. For $\mathbf{x}_1$ we chose the most promising points resulting from the lattice scan. Then, the basis vectors of the parameter space are used to

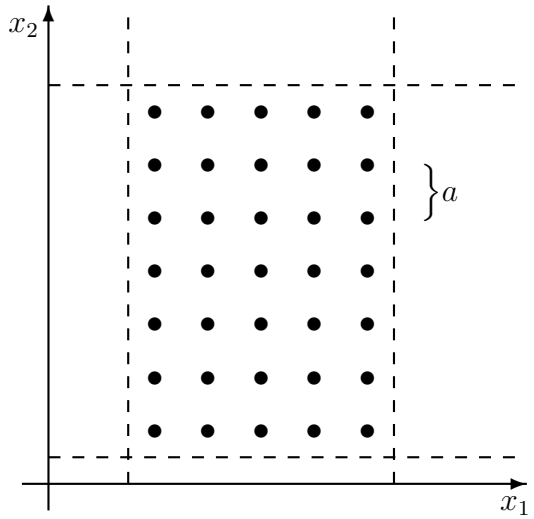

Figure 3.2: The points sampled in a lattice scan in a 2 dimensional parameter space with parameters x_1 and x_2. The dotted lines show limits placed by constraints. The lattice spacing here is a in both x_1 and x_2.

create the vertices of a 2-simplex, the closed circles in figure 3.3a. The value of W is then found at each of these points. Let us suppose that $\mathbf{x}_1$ returns the highest value for W. This point is then eliminated from the simplex and the centre of the remaining vertices, $\mathbf{o}$, is found, the cross in figure 3.3b.

A new vertex, $\mathbf{x}_2$, is then created at $\mathbf{o} - (\mathbf{x}_1 - \mathbf{o})$, figure 3.4a. A new simplex is then built around these three vertices and the process repeats, figure 3.4b.

The simplex then flows 'downhill', each time eliminating the point with the highest W, figure 3.5a. In this diagram the new vertices created are labelled $\{1, 2, 3, \dots\}$. Here the vertex labelled 5 is the lowest point found. If vertex 5 is a minimum the process continues and the simplex revolves around 5, or alternates between two adjacent simplices.

This search technique finds better points in the parameter space, but does not, as yet, improve the resolution. A simple way to improve this algorithm is to shrink the simplex as it walks around the parameter space. In this way it is able to walk some distance at the beginning of the process but achieve high resolution at the end. Figure 3.5b shows a similar path when the new vertex is placed at $\mathbf{o} - 0.9(\mathbf{x}_1 - \mathbf{o})$. In our case we performed the analogous process in 6 dimensions. We started with a step size of $a/2$ and continued until the measure at all seven vertices agreed to within approximately 1%.

For each point in parameter space tested the positions of $\boldsymbol{\alpha}_{t,c,b,s,\tau,\mu}$ were found and projected onto the plane as described earlier. We then fit a cubic line to these

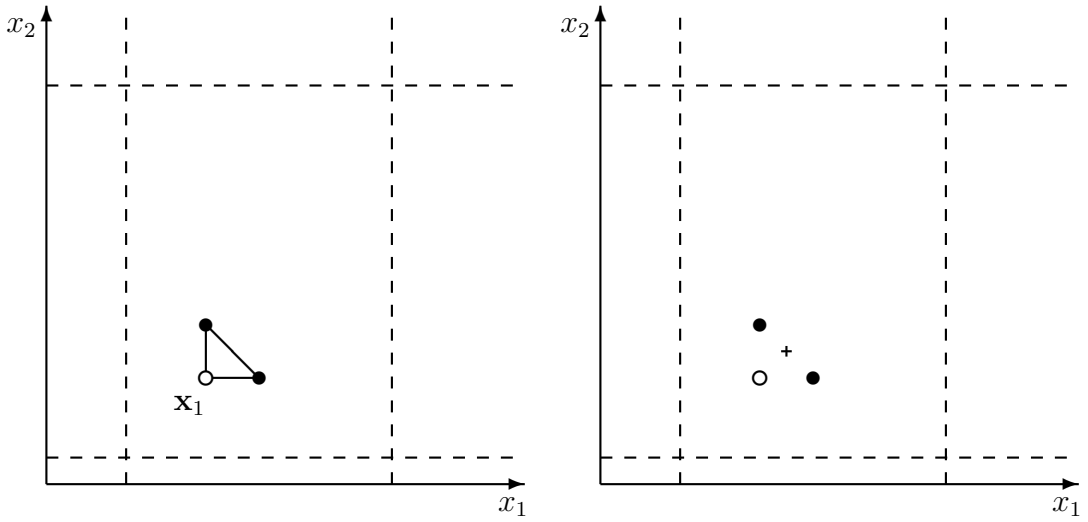

Figure 3.3: On the left (a), the initial point chosen is represented by an open circle, then the basis vectors are used to generate the points to make a 2-simplex. On the right (b), the open circle has the highest W so is removed. The center of the remaining vertices is then found, represented here by a cross.

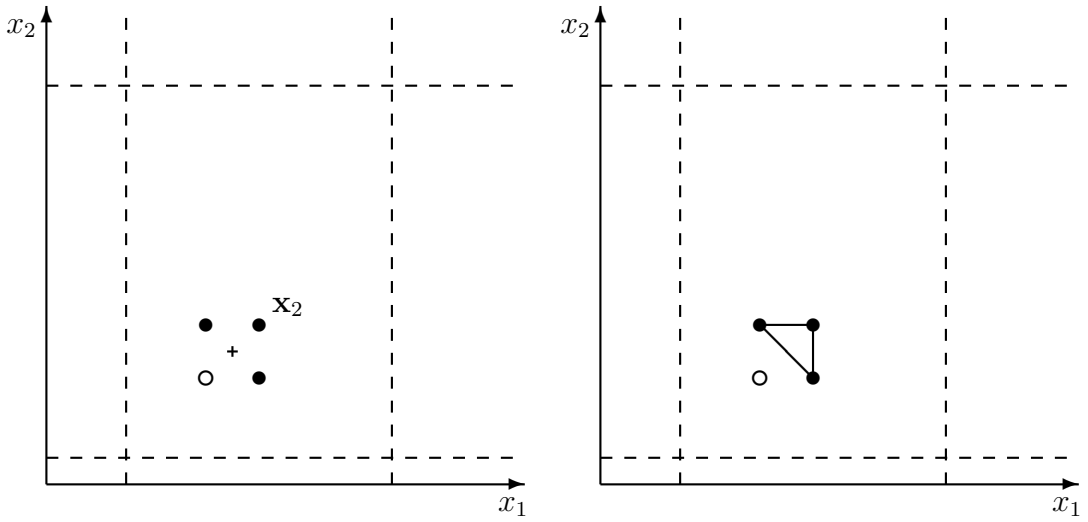

Figure 3.4: On the left (a), a new vertex is created opposite $\mathbf{x}_1$. On the right (b), a new simplex is created around these points and the process repeats.

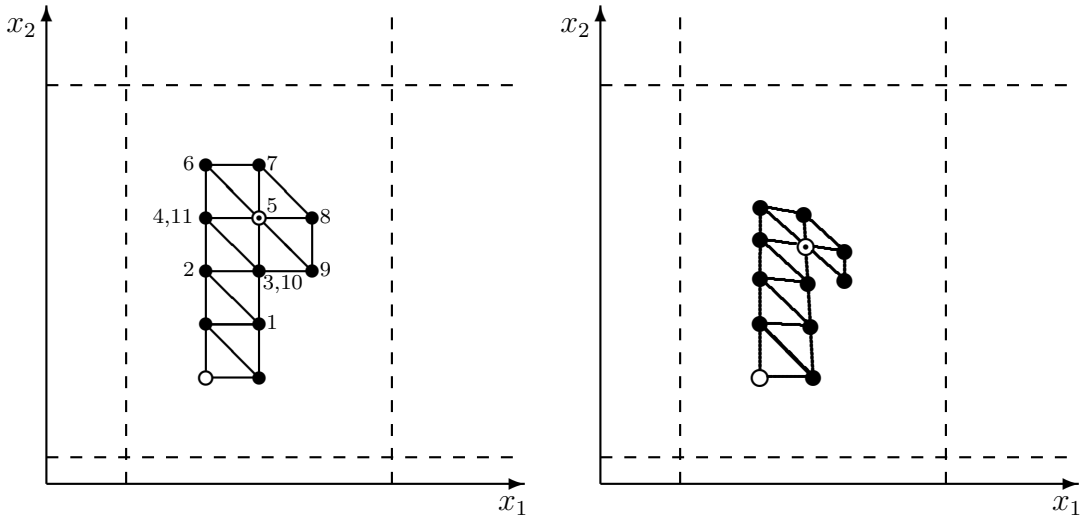

Figure 3.5: On the left (a), the simplex has walked around the parameter space and found vertex 5 to have the lowest W. On the right (b), we can improve the resolution of the optimisation as the simplex walks by reducing it's size each time it moves.

points on the plane using a non-linear least squares algorithm. Finally we use the Jarlskog invariant to fix the value of θ, determine the magnitudes of the elements of the CKM matrix and find W.

Previous work [10] has shown that the cumulative arc length between $\boldsymbol{\alpha}_x$ can be modelled by an exponential function at high scales. For the best fit curve we used a non-linear least squares algorithm to fit an exponential function to the cumulative arc length, excluding the strange quark and the electron. The strange quark was excluded since the interpretation of its intermediate mass is somewhat uncertain in this scheme. The electron was excluded firstly since we are only interested in the relationship at higher scales and secondly since we do not have good restrictions on the cumulative arc length, as $\boldsymbol{\alpha}_e$ can only be constrained to lie on a line.

3.4 Results

Having completed the lattice scan and simplex optimisation, figure 3.6 shows the cubic best fit line along with the position of $\boldsymbol{\alpha}$ at various scales. The experimental errors in the masses of the quarks lead to an uncertainty in the position of $\boldsymbol{\alpha}_c$ and $\boldsymbol{\alpha}_s$. The 1 σ errors in the quark masses restrict $\boldsymbol{\alpha}_c$ and $\boldsymbol{\alpha}_s$ to lie on the lines shown. The cubic best fit line is

$$0.75\,x - 4.83\,x^2 - 9.19\,x^3. \tag{3.35}$$

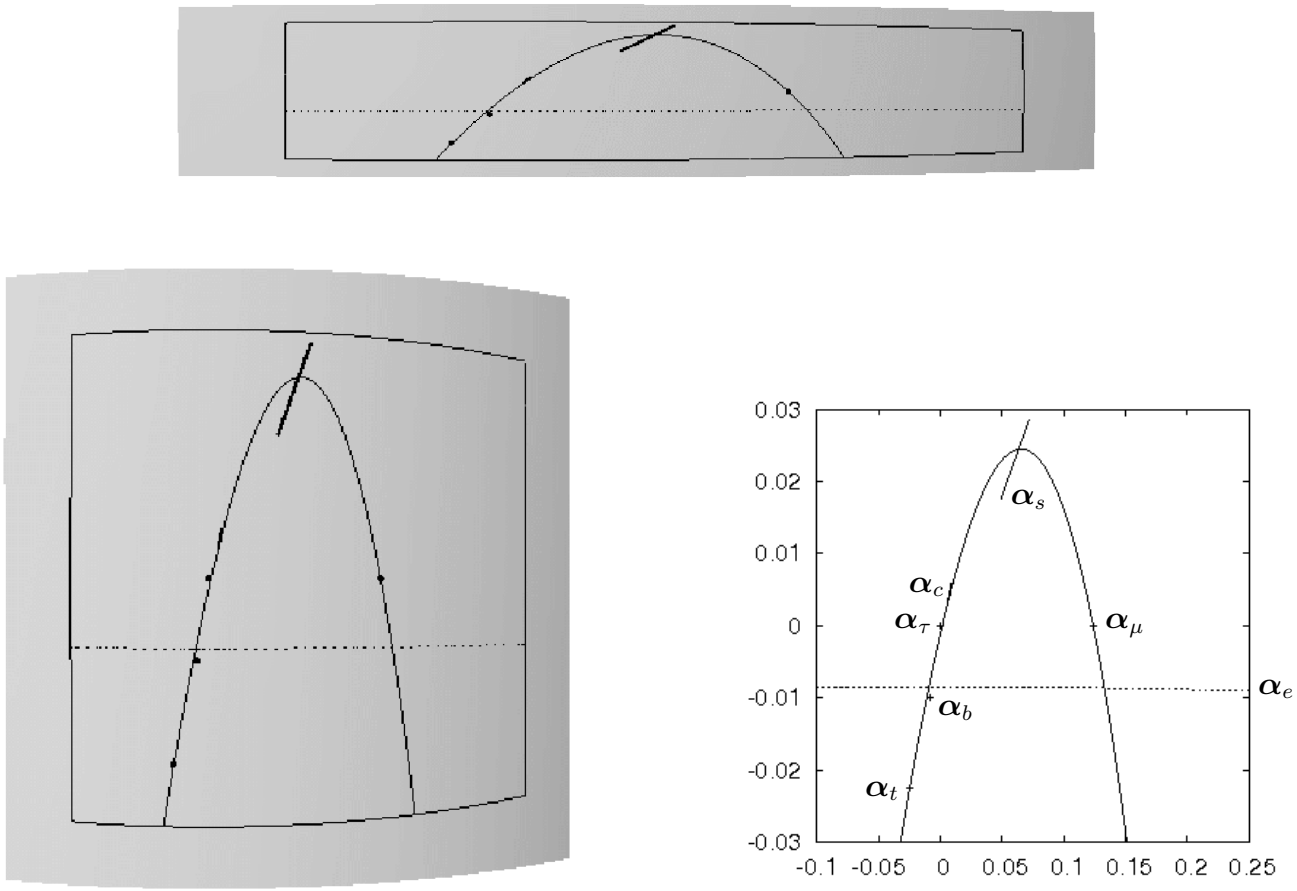

Figure 3.6: The positions of $\boldsymbol{\alpha}$ at various scales determined by experimental constraints and 'smoothness'. The position of $\boldsymbol{\alpha}_e$ is constrained to lie somewhere on the dotted line. The cubic best fit line is shown by the solid line. The top shows these on the sphere, left shows them on an ellipsoid with the axes stretched to match those of the stereographic projection while the right shows the stereographic projection with the positions of $\boldsymbol{\alpha}_x$ indicated.

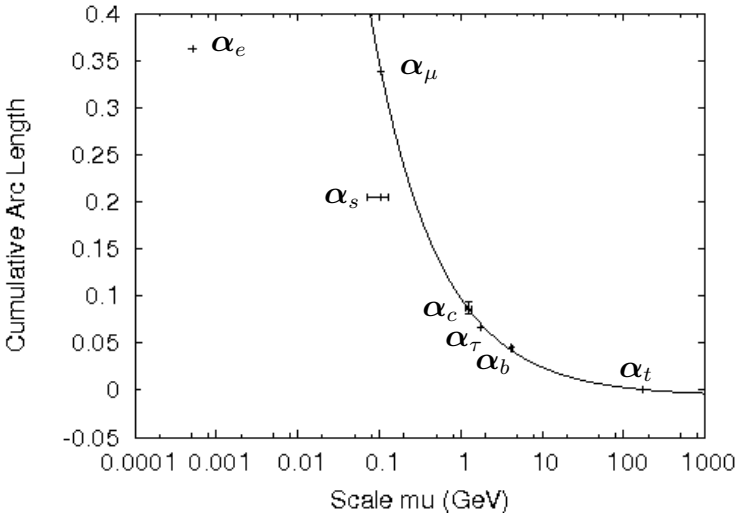

Figure 3.7: The cumulative arc length along the best fit line measured from $\boldsymbol{\alpha}_t$ is well approximated by an exponential curve for all but $\boldsymbol{\alpha}_s$ and $\boldsymbol{\alpha}_e$. A great circle gives an arc length of 2π in these units.

The cumulative arc length between $\boldsymbol{\alpha}_x$'s was found after mapping the cubic best fit line onto the sphere through an inverse stereographic projection.

Figure 3.7 shows that the arc lengths between $\boldsymbol{\alpha}_t$, $\boldsymbol{\alpha}_b$, $\boldsymbol{\alpha}_\tau$, $\boldsymbol{\alpha}_c$ and $\boldsymbol{\alpha}_\mu$ are well fitted by the exponential curve

$$0.104 \exp\left(-1.228 \log_{10}(\mu)\right) - 0.0061 \tag{3.36}$$

for μ in GeV. This is in good agreement with the results from the planar approximation found in [10]. The point $\boldsymbol{\alpha}_s$ does not fit on the exponential curve as discussed. The arc length to $\boldsymbol{\alpha}_e$ is estimated by the arc length to $\boldsymbol{\alpha}_e$ line. This is just an estimate since $\boldsymbol{\alpha}_e$ may sit anywhere on this line. It is, however, clear that $\boldsymbol{\alpha}_e$ is unlikely to sit on the exponential curve found. Various models which employ the rotating mass matrix mechanism suggest a $\tanh(\mu)$ like behaviour, with fixed points for the rotation at $\mu = 0$ and $\mu = \infty$, so it is not surprising that the exponential fit matches the data well at higher scales but not at lower scales. For the later work on Higgs decay we only need to model the behaviour at high scales.

For this trajectory we find $\omega_U = 0.09$ radians and $\omega_D = 0.25$ radians. Fitting a Jarlskog invariant of $J = 3.05 \times 10^{-5}$ gives a strong CP angle of 1.45 radians. These results are in line with estimates in [12]. The absolute values of the CKM matrix obtained are

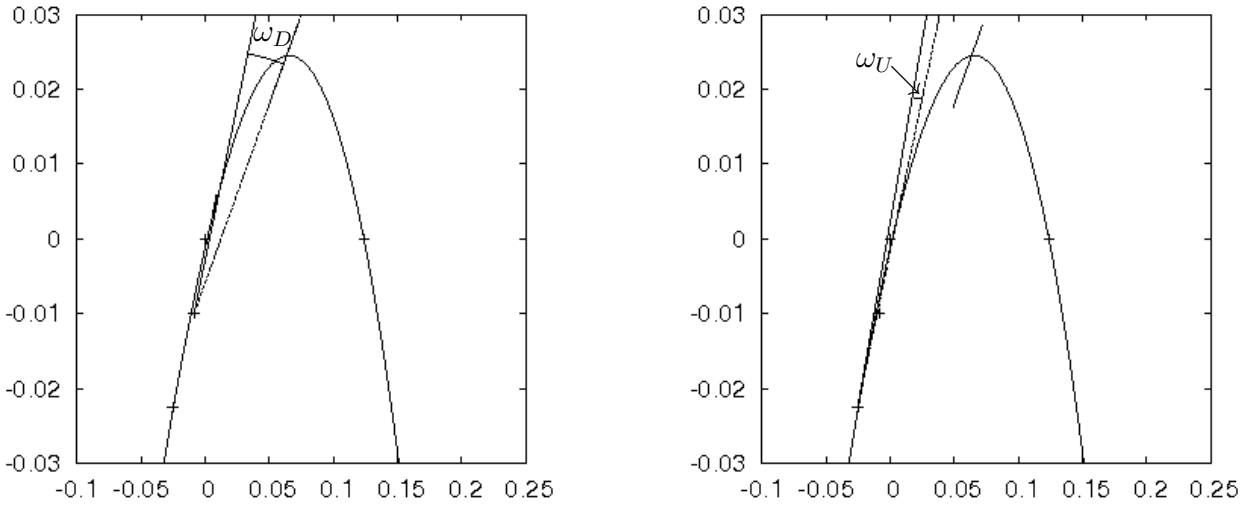

Figure 3.8: An illustration of the angle ω_D (ω_U). Here the state vector triad and the Darboux triad have their origins at $\boldsymbol{\alpha}_b$ ($\boldsymbol{\alpha}_t$). The solid line shows $\boldsymbol{\tau}(\mu) \parallel \dot{\boldsymbol{\alpha}}(\mu)$ and the dashed line shows $\mathbf{v}_s$ ($\mathbf{v}_c$). It should be remembered that the axes are not of equal scale and that this is a stereographic projection of the vectors so the angles cannot be directly read off.

$$\begin{pmatrix} 0.97430 & 0.2252 & 0.00357 \\ 0.2251 & 0.97345 & 0.0415 \\ 0.00879 & 0.0407 & 0.999134 \end{pmatrix}, \tag{3.37}$$

which are in good agreement with the experimental values [1]:

$$\begin{pmatrix} 0.97419 \pm 0.00022 & 0.2257 \pm 0.0010 & 0.00359 \pm 0.00016 \\ 0.2256 \pm 0.0010 & 0.97334 \pm 0.00023 & 0.0415^{+0.0010}_{-0.0011} \\ 0.00874^{+0.00026}_{-0.00037} & 0.0407 \pm 0.0010 & 0.999133^{+0.000044}_{-0.000043} \end{pmatrix}. \tag{3.38}$$

We find the unitarity angles, defined and measured [1] as

$$\alpha = \arg\left(-\frac{V_{td}V_{tb}^*}{V_{ud}V_{ub}^*}\right) = (88^{+6}_{-5})^\circ, \tag{3.39}$$

$$\beta = \arg\left(-\frac{V_{cd}V_{cb}^*}{V_{td}V_{tb}^*}\right) = \frac{1}{2}\sin^{-1}(0.681 \pm 0.025), \tag{3.40}$$

$$\gamma = \arg\left(-\frac{V_{ud}V_{ub}^*}{V_{cd}V_{cb}^*}\right) = (77^{+30}_{-32})^\circ, \tag{3.41}$$

to be $\alpha = 88^\circ$, $\sin(2\beta) = 0.691$ and $\gamma = 70^\circ$.

Chapter 4

Higgs Decay

In the standard model spontaneous symmetry breaking in the electroweak sector generates fermion mass terms. The fermion-Higgs boson couplings give both the fermion masses and the Higgs decay branching ratios. In any model which employs the Higgs mechanism, if the mass matrix rotates then the rotation can be used to estimate the Higgs decay branching ratios. In this section we use the trajectory of $\boldsymbol{\alpha}$ to make estimates of Higgs decay branching ratios for a range of Higgs masses.

4.1 Theoretical Background

Now that we have found a trajectory of $\boldsymbol{\alpha}$ which agrees well with experimental constraints we can use it to ask what the rotating mass matrix hypothesis may say about Higgs decay. Though we have so far ignored the lightest quarks note that the up and down triads are fixed at $\mu = m_c$ and $\mu = m_s$ respectively. We can make predictions for the branching ratios of modes involving the up and down quarks since we shall see that they depend only on the quark state vectors and the position of $\boldsymbol{\alpha}$ at $\mu = m_H/2$. We can similarly make predictions for modes involving the electron. The following Yukawa couplings have been suggested [13], e.g., for the up-type quarks:

$$\mathcal{L}_{YK} = \rho_U \overline{\Psi}_L \phi \boldsymbol{\alpha}\boldsymbol{\alpha}^\dagger \Psi_R + h.c. \tag{4.1}$$

Choosing the gauge in which ϕ, the Higgs doublet, is real and points in the up direction and expanding the remaining real component about its minimum value ζ_W, $\phi^1_R = \zeta_W + H$, we obtain the zeroth order mass matrix,

$$\begin{aligned} \mathcal{L}_{YK} &= \rho_U \zeta_W \overline{\Psi}_L \boldsymbol{\alpha}\boldsymbol{\alpha}^\dagger \Psi_R + h.c. \\ &= m_U \overline{\Psi}_L \boldsymbol{\alpha}\boldsymbol{\alpha}^\dagger \Psi_R + h.c., \end{aligned} \tag{4.2}$$

where we have writen $m_U = \rho_U \zeta_W$, and the first order coupling matrix of the Higgs boson to the quarks,

$$Y = \rho_U \boldsymbol{\alpha}\boldsymbol{\alpha}^\dagger. \tag{4.3}$$

Since this Yukawa coupling matrix depends on scale, μ, we need to take care in defining the details of Higgs decay. In constraining the trajectory of $\boldsymbol{\alpha}$ we were considering fermion masses, whereas now we are considering Higgs decay. These are clearly related processes but in integrating the assumed underlying RGE the constant of integration may differ. To find the correct calibration we consider the threshold scale for production of a fermion pair, $\mu = 2m_f$. The fermions will be at rest so the Higgs coupling matrix should be proportional to the fermion mass matrix,

$$\langle \mathbf{v}_f | Y(\mu = 2m_f) | \mathbf{v}_f \rangle = \rho_T |\langle \mathbf{v}_f | \boldsymbol{\alpha}(\mu = 2m_f)\rangle|^2 = m_f/\zeta_W. \tag{4.4}$$

However, when extracting fermion masses from the rotating mass matrix we had

$$m_f = \zeta_W \rho_T |\langle \mathbf{v}_f | \boldsymbol{\alpha}(\mu = m_f)\rangle|^2. \tag{4.5}$$

The correct calibration is a factor of 2 change in scale, i.e., $\boldsymbol{\alpha}_H = \boldsymbol{\alpha}(\mu = m_H/2)$. We take the scale of Higgs decay to be that of the Higgs mass, as usual. We can now use the best fit line to find the Higgs state tensor, $\boldsymbol{\alpha}\boldsymbol{\alpha}^\dagger$, as a function of Higgs mass.

We then get the coupling for Higgs decaying into $x\overline{y}$,

$$A(H \to x\overline{y}) = \rho_{T_x} |\mathbf{v}_x \cdot \boldsymbol{\alpha}_H||\mathbf{v}_y \cdot \boldsymbol{\alpha}_H|. \tag{4.6}$$

We can ignore any kinematic factors by considering ratios of branching ratios,

$$\frac{\Gamma(H \to x\overline{y})}{\Gamma(H \to b\overline{b})} = \frac{\rho_{T_x}^2}{\rho_D^2} \frac{|\mathbf{v}_x \cdot \boldsymbol{\alpha}_H|^2 |\mathbf{v}_y \cdot \boldsymbol{\alpha}_H|^2}{|\mathbf{v}_b \cdot \boldsymbol{\alpha}_H|^4}. \tag{4.7}$$

The trajectory of $\boldsymbol{\alpha}$ found resulted from only the left handed fields, whereas Higgs decay will involve both right and left handed fields. Using the trajectory found from only the left handed fields is equivalent to ignoring the chiral rotation, resulting in a real CKM matrix. In section 7.4 we argue that the error introduced in the CKM matrix by this approximation is less than 2% for all but one element whose error is less than 10%.

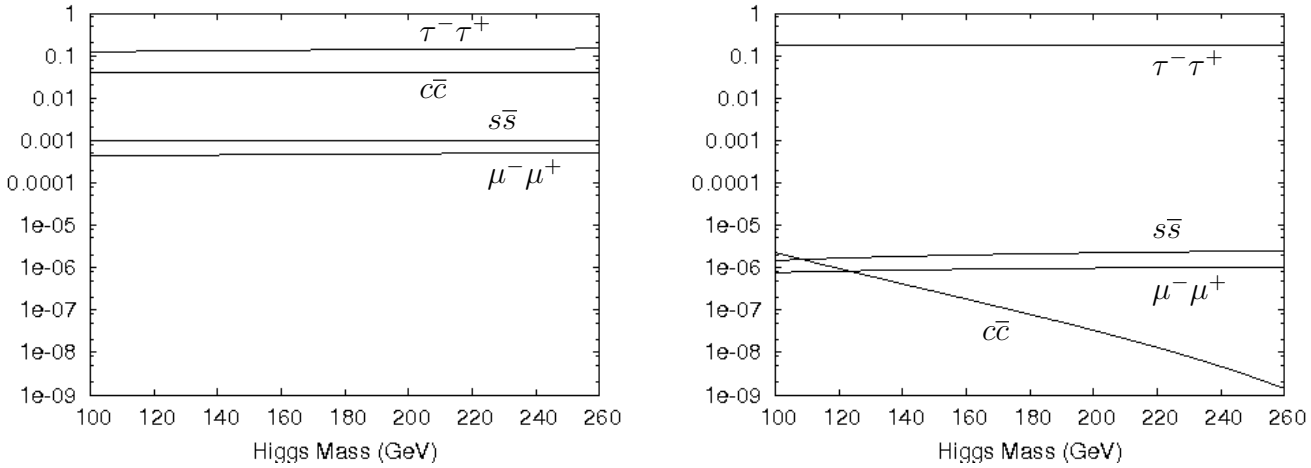

Figure 4.1: $\Gamma(H \to x\overline{x})/\Gamma(H \to b\overline{b})$ for various final state particles as predicted by the standard model (left) and the rotating mass matrix hypothesis (right).

4.2 Results

Now we have explicit formulae for the best fit trajectory of $\boldsymbol{\alpha}$ and the relation between arc length and scale, at high energies, it becomes a simple matter to find the ratios of branching ratios, given by (4.7), for a range of Higgs masses. LEP found a lower limit on the Higgs mass of 114.4 GeV at 95% confidence level [1]. Various upper bounds have been given for the standard model Higgs boson mass. Here we plot up to $m_H = 260$ GeV. Figure 4.1 shows the standard model predictions for Higgs decay along with the predictions from the rotating mass matrix hypothesis. The standard model predictions were found using `HDECAY` [27]. We can see that the $c\overline{c}$ decay mode is heavily suppressed, in accordance with the estimate in [13]. This mode is suppressed since near $\mu = 2\,m_t$ the eigenvector $\boldsymbol{\alpha}$ is almost orthogonal to $\mathbf{v}_c$, reducing the branching ratio to $c\overline{c}$. The suppression is to such a degree over the whole range of Higgs masses that detection should not require large statistics. The $s\overline{s}$ and $\mu^-\mu^+$ modes are also suppressed, though to a smaller degree.

Although we propose no dynamical mechanism the rotating mass matrix picture generically predicts flavour violating decays, shown in figure 4.2. If the Higgs mass is large then $t\overline{c}$ and $t\overline{u}$ decay modes are possible. To be in line with the rest of the estimates, where the decays are well above threshold, we neglect threshold effects for these modes. Above 220 GeV we believe that these effects will be negligible and that the estimates shown for the branching ratios are realistic. The branching ratio for $H \to \tau^-\mu^+$ is almost three orders of magnitude higher than that for $H \to \mu^-\mu^+$. This

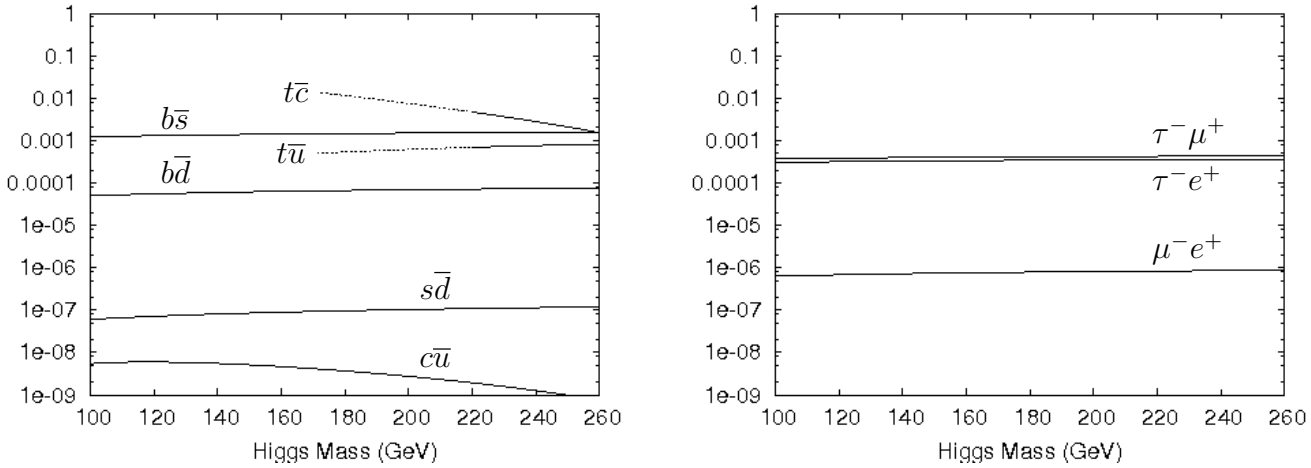

Figure 4.2: $\Gamma(H \to x\overline{y})/\Gamma(H \to b\overline{b})$ for various flavour violating decays as predicted by the rotating mass matrix hypothesis. Note that $\Gamma(H \to y\overline{x}) = \Gamma(H \to x\overline{y})$. Below around 220 GeV, indicated by the dotted lines, threshold effects will influence the $t\overline{c}$ and $t\overline{u}$ decay modes.

is in stark contrast to the standard model predictions where $H \to \tau^-\mu^+$ cannot occur at tree level and so has a small branching ratio. These modes may have a cleaner signal than $H \to c\overline{c}$, making it easier to detect. Flavour violating effects at the levels predicted here have been shown in [13] to be consistent with existing experimental bounds on flavour violation.

Part II

The Rank-One Rotating Mass Matrix Hypothesis: A Model Specific Study

Chapter 5

The Framed Standard Model

In the second part of this thesis we take a bottom up approach in exploring the ideas which were studied with a top down approach in the first part. The framed standard model (FSM) [2, 19] is a quantum field theory with a rank-one rotating mass matrix. In this part we investigate whether the renormalisation group equation (RGE) generated by one one-loop diagram can rotate the mass matrix to match experimental data. As we are only considering one diagram, and at one-loop level, the results must be seen as a first approximation, but none-the-less it can demonstrate the feasibility of the scheme. In this chapter we will outline the FSM and derive the one-loop renormalisation group equation for the mass matrix. In the next chapter we consider complications arising from a non-trivial metric on the internal symmetry space and the possible effects of QCD running of the mass matrix eigenvalues. In chapter 7 we describe the search methodology and discuss the most promising trajectories found. Finally we consider the implications for Higgs decay.

5.1 Outline of the FSM

The standard model has a local $u(1) \times su(2) \times su(3)$ gauge symmetry (throughout this thesis we will refer only to the algebra as we will not be concerned with any group structure) at each point, x, in Minkowski space-time. Each of these symmetries introduces a connection on their corresponding principle bundle which becomes, physically, a gauge field, $A_\mu(x)$, $B_\mu(x)$ and $C_\mu(x)$ respectively. This natural, geometric appearance of the gauge fields is one of the more theoretically satisfying aspects of the standard model. The fact that the fermion and scalar fields have no such geometric origin, but are rather introduced by hand, is, theoretically, a significant shortcoming. The FSM posits that, in addition the this geometric structure for the usual gauge fields, the scalar fields can be ascribed some geometric significance. In the FSM the

standard model gauge symmetries are paired with a corresponding global symmetry, $\tilde{u}(1) \times \widetilde{su}(2) \times \widetilde{su}(3)$. The geometric motivation being that, as in space-time, one can globally change the reference frame without changing any of the physics. As in the vielbein picture of gravity, the matrices representing these changes of reference frame are promoted to dynamical variables, or so called framon fields.

The FSM introduces two types of framon fields: the weak framon fields,

$$\phi_r^{\tilde{r}\tilde{a}}(x) = \alpha^{\tilde{a}} \phi_r^{\tilde{r}}(x), \tag{5.1}$$

transforming in the $(\mathbf{1} \otimes \mathbf{2} \otimes \mathbf{1}) \otimes (\tilde{\mathbf{1}} \otimes \tilde{\mathbf{2}} \otimes \tilde{\mathbf{3}})$ representation of $u(1) \times su(2) \times su(3) \times \tilde{u}(1) \times \widetilde{su}(2) \times \widetilde{su}(3)$ and the strong framon fields,

$$\phi_a^{\tilde{r}\tilde{a}}(x) = \alpha^{\tilde{r}} \phi_a^{\tilde{a}}(x), \tag{5.2}$$

transforming in the $(\mathbf{1} \otimes \mathbf{1} \otimes \mathbf{3}) \otimes (\tilde{\mathbf{1}} \otimes \tilde{\mathbf{2}} \otimes \tilde{\mathbf{3}})$ representation, where $r, \tilde{r} = 1, 2$ and $a, \tilde{a} = 1, 2, 3$ are $su(2)$, $\widetilde{su}(2)$, $su(3)$ and $\widetilde{su}(3)$ indices respectively. The factors $\phi_r^{\tilde{r}}(x)$ and $\phi_a^{\tilde{a}}(x)$ transform under the fundamental representation of $su(N)$ acting from the left for local transformations and under the anti-fundamental representation of $\widetilde{su}(N)$ acting from the right for global transformations, for $N = 2, 3$ respectively. The fields $\phi_r^{\tilde{r}}(x)$ and $\phi_a^{\tilde{a}}(x)$ are space-time dependent Lorentz scalar fields. The factors $\alpha^{\tilde{a}}$ and $\alpha^{\tilde{r}}$ are global quantities independent of space-time and are normalised to have unit length. The $(u(1), \tilde{u}(1))$ charges of the weak and strong framon fields are $(\pm\frac{1}{2}, \mp\frac{1}{2})$ (the sign depending on whether $\tilde{r}$=1 or 2) and $(-\frac{1}{3}, \frac{1}{3})$ respectively. The components of these fields are not all independent. The weak framon fields satisfy

$$\phi_r^{\tilde{2}} = i\epsilon_{rs}(\phi_s^{\tilde{1}})^* \tag{5.3}$$

and the strong framon fields satisfy

$$\det(\Phi) \in \mathbb{R}, \tag{5.4}$$

where Φ is the matrix with elements $\phi_a^{\tilde{a}}(x)$. These conditions reduce the 8 and 18 real degrees of freedom of the original fields to 4 and 17 real degrees of freedom, for the weak and strong framons respectively.

These constraints are motivated by the conditions for a unitary matrix, which the framon fields would satisfy had they not been promoted to fields:

$$\Phi^\dagger \Phi = 1, \tag{5.5}$$

$$|\det(\Phi)| = 1. \tag{5.6}$$

Condition (5.3) is obtained by retaining as much of conditions (5.5) and (5.6) as possible, while insisting on at least one field variable. The analogous condition does not hold in the $su(3)$ case as it would force different degrees of freedom to have different dimension, which is not physically permissible. Condition (5.4) is the strongest condition which allows dynamical fields but with all the degrees of freedom having the same dimension.

Given the conditions on the framon fields we can, and will, simplify notation somewhat by constructing vectors in $\widetilde{su}(2)$ and $\widetilde{su}(3)$ space. For the weak framons we will write

$$\phi = \begin{pmatrix} \phi_1^{\tilde{1}} \\ \phi_2^{\tilde{1}} \end{pmatrix}. \tag{5.7}$$

This completely specifies the weak framon field as the $\phi_r^{\tilde{2}}$ components are given by the $\phi_r^{\tilde{1}}$ components through condition (5.3). For the strong framons we will write

$$\phi_a = \begin{pmatrix} \phi_a^{\tilde{1}} \\ \phi_a^{\tilde{2}} \\ \phi_a^{\tilde{3}} \end{pmatrix}. \tag{5.8}$$

As they will arise quite frequently, we will often write $\zeta_W^2 = |\phi|^2$ and $\zeta_S^2 = \sum_a |\phi_a|^2$. We will also write

$$\boldsymbol{\alpha} = \begin{pmatrix} \alpha^{\tilde{1}} \\ \alpha^{\tilde{2}} \\ \alpha^{\tilde{3}} \end{pmatrix} \tag{5.9}$$

which, since $\alpha^{\tilde{a}}$ was normalised, will have unit length.

The action for the bosonic sector of the FSM can be written as

$$\mathcal{A}_B = \mathcal{A}_{GF} + \mathcal{A}_{KE} + \int d^4x V[\Phi], \tag{5.10}$$

where $\mathcal{A}_{GF}$ contains the pure gauge field action, $\mathcal{A}_{KE}$ contains the kinetic terms for the framon fields and $V[\Phi]$ is the self-interaction potential of the framon fields. As usual,

$$\mathcal{A}_{GF} = -\frac{1}{4}\int d^4x F_{\mu\nu}F^{\mu\nu} - \frac{1}{4}\int d^4x \mathrm{Tr}(G_{\mu\nu}G^{\mu\nu}) - \frac{1}{4}\int d^4x \mathrm{Tr}(H_{\mu\nu}H^{\mu\nu}), \tag{5.11}$$

where

$$F_{\mu\nu} = \partial_\nu A_\mu - \partial_\mu A_\nu, \tag{5.12}$$
$$G_{\mu\nu} = \partial_\nu B_\mu - \partial_\mu B_\nu + ig_2[B_\mu, B_\nu], \tag{5.13}$$
$$H_{\mu\nu} = \partial_\nu C_\mu - \partial_\mu C_\nu + ig_2[C_\mu, C_\nu], \tag{5.14}$$

are the $u(1)$, $su(2)$ and $su(3)$ field strength tensors respectively. The kinetic term for the framon fields can be written as

$$\mathcal{A}_{KE} = \int d^4x \left[2(D^{(W)}_\mu\phi)^\dagger(D^{(W)\mu}\phi) + \sum_a (D^{(S)}_\mu\phi_a)^\dagger(D^{(S)\mu}\phi_a)\right], \tag{5.15}$$

where

$$D^{(W)}_\mu = \partial_\mu - ig_1qA_\mu - ig_2B_\mu, \tag{5.16}$$
$$D^{(S)}_\mu = \partial_\mu + i\frac{g_1}{3}A_\mu - ig_3C_\mu, \tag{5.17}$$

are the weak framon and strong framon covariant derivatives respectively.

The most general renormalisable Lorentz and gauge invariant framon self-interaction potential can be written in the form

$$V[\Phi] = V_W[\Phi] + V_S[\Phi] + V_{WS}[\Phi], \tag{5.18}$$

where $V_W[\Phi]$ contains only the weak framon field, $V_S[\Phi]$ contains only the strong framon field and $V_{WS}[\Phi]$ contains both fields. These terms, once the conditions on the weak and strong framons are enforced, are

$$V_W[\Phi] = -\mu_W \sum_r \phi^{\tilde{1}}_r\phi^{\tilde{1}*}_r + \lambda_W\left[\sum_r \phi^{\tilde{1}}_r\phi^{\tilde{1}*}_r\right]^2, \tag{5.19}$$

$$V_S[\Phi] = -\mu_S \sum_{a,\tilde{a}} (\phi^{\tilde{a}*}_a\phi^{\tilde{a}}_a) + \lambda_S\left[\sum_{a,\tilde{a}} (\phi^{\tilde{a}*}_a\phi^{\tilde{a}}_a)\right]^2 + \kappa_S \sum_{a,b,\tilde{a},\tilde{b}} (\phi^{\tilde{a}*}_a\phi^{\tilde{b}}_b)(\phi^{\tilde{b}*}_b\phi^{\tilde{a}}_a), \tag{5.20}$$

$$V_{WS}[\Phi] = \nu_1 \sum_r \phi^{\tilde{1}}_r\phi^{\tilde{1}*}_r \sum_{a,\tilde{a}} (\phi^{\tilde{a}*}_a\phi^{\tilde{a}}_a) - \nu_2 \sum_r \phi^{\tilde{1}}_r\phi^{\tilde{1}*}_r \sum_a \left|\sum_{\tilde{a}} (\alpha^{\tilde{a}*}\phi^{\tilde{a}}_a)\right|^2. \tag{5.21}$$

We can simplify the notation using the vectors introduced in equations (5.7), (5.8) and (5.9),

$$\begin{aligned} V[\Phi] = &- \mu_W|\phi|^2 + \lambda_W(|\phi|^2)^2 \\ &- \mu_S \sum_a |\phi_a|^2 + \lambda_S \left[\sum_a |\phi_a|^2\right]^2 + \kappa_S \sum_{a,b} |(\phi_a^* \cdot \phi_b)|^2 \\ &+ \nu_1|\phi^2| \sum_a |\phi_a|^2 - \nu_2|\phi|^2 \sum_a |(\boldsymbol{\alpha}^* \cdot \phi_a)|^2. \end{aligned} \tag{5.22}$$

The FSM takes the first 6 coupling constants to be positive. The sign of ν_2 is not fixed. The weak framon and the strong framon sectors are linked through the ν_1 and ν_2 terms. The ν_2 term contains, crucially, $\boldsymbol{\alpha}$, a global vector in $\widetilde{su}(3)$ space. The vacuum for this potential is investigated in [2] and [19] and is found to have a degeneracy which can be labelled by $\boldsymbol{\alpha}$. As $\boldsymbol{\alpha}$ varies there is a trade off between the orthogonality and the normality of ϕ_1, ϕ_2, and ϕ_3. Once the fermions and Yukawa terms are introduced $\boldsymbol{\alpha}$ will become the eigenvector of a rank-one mass matrix. We will find that the strong framon contribution to the fermion self energy will rotate $\boldsymbol{\alpha}$, and so also the vacuum, as scale changes. The normality of ϕ_a then depends on scale and, since they play a geometric role, this introduces a scale dependent metric on $\widetilde{su}(3)$ space.

We interrupt this discussion of the vacuum to make a brief aside and introduce some notation relating to gauge fixing. As noted we now have 4 real degrees of freedom for the weak framons and 17 real degrees of freedom for the strong framon fields. However, not all of these degrees of freedom are physical. When we want to find a physical quantity we will fix the gauge freedoms. Local gauge fixing will remove 3 degrees of freedom from the weak framon fields and 8 degrees of freedom from the strong framon fields, leaving 1 and 9 degrees of freedom respectively. We will always choose the $su(2)$ gauge so that

$$\phi = \begin{pmatrix} \zeta_W \\ 0 \end{pmatrix}, \tag{5.23}$$

where $\zeta_W \in \mathbb{R}$. A useful $su(3)$ gauge choice is one where the strong framon field appears triangular:

$$\Phi_{\mathrm{T}} = \begin{pmatrix} \phi_{\mathrm{T}1R}^{\tilde{1}} & \phi_{\mathrm{T}1R}^{\tilde{2}} + i\phi_{\mathrm{T}1I}^{\tilde{2}} & \phi_{\mathrm{T}1R}^{\tilde{3}} + i\phi_{\mathrm{T}1I}^{\tilde{3}} \\ 0 & \phi_{\mathrm{T}2R}^{\tilde{2}} & \phi_{\mathrm{T}2R}^{\tilde{3}} + i\phi_{\mathrm{T}2I}^{\tilde{3}} \\ 0 & 0 & \phi_{\mathrm{T}3R}^{\tilde{3}} \end{pmatrix}. \tag{5.24}$$

Another useful choice is the gauge where the strong framon field is Hermitian:

$$\Phi_{\rm H} = \begin{pmatrix} \phi^{\tilde{1}}_{{\rm H}1R} & \phi^{\tilde{2}}_{{\rm H}1R} + i\phi^{\tilde{2}}_{{\rm H}1I} & \phi^{\tilde{3}}_{{\rm H}1R} + i\phi^{\tilde{3}}_{{\rm H}1I} \\ \phi^{\tilde{2}}_{{\rm H}1R} - i\phi^{\tilde{2}}_{{\rm H}1I} & \phi^{\tilde{2}}_{{\rm H}2R} & \phi^{\tilde{3}}_{{\rm H}2R} + i\phi^{\tilde{3}}_{{\rm H}2I} \\ \phi^{\tilde{3}}_{{\rm H}1R} - i\phi^{\tilde{3}}_{{\rm H}1I} & \phi^{\tilde{3}}_{{\rm H}2R} - i\phi^{\tilde{3}}_{{\rm H}2I} & \phi^{\tilde{3}}_{{\rm H}3R} \end{pmatrix}. \tag{5.25}$$

We can see explicitly that in both cases there are 9 real degrees of freedom.

During the work several gauges and vacuums will be utilised. We will at times consider the three different cases, either no gauge fixing, the triangular gauge or the hermitian gauge. We will keep track of these changes by noting the $su(3)$ local gauge, $\widetilde{su}(3)$ global gauge and vacuum we've chosen, in the form ($su(3)$ local gauge, $\widetilde{su}(3)$ global gauge, vacuum). We will find that if we start with the local gauge chosen so that the framon field is triangular, the global gauge fixed by $\boldsymbol{\alpha}^\dagger = (1,0,0) =: \boldsymbol{\alpha}_0^\dagger$ and the vacuum labelled by $\boldsymbol{\alpha}_0$ then the vacuum is diagonal, which is calculationally convenient. This set up will be labelled $(T_0, \boldsymbol{\alpha}_0, \boldsymbol{\alpha}_0)$. We may look at a general vacuum in the same local and global gauge but at a different vacuum by acting on the framon field on the right with a general global $\widetilde{su}(3)$ rotation A, $(T_0, \boldsymbol{\alpha}_0, \boldsymbol{\alpha}) = (T_0, \boldsymbol{\alpha}_0, \boldsymbol{\alpha}_0)A^{-1}$. The framon field will still be in the same gauge, but will no longer appear triangular. At other times we will be interested in working in the hermitian gauge. This will be denoted $(H, \boldsymbol{\alpha}_0, \boldsymbol{\alpha}_0)$ or $(H, \boldsymbol{\alpha}_0, \boldsymbol{\alpha})$ depending on whether we are looking at a specific or general vacuum. Again $(H, \boldsymbol{\alpha}_0, \boldsymbol{\alpha}) = (H, \boldsymbol{\alpha}_0, \boldsymbol{\alpha}_0)A^{-1}$. The vacuum is also diagonal in this set up.

Returning to the FSM framon vacuum, in the $(T_0, \boldsymbol{\alpha}_0, \boldsymbol{\alpha}_0)$ set up [19] finds that minimising the framon potential leads to a diagonal vacuum,

$$\Phi_{Vac}(\boldsymbol{\alpha}_0) = \zeta_S \begin{pmatrix} \sqrt{\frac{1+2R}{3}} & 0 & 0 \\ 0 & \sqrt{\frac{1-R}{3}} & 0 \\ 0 & 0 & \sqrt{\frac{1-R}{3}} \end{pmatrix}, \tag{5.26}$$

where

$$R = \frac{\nu_2 \zeta_W^2}{2\kappa_S \zeta_S^2}. \tag{5.27}$$

A general vacuum, i.e., in the $(T_0, \boldsymbol{\alpha}_0, \boldsymbol{\alpha})$ set up, is obtained by acting on the right with a general global $\widetilde{su}(3)$ transformation,

$$\Phi_{Vac}(\boldsymbol{\alpha}) = \Phi_{Vac}(\boldsymbol{\alpha}_0)A^{-1}, \tag{5.28}$$

where A is given by

$$A = R_1 \begin{pmatrix} \cos\theta e^{-i\beta_1} & -\frac{\cos\theta\sin\theta\sin\phi e^{i(\beta_2-\beta_1)}}{\sqrt{\cos^2\theta+\sin^2\theta\cos^2\phi}} & -\frac{\sin\theta\cos\phi e^{i\beta_3}}{\sqrt{\cos^2\theta+\sin^2\theta\cos^2\phi}} \\ \sin\theta\sin\phi e^{-i\beta_2} & \sqrt{\cos^2\theta+\sin^2\theta\cos^2\phi} & 0 \\ \sin\theta\cos\phi e^{-i\beta_3} & -\frac{\sin^2\theta\cos\phi\sin\phi e^{i(\beta_2-\beta_3)}}{\sqrt{\cos^2\theta+\sin^2\theta\cos^2\phi}} & \frac{\cos\theta e^{i\beta_1}}{\sqrt{\cos^2\theta+\sin^2\theta\cos^2\phi}} \end{pmatrix}. \quad (5.29)$$

We do not explicitly write R_1, which can be written in the form

$$R_1 = \left(\begin{array}{c|c} 1 & 0 \\ \hline 0 & R_1^{2\times 2} \end{array}\right), \quad (5.30)$$

since in the calculations that follow we will be interested in the combination $A^{-1}\boldsymbol{\alpha}_0$. The factor R_1^{-1} has no effect on $\boldsymbol{\alpha}_0 = (1,0,0)^\dagger$. We will note here, and use the fact later, that

$$A^{-1}\boldsymbol{\alpha}_0 = \begin{pmatrix} \cos\theta e^{i\beta_1} \\ -\frac{\cos\theta\sin\theta\sin\phi e^{i(\beta_1-\beta_2)}}{\sqrt{\cos^2\theta+\sin^2\theta\cos^2\phi}} \\ -\frac{\sin\theta\cos\phi e^{-i\beta_3}}{\sqrt{\cos^2\theta+\sin^2\theta\cos^2\phi}} \end{pmatrix}. \quad (5.31)$$

This parameterisation has the benefit that a general $\boldsymbol{\alpha}$ has a convenient form,

$$\boldsymbol{\alpha} = A\boldsymbol{\alpha}_0 = R_1 \begin{pmatrix} \cos\theta e^{-i\beta_1} \\ \sin\theta\sin\phi e^{-i\beta_2} \\ \sin\theta\cos\phi e^{-i\beta_3} \end{pmatrix}. \quad (5.32)$$

5.2 The FSM Strong Framon Fields

In writing the vacuum as we have in equation (5.26) we have implicitly chosen a coordinate frame where orthonormal fluctuations around the vacuum appear as

$$\Phi = \begin{pmatrix} \zeta_S\sqrt{\frac{1+2R}{3}} + \delta\phi_1^{\tilde{1}} & \delta\phi_1^{\tilde{2}} e^{i\chi_3} & \delta\phi_1^{\tilde{3}} e^{i\chi_2} \\ \delta\phi_2^{\tilde{1}} e^{-i\chi_3} & \zeta_S\sqrt{\frac{1-R}{3}} + \delta\phi_2^{\tilde{2}} & \delta\phi_2^{\tilde{3}} e^{i\chi_1} \\ \delta\phi_3^{\tilde{1}} e^{-i\chi_2} & \delta\phi_3^{\tilde{2}} e^{-i\chi_1} & \zeta_S\sqrt{\frac{1-R}{3}} + \delta\phi_3^{\tilde{3}} \end{pmatrix}, \quad (5.33)$$

with $\delta\phi_j^{\tilde{i}} \in \mathbb{C}$. The phase factors $e^{i\chi_i}$ are an arbitrary rotation of these bases, which we are free to perform. Later they will be fixed to simplify the algebra. However, we want to fix the gauge and work with the 9 degrees of freedom which are physical. To work with physical fluctuations in the $(T_0, \boldsymbol{\alpha}_0, \boldsymbol{\alpha}_0)$ gauge we need to act on Φ with

$$\Omega = \begin{pmatrix} 1 - \frac{i}{\zeta_S}\sqrt{\frac{3}{1+2R}}\delta\phi_{1I}^{\tilde{1}} & \frac{1}{\zeta_S}\sqrt{\frac{3}{1+2R}}\delta\phi_2^{\tilde{1}*}e^{i\chi_3} & \frac{1}{\zeta_S}\sqrt{\frac{3}{1+2R}}\delta\phi_3^{\tilde{1}*}e^{i\chi_2} \\ -\frac{1}{\zeta_S}\sqrt{\frac{3}{1+2R}}\delta\phi_2^{\tilde{1}}e^{-i\chi_3} & 1 - \frac{i}{\zeta_S}\sqrt{\frac{3}{1-R}}\delta\phi_{2I}^{\tilde{2}} & \frac{1}{\zeta_S}\sqrt{\frac{3}{1-R}}\delta\phi_3^{\tilde{2}*}e^{i\chi_1} \\ -\frac{1}{\zeta_S}\sqrt{\frac{3}{1+2R}}\delta\phi_3^{\tilde{1}}e^{-i\chi_2} & -\frac{1}{\zeta_S}\sqrt{\frac{3}{1-R}}\delta\phi_3^{\tilde{2}}e^{-i\chi_1} & 1 - \frac{i}{\zeta_S}\sqrt{\frac{3}{1-R}}\delta\phi_{3I}^{\tilde{3}} \end{pmatrix}, \tag{5.34}$$

i.e., $\Phi' = \Omega\Phi$, to give the fluctuations in the $(T_0, \boldsymbol{\alpha}_0, \boldsymbol{\alpha}_0)$ gauge:

$$\Phi' = \begin{pmatrix} \zeta_S\sqrt{\frac{1+2R}{3}} + h_1 & \eta_3 & \eta_2 \\ 0 & \zeta_S\sqrt{\frac{1-R}{3}} + h_2 & \eta_1 \\ 0 & 0 & \zeta_S\sqrt{\frac{1-R}{3}} + h_3 \end{pmatrix}, \tag{5.35}$$

where $h_1, h_2, h_3 \in \mathbb{R}$ and $\eta_1, \eta_2, \eta_3 \in \mathbb{C}$. With this transformation we can identify

$$\tilde{h}_1 = \delta\phi_{1R}^{\tilde{1}}, \tag{5.36}$$
$$\tilde{h}_2 = \delta\phi_{2R}^{\tilde{2}}, \tag{5.37}$$
$$\tilde{h}_3 = \delta\phi_{3R}^{\tilde{3}}, \tag{5.38}$$
$$\tilde{\eta}_{1R} = \delta\phi_{2R}^{\tilde{3}}e^{i\chi_1} + \delta\phi_{3R}^{\tilde{2}}e^{-i\chi_1}, \tag{5.39}$$
$$\tilde{\eta}_{1I} = \delta\phi_{2I}^{\tilde{3}}e^{i\chi_1} - \delta\phi_{3I}^{\tilde{2}}e^{-i\chi_1}, \tag{5.40}$$
$$\tilde{\eta}_{2R} = \delta\phi_{1R}^{\tilde{3}}e^{i\chi_2} + \sqrt{\frac{1-R}{1+2R}}\delta\phi_{3R}^{\tilde{1}}e^{-i\chi_2}, \tag{5.41}$$
$$\tilde{\eta}_{2I} = \delta\phi_{1I}^{\tilde{3}}e^{i\chi_2} - \sqrt{\frac{1-R}{1+2R}}\delta\phi_{3I}^{\tilde{1}}e^{-i\chi_2}, \tag{5.42}$$
$$\tilde{\eta}_{3R} = \delta\phi_{1R}^{\tilde{2}}e^{i\chi_3} + \sqrt{\frac{1-R}{1+2R}}\delta\phi_{2R}^{\tilde{1}}e^{-i\chi_3}, \tag{5.43}$$
$$\tilde{\eta}_{3I} = \delta\phi_{1I}^{\tilde{2}}e^{i\chi_3} - \sqrt{\frac{1-R}{1+2R}}\delta\phi_{2I}^{\tilde{1}}e^{-i\chi_3}. \tag{5.44}$$

Although the original fluctuations (e.g., $\delta\phi_{jR}^{\tilde{i}}$) were orthonormal, these fluctuations are orthogonal but not normalised. We thus normalise them to give

$$h_1 = \delta\phi^{\tilde{1}}_{1R}, \tag{5.45}$$

$$h_2 = \delta\phi^{\tilde{2}}_{2R}, \tag{5.46}$$

$$h_3 = \delta\phi^{\tilde{3}}_{3R}, \tag{5.47}$$

$$\eta_{1R} = \frac{\delta\phi^{\tilde{3}}_{2R}e^{i\chi_1}}{\sqrt{2}} + \frac{\delta\phi^{\tilde{2}}_{3R}}{\sqrt{2}}e^{-i\chi_1}, \tag{5.48}$$

$$\eta_{1I} = \frac{\delta\phi^{\tilde{3}}_{2I}e^{i\chi_1}}{\sqrt{2}} - \frac{\delta\phi^{\tilde{2}}_{3I}}{\sqrt{2}}e^{-i\chi_1}, \tag{5.49}$$

$$\eta_{2R} = \sqrt{\frac{1+2R}{2+R}}\delta\phi^{\tilde{3}}_{1R}e^{i\chi_2} + \sqrt{\frac{1-R}{2+R}}\delta\phi^{\tilde{1}}_{3R}e^{-i\chi_2}, \tag{5.50}$$

$$\eta_{2I} = \sqrt{\frac{1+2R}{2+R}}\delta\phi^{\tilde{3}}_{1I}e^{i\chi_2} - \sqrt{\frac{1-R}{2+R}}\delta\phi^{\tilde{1}}_{3I}e^{-i\chi_2}, \tag{5.51}$$

$$\eta_{3R} = \sqrt{\frac{1+2R}{2+R}}\delta\phi^{\tilde{2}}_{1R}e^{i\chi_3} + \sqrt{\frac{1-R}{2+R}}\delta\phi^{\tilde{1}}_{2R}e^{-i\chi_3}, \tag{5.52}$$

$$\eta_{3I} = \sqrt{\frac{1+2R}{2+R}}\delta\phi^{\tilde{2}}_{1I}e^{i\chi_3} - \sqrt{\frac{1-R}{2+R}}\delta\phi^{\tilde{1}}_{2I}e^{-i\chi_3}. \tag{5.53}$$

We can then represent these framon fields as 3×3 complex matrices:

$$V_1 = \begin{pmatrix} 1 & 0 & 0 \\ 0 & 0 & 0 \\ 0 & 0 & 0 \end{pmatrix}, \tag{5.54}$$

$$V_2 = \begin{pmatrix} 0 & 0 & 0 \\ 0 & 1 & 0 \\ 0 & 0 & 0 \end{pmatrix}, \tag{5.55}$$

$$V_3 = \begin{pmatrix} 0 & 0 & 0 \\ 0 & 0 & 0 \\ 0 & 0 & 1 \end{pmatrix}, \tag{5.56}$$

$$V_4 = \begin{pmatrix} 0 & \sqrt{\frac{1+2R}{2+R}}e^{i\chi_3} & 0 \\ \sqrt{\frac{1-R}{2+R}}e^{-i\chi_3} & 0 & 0 \\ 0 & 0 & 0 \end{pmatrix}, \tag{5.57}$$

$$V_5 = \begin{pmatrix} 0 & 0 & \sqrt{\frac{1+2R}{2+R}}e^{i\chi_2} \\ 0 & 0 & 0 \\ \sqrt{\frac{1-R}{2+R}}e^{-i\chi_2} & 0 & 0 \end{pmatrix}, \tag{5.58}$$

$$V_6 = \begin{pmatrix} 0 & 0 & 0 \\ 0 & 0 & \frac{e^{i\chi_1}}{\sqrt{2}} \\ 0 & \frac{e^{-i\chi_1}}{\sqrt{2}} & 0 \end{pmatrix}, \tag{5.59}$$

$$V_7 = i \begin{pmatrix} 0 & \sqrt{\frac{1+2R}{2+R}}e^{i\chi_3} & 0 \\ -\sqrt{\frac{1-R}{2+R}}e^{-i\chi_3} & 0 & 0 \\ 0 & 0 & 0 \end{pmatrix}, \tag{5.60}$$

$$V_8 = i \begin{pmatrix} 0 & 0 & \sqrt{\frac{1+2R}{2+R}}e^{i\chi_2} \\ 0 & 0 & 0 \\ -\sqrt{\frac{1-R}{2+R}}e^{-i\chi_2} & 0 & 0 \end{pmatrix}, \tag{5.61}$$

$$V_9 = i \begin{pmatrix} 0 & 0 & 0 \\ 0 & 0 & \frac{e^{i\chi_1}}{\sqrt{2}} \\ 0 & -\frac{e^{-i\chi_1}}{\sqrt{2}} & 0 \end{pmatrix}. \tag{5.62}$$

5.3 Introducing the fermion fields

The FSM makes progress in suggesting a geometric origin for the scalar fields, but the fermion fields must still be put in by hand. The FSM introduces the following fermion fields:

$$\psi_R^{(-\frac{1}{2})} = \psi_R^{(-\frac{1}{2})}(\mathbf{1},\mathbf{1}), \tag{5.63}$$

$$\psi_{Lr}^{(-\frac{1}{2})} = \psi_L^{(-\frac{1}{2})}(\mathbf{2},\mathbf{1}), \tag{5.64}$$

$$\psi_{Ra}^{(1/6)} = \psi_R^{(1/6)}(\mathbf{1},\mathbf{3}), \tag{5.65}$$

$$\psi_{Lra}^{(1/6)} = \psi_L^{(1/6)}(\mathbf{2},\mathbf{3}), \tag{5.66}$$

where the $u(1)$ charge q is given in the superscript and $su(2)$ and $su(3)$ representations are given as the first and second entries in the brackets, respectively.

It has been shown by 't Hooft [28] and Banks and Robinovici [5] that a theory with $su(2)$ symmetry breaking is equivalent to the lowest bound states of a similar theory with $su(2)$ confinement. The FSM uses $su(2)$ confinement rather than symmetry breaking. Since $su(2)$ confinement has not been seen in experiment the FSM assumes that it is much deeper than $su(3)$ confinement. Current experimental energies probe what we will call the standard model scenario. In this regime only $su(2)$ bound states can be seen, such as

$$\sum_r \phi_r^{\tilde{r}*}\psi_{Lr} \tag{5.67}$$

and

$$\sum_r \phi_r^{\tilde{r}*}\psi_{Lra}. \tag{5.68}$$

We can now write out the representations associated with these bound states, table 5.1. The top section of this table shows pure framon bound states. There is one scalar coming the weak framons and an $\widetilde{su}(3)$ nonet coming from the strong framons. The second section shows bound states of the weak framons and gauge fields. The weak framons are labelled by their $u(1)$ charge rather than with $\tilde{r}$. As they have both a non-trivial $u(1)$ and $su(2)$ representation they couple to the $u(1)$ and $su(2)$ gauge fields. The situation is more complex than represented in the table, in that the physical photon is a mixture of γ and $\boldsymbol{\phi}^{(\pm\frac{1}{2})\dagger}(B_\mu^i\tau_i)\boldsymbol{\phi}_r^{(\pm\frac{1}{2})}$. In the third section we see the coupling of the weak framons to the left handed fermions.

Table 5.2 shows the standard model particle spectrum. We see that we can identify the states as in table 5.3 with the index $\tilde{a}$ playing the role of generation number. Note that the baryon minus lepton number is given by

$$(B-L) = 2(q+\tilde{q}). \tag{5.69}$$

Global conservation of q and $\tilde{q}$ is seen to imply global baryon minus lepton number conservation.

The FSM proposes

$$\mathcal{L}_{\rm YK}^{\rm weak} = \sum_{[\tilde{a}],[b]} Y_{[b]}\bar{\psi}^r_{[\tilde{a}]}\alpha^{\tilde{a}}\phi_r^{\tilde{r}=1}\frac{1}{2}(1+\gamma_5)\psi^{[b]} + \sum_{[\tilde{a}],[b]} Y'_{[b]}\bar{\psi}^r_{[\tilde{a}]}\alpha^{\tilde{a}}\phi_r^{\tilde{r}=2}\frac{1}{2}(1+\gamma_5)\psi'^{[b]} + \text{h.c.} \tag{5.70}$$

as the Yukawa terms for the weak framons and leptons, where the indices in brackets $[\tilde{a}]$ and $[\tilde{b}]$ are three identical copies of the same fields. The Yukawa terms for the quarks are the same with $\psi^{[b]}$ replaced with $\psi_a^{[b]}$. The coupling to the strong framons is

$$\mathcal{L}_{\rm YK}^{\rm strong} = \sum_{[b]} Z_{[b]}\bar{\psi}^a\phi_a\cdot\boldsymbol{\alpha}_0\frac{1}{2}(1+\gamma_5)\psi^{[b]} + \text{h.c.} \tag{5.71}$$

In the next section we transform the strong framon coupling terms so the coupling matrix is hermitian. We have seen above that the weak framon in FSM can be identified with the Higgs boson in the standard model. When the same procedure is performed on equation (5.70) we recover the Yukawa couplings assumed in part I, equation (4.1).

	q	$su(2)$	$su(3)$	$\tilde{q}$	$\widetilde{su}(2)$	$\widetilde{su}(3)$	Field Content
$\sum_{r,\tilde{r}} \phi_r^{\tilde{r}*}\phi_r^{\tilde{r}}$	0	**1**	**1**	0	**1**	**1**	1 scalar
$\sum_a \phi_a^{\tilde{a}*}\phi_a^{\tilde{b}}$	0	**1**	**1**	0	**1**	$\mathbf{8}\oplus\mathbf{1}$	9 scalars
γ	0	**1**	**1**	0	**1**	**1**	1 vector
$\boldsymbol{\phi}^{(+\frac{1}{2})\dagger}(B_\mu^i\tau_i)\boldsymbol{\phi}^{(-\frac{1}{2})}$	1	**1**	**1**	-1	} **3**	**1**	1 vector
$\boldsymbol{\phi}^{(-\frac{1}{2})\dagger}(B_\mu^i\tau_i)\boldsymbol{\phi}_r^{(+\frac{1}{2})}$	-1	**1**	**1**	1		**1**	1 vector
$\boldsymbol{\phi}^{(\pm\frac{1}{2})\dagger}(B_\mu^i\tau_i)\boldsymbol{\phi}_r^{(\pm\frac{1}{2})}$	0	**1**	**1**	0		**1**	1 vector
C_μ	0	**1**	**8**	0	**1**	**1**	8 vectors
$\sum_r \phi_r^{(+\frac{1}{2})\tilde{a}*}\psi_{Lr}^{(-\frac{1}{2})}$	0	**1**	**1**	$-\frac{1}{2}$	} **2**	**3**	3 spin $\frac{1}{2}$
$\sum_r \phi_r^{(-\frac{1}{2})\tilde{a}*}\psi_{Lr}^{(-\frac{1}{2})}$	-1	**1**	**1**	$\frac{1}{2}$		**3**	3 spin $\frac{1}{2}$
$\sum_r \phi_r^{(+\frac{1}{2})\tilde{a}*}\psi_{Lra}^{(\frac{1}{6})}$	$\frac{2}{3}$	**1**	**3**	$-\frac{1}{2}$	} **2**	**3**	9 spin $\frac{1}{2}$
$\sum_r \phi_r^{(-\frac{1}{2})\tilde{a}*}\psi_{Lra}^{(\frac{1}{6})}$	$-\frac{1}{3}$	**1**	**3**	$\frac{1}{2}$		**3**	9 spin $\frac{1}{2}$
+ right handed counterparts							

Table 5.1: The FSM lowest $su(2)$ bound states and their representations. See text for details, especially for notes on the mixing of γ and $\boldsymbol{\phi}^{(\pm\frac{1}{2})\dagger}(B_\mu^i\tau_i)\boldsymbol{\phi}_r^{(\pm\frac{1}{2})}$.

	Electric Charge	$su(2)$	$su(3)$	Field Content
H	0	**1**	**1**	1 scalar
W_μ^+	1	} $\mathbf{3}\oplus\mathbf{1}$	**1**	1 vector
W_μ^-	-1		**1**	1 vector
Z^0, γ	0		**1**	2 vectors
C_μ	0	**1**	**8**	8 vectors
$\nu_{eL}, \nu_{\mu L}, \nu_{\tau L}$	0	} **2**	**1**	3 spin $\frac{1}{2}$
e_L, μ_L, τ_L	-1		**1**	3 spin $\frac{1}{2}$
u_L, c_L, t_L	$\frac{2}{3}$	} **2**	**3**	9 spin $\frac{1}{2}$
d_L, s_L, b_L	$-\frac{1}{3}$		**3**	9 spin $\frac{1}{2}$
+ right handed counterparts				

Table 5.2: The standard model field content after spontaneous symmetry breaking.

FSM	SM	$2(q+\tilde{q})$
$\sum_{r,\tilde{r}} \phi_r^{\tilde{r}*}\phi_r^{\tilde{r}}$	H	0
$\boldsymbol{\phi}^{(+\frac{1}{2})\dagger}(B_\mu^i\tau_i)\boldsymbol{\phi}^{(-\frac{1}{2})}$	W_μ^+	0
$\boldsymbol{\phi}^{(-\frac{1}{2})\dagger}(B_\mu^i\tau_i)\boldsymbol{\phi}_r^{(+\frac{1}{2})}$	W_μ^-	0
$\gamma,\ \boldsymbol{\phi}^{(\pm\frac{1}{2})\dagger}(B_\mu^i\tau_i)\boldsymbol{\phi}_r^{(\pm\frac{1}{2})}$	$\gamma,\ Z$	0
$\sum_r \phi_r^{(+\frac{1}{2})\tilde{a}*}\psi_{Lr}^{(-\frac{1}{2})}$	$\nu_{eL},\nu_{\mu L},\nu_{\tau L}$	-1
$\sum_r \phi_r^{(-\frac{1}{2})\tilde{a}*}\psi_{Lr}^{(-\frac{1}{2})}$	e_L^-,μ_L^-,τ_L^-	-1
$\sum_r \phi_r^{(+\frac{1}{2})\tilde{a}*}\psi_{Lra}^{(\frac{1}{6})}$	u_L,c_L,t_L	$\frac{1}{3}$
$\sum_r \phi_r^{(-\frac{1}{2})\tilde{a}*}\psi_{Lra}^{(\frac{1}{6})}$	d_L,s_L,b_L	$\frac{1}{3}$

Table 5.3: Identification of the FSM lowest $su(2)$ bound states and the standard model field content. Baryon minus lepton number is given by $2(q+\tilde{q})$.

5.4 The Tree Level Mass Matrix

In this section we will make the mass matrix hermitian as it will make the algebra simpler if we do not have to keep track of the fermion chirality so closely. Examination of the strong framon Yukawa couplings, equation (5.71), allows us to write, for the $(T_0, \boldsymbol{\alpha}_0, \boldsymbol{\alpha})$ set up,

$$\begin{aligned} m &= \Phi_{\rm Vac}(\boldsymbol{\alpha}_0)A^{-1}\boldsymbol{\alpha}_0(Z_{[1]},Z_{[2]},Z_{[3]}) \\ &= \zeta_S \begin{pmatrix} \sqrt{\frac{1+2R}{3}} & 0 & 0 \\ 0 & \sqrt{\frac{1-R}{3}} & 0 \\ 0 & 0 & \sqrt{\frac{1-R}{3}} \end{pmatrix} \begin{pmatrix} \cos\theta e^{i\beta_1} \\ -\frac{\cos\theta\sin\theta\sin\phi e^{i(\beta_1-\beta_2)}}{\sqrt{\cos^2\theta+\sin^2\theta\cos^2\phi}} \\ -\frac{\sin\theta\cos\phi e^{-i\beta_3}}{\sqrt{\cos^2\theta+\sin^2\theta\cos^2\phi}} \end{pmatrix} (Z_{[1]},Z_{[2]},Z_{[3]}) \\ &= \zeta_S \begin{pmatrix} \sqrt{\frac{1+2R}{3}}\cos\theta e^{i\beta_1} \\ -\sqrt{\frac{1-R}{3}}\frac{\cos\theta\sin\theta\sin\phi e^{i(\beta_1-\beta_2)}}{\sqrt{\cos^2\theta+\sin^2\theta\cos^2\phi}} \\ -\sqrt{\frac{1-R}{3}}\frac{\sin\theta\cos\phi e^{-i\beta_3}}{\sqrt{\cos^2\theta+\sin^2\theta\cos^2\phi}} \end{pmatrix} (Z_{[1]},Z_{[2]},Z_{[3]}). \end{aligned} \tag{5.72}$$

In section 2.1.1 we demonstrated that a mass matrix can be made hermitian,

$$m_W = mV^{-1}U, \tag{5.73}$$

via unitary matrices U and V. We can always choose a unitary V^{-1} so that

$$(Z_{[1]}, Z_{[2]}, Z_{[3]})V^{-1} = \rho_S \boldsymbol{\alpha}_0^\dagger, \tag{5.74}$$

where $\rho_S^2 = Z_{[1]}^2 + Z_{[2]}^2 + Z_{[3]}^2$. For $\boldsymbol{\alpha}_0^\dagger = (1,0,0)$ this is given by

$$V^{-1} = \frac{1}{\rho_S} \begin{pmatrix} Z_{[1]}^* & -\frac{Z_{[1]}^* Z_{[2]}}{\sqrt{|Z_{[1]}|^2+|Z_{[3]}|^2}} & -\frac{\rho_S Z_{[3]}}{\sqrt{|Z_{[1]}|^2+|Z_{[3]}|^2}} \\ Z_{[2]}^* & \sqrt{|Z_{[1]}|^2+|Z_{[3]}|^2} & 0 \\ Z_{[3]}^* & -\frac{Z_{[2]} Z_{[3]}^*}{\sqrt{|Z_{[1]}|^2+|Z_{[3]}|^2}} & \frac{\rho_S Z_{[1]}}{\sqrt{|Z_{[1]}|^2+|Z_{[3]}|^2}} \end{pmatrix} \tag{5.75}$$

so that

$$\begin{aligned} mV^{-1} &= \Phi_{\mathrm{Vac}}(\boldsymbol{\alpha}_0) A^{-1} \boldsymbol{\alpha}_0 (Z_{[1]}, Z_{[2]}, Z_{[3]}) V^{-1} \\ &= \rho_S \Phi_{\mathrm{Vac}}(\boldsymbol{\alpha}_0) A^{-1} \boldsymbol{\alpha}_0 \boldsymbol{\alpha}_0^\dagger \\ &= \zeta_S \rho_S |v_0\rangle \boldsymbol{\alpha}_0^\dagger, \end{aligned} \tag{5.76}$$

where we have introduced $|v_0\rangle := \frac{1}{\zeta_S} \Phi_{\mathrm{Vac}}(\boldsymbol{\alpha}_0) A^{-1} \boldsymbol{\alpha}_0$. Explicitly,

$$|v_0\rangle = \begin{pmatrix} \sqrt{\frac{1+2R}{3}} \cos\theta e^{i\beta_1} \\ -\sqrt{\frac{1-R}{3}} \frac{\cos\theta \sin\theta \sin\phi e^{i(\beta_1-\beta_2)}}{\sqrt{\cos^2\theta + \sin^2\theta \cos^2\phi}} \\ -\sqrt{\frac{1-R}{3}} \frac{\sin\theta \cos\phi e^{-i\beta_3}}{\sqrt{\cos^2\theta + \sin^2\theta \cos^2\phi}} \end{pmatrix}. \tag{5.77}$$

We now want to find a unitary matrix U such that $mV^{-1}U$ is hermitian. Now, since $\boldsymbol{\alpha}_0$ is just a vector of unit length, we know that $\exists U$ unitary such that

$$\boldsymbol{\alpha}_0^\dagger U = \frac{1}{v_0} \langle v_0|, \tag{5.78}$$

where $v_0^2 = \langle v_0 | v_0 \rangle$. Note that this does not define U uniquely, as $\boldsymbol{\alpha}_0$ is invariant to transformations by R_1. However, this is enough for us as we shall always use U in the combination $\boldsymbol{\alpha}_0^\dagger U$. We can now write

$$mV^{-1}U = m_W = \frac{\zeta_S \rho_S}{v_0} |v_0\rangle\langle v_0|. \tag{5.79}$$

5.5 The Strong Framon-Fermion Coupling Terms

Now we know how to make the mass matrix hermitian we want to find how this transformation changes the strong framon-fermion coupling constants. In equations (5.54) to (5.62) we found the first order orthonormal framon fields in the $(T_0, \boldsymbol{\alpha}_0, \boldsymbol{\alpha}_0)$

set up. The Yukawa term, with first order fluctuations around the vacuum, is then, in $(T_0, \boldsymbol{\alpha}_0, \boldsymbol{\alpha})$,

$$\mathcal{L}_{\rm YK} = \overline{\Psi}_L \Big(\Phi_{\rm Vac}(\boldsymbol{\alpha}_0) + \sum_j \delta\phi_j V_j \Big) A^{-1} \boldsymbol{\alpha}_0(Z_{[1]}, Z_{[2]}, Z_{[3]}) \Psi^0_R + h.c. \tag{5.80}$$

We can act on the right with $V^{-1}U$ to make the vacuum mass matrix hermitian, but this will not in general make V_i hermitian. After acting with $V^{-1}U$ to redefine the right handed fields we will have

$$\begin{aligned} \mathcal{L}_{\rm YK} &= \overline{\Psi}_L \Big(\sum_j \delta\phi_j V_j \Big) A^{-1} \boldsymbol{\alpha}_0(Z_{[1]}, Z_{[2]}, Z_{[3]}) V^{-1} U \Psi_R + h.c. + \overline{\Psi} m_W \Psi \\ &= \sum_j \overline{\Psi}_L \Gamma_j \delta\phi_j \Psi_R + h.c. + \overline{\Psi} m_W \Psi, \end{aligned} \tag{5.81}$$

where we have rewritten the coupling in a compact notation

$$\Gamma_j = \frac{\rho_S}{v_0} |v_j\rangle\langle v_0| P_R + h.c. \tag{5.82}$$

and defined $|v_j\rangle := V_j A^{-1} \boldsymbol{\alpha}_0$. Explicitly, we have

$$|v_1\rangle = \begin{pmatrix} \cos\theta e^{i\beta_1} \\ 0 \\ 0 \end{pmatrix}, \tag{5.83}$$

$$|v_2\rangle = \begin{pmatrix} 0 \\ -\frac{\cos\theta \sin\theta \sin\phi e^{i(\beta_1 - \beta_2)}}{\sqrt{\cos^2\theta + \sin^2\theta \cos^2\phi}} \\ 0 \end{pmatrix}, \tag{5.84}$$

$$|v_3\rangle = \begin{pmatrix} 0 \\ 0 \\ -\frac{\sin\theta \cos\phi e^{-i\beta_3}}{\sqrt{\cos^2\theta + \sin^2\theta \cos^2\phi}} \end{pmatrix}, \tag{5.85}$$

$$|v_4\rangle = \begin{pmatrix} -\sqrt{\frac{1+2R}{2+R}} \frac{\cos\theta \sin\theta \sin\phi e^{i(\beta_1 - \beta_2 + \chi_3)}}{\sqrt{\cos^2\theta + \sin^2\theta \cos^2\phi}} \\ \sqrt{\frac{1-R}{2+R}} \cos\theta e^{i(\beta_1 - \chi_3)} \\ 0 \end{pmatrix}, \tag{5.86}$$

$$|v_5\rangle = \begin{pmatrix} -\sqrt{\frac{1+2R}{2+R}} \frac{\sin\theta \cos\phi e^{i(\chi_2 - \beta_3)}}{\sqrt{\cos^2\theta + \sin^2\theta \cos^2\phi}} \\ 0 \\ \sqrt{\frac{1-R}{2+R}} \cos\theta e^{i(\beta_1 - \chi_2)} \end{pmatrix}, \tag{5.87}$$

$$|v_6\rangle = \begin{pmatrix} 0 \\ -\frac{\sin\theta\cos\phi e^{i(\chi_1-\beta_3)}}{\sqrt{2(\cos^2\theta+\sin^2\theta\cos^2\phi)}} \\ -\frac{\cos\theta\sin\theta\sin\phi e^{i(\beta_1-\beta_2-\chi_1)}}{\sqrt{2(\cos^2\theta+\sin^2\theta\cos^2\phi)}} \end{pmatrix}, \tag{5.88}$$

$$|v_7\rangle = i\begin{pmatrix} -\sqrt{\frac{1+2R}{2+R}}\frac{\cos\theta\sin\theta\sin\phi e^{i(\beta_1-\beta_2+\chi_3)}}{\sqrt{\cos^2\theta+\sin^2\theta\cos^2\phi}} \\ -\sqrt{\frac{1-R}{2+R}}\cos\theta e^{i(\beta_1-\chi_3)} \\ 0 \end{pmatrix}, \tag{5.89}$$

$$|v_8\rangle = i\begin{pmatrix} -\sqrt{\frac{1+2R}{2+R}}\frac{\sin\theta\cos\phi e^{i(\chi_2-\beta_3)}}{\sqrt{\cos^2\theta+\sin^2\theta\cos^2\phi}} \\ 0 \\ -\sqrt{\frac{1-R}{2+R}}\cos\theta e^{i(\beta_1-\chi_2)} \end{pmatrix}, \tag{5.90}$$

$$|v_9\rangle = i\begin{pmatrix} 0 \\ -\frac{\sin\theta\cos\phi e^{i(\chi_1-\beta_3)}}{\sqrt{2(\cos^2\theta+\sin^2\theta\cos^2\phi)}} \\ \frac{\cos\theta\sin\theta\sin\phi e^{i(\beta_1-\beta_2-\chi_1)}}{\sqrt{2(\cos^2\theta+\sin^2\theta\cos^2\phi)}} \end{pmatrix}. \tag{5.91}$$

We will later be interested in quantities such as $\langle v_0|v_j\rangle$ and $\langle v_j|v_j\rangle$ so it will simplify the algebra if we can remove the phase dependence of these inner products. Notice that if we set

$$\chi_1 = \beta_1 + \beta_3 - \beta_2, \tag{5.92}$$

$$\chi_2 = \beta_1 + \beta_3, \tag{5.93}$$

$$\chi_3 = \beta_2, \tag{5.94}$$

then the phase of each component agrees with the phases in $|v_0\rangle$, equation (5.77), so any phases will cancel out of each term in the inner product.

5.6 The Strong Framon Contribution to the Fermion Self Energy

We now want to find the contribution to the fermion mass from interaction with the strong framon fields. It was argued in [7] that this is the most important contribution to the rotation of the mass matrix in a similar model. Also, with a reinterpretation of the parameters this contribution has many of the properties of a general massive intermediary, since the strong Higgs are hadrons and so they have a broad width. We will here only consider the one-loop correction:

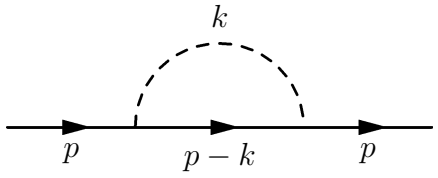

Standard Feynman rules give the contribution for each strong framon field, $\Sigma_j(p)$, with coupling Γ_j and mass M_j, to be:

$$\begin{aligned}\Sigma_j(p) &= \frac{i}{(2\pi)^4}\int d^Dk \frac{1}{k^2-M_j^2}\Gamma_j \frac{(\not{p}-\not{k})+m}{(p-k)^2-m^2+i\epsilon}\Gamma_j \\ &= \frac{i}{(2\pi)^4}\Gamma_j \int d^Dk \int_0^1 dz \frac{(\not{p}-\not{k})+m}{(k^2-M_j^2+(p^2-2pk-m^2+M_j^2)z+i\epsilon)^2}\Gamma_j, \quad (5.95)\end{aligned}$$

where we will use dimensional requlariza tion, so $D = 4-\eta$, and we have used a trick due to Feynman to combine the denomintors. We now change variables using $q = k - pz$

$$\begin{aligned}\Sigma_j(p) &= \frac{i}{(2\pi)^4}\Gamma_j \int_0^1 dz \int d^Dq \frac{m-(\not{q}+\not{p}z)+\not{p}}{(q^2-p^2z^2-M_j^2+(p^2-m^2M_j^2)z+i\epsilon)^2}\Gamma_j \\ &= \frac{i}{(2\pi)^4}\Gamma_j \int_0^1 dz(m+\not{p}(1-z))\cdot i\pi^{\frac{D}{2}}\frac{\Gamma(\eta-\frac{D}{2})}{\Gamma(\eta)(Q^2)^{\eta-\frac{D}{2}}}\Gamma_j, \quad (5.96)\end{aligned}$$

where $Q^2 = p^2z(1-z)+M_j^2(z-1)-m^2z$ and $\Gamma(x)$ denotes the gamma function. Now we let $\eta \to 0$,

$$\begin{aligned}\Sigma_j(p) &= \frac{-\pi^2}{(2\pi)^4}\Gamma_j \int_0^1 dz(m+\not{p}(1-z))\left(\frac{2}{\eta}-\gamma+\cdots\right)\left(1-\frac{\eta}{2}\ln\left(\frac{Q^2}{\mu^2}\right)+\cdots\right)\Gamma_j \\ &= -\frac{\Gamma_j}{16\pi^2}\int_0^1 dz(m+\not{p}(1-z))\left(C-\ln\left(\frac{Q^2}{\mu^2}\right)+\cdots\right)\Gamma_j, \quad (5.97)\end{aligned}$$

where C is an infinite constant to be subtracted. To maintain the hermiticity of the contribution we must put half of $\not{p}$ to the left and half to the right by splitting it $\not{p} = \frac{1}{2}(\not{p}+\not{p})$. Note that $\not{p}$ does not commute with $P_{R,L}$ and m does not commute with $|v_j\rangle\langle v_0|$. Using $\not{p}P_R = P_L\not{p}$, $P_{R,L}^2 = P_{R,L}$, $P_RP_L = 0$,

$$\Gamma_j = \frac{\rho_S}{v_0}|v_j\rangle\langle v_0|P_R + h.c., \quad (5.98)$$

and subtracting the constants we get

$$\begin{aligned}
\Sigma(p) &= \sum_j \Sigma_j(p) \\
&= \frac{1}{16\pi^2}\sum_j \int_0^1 dz \Gamma_j \ln(\mu^2) \left(\left(\frac{\not{p}}{2} + \frac{\not{p}}{2} \right)(1-z) + m \right) \Gamma_j \\
&= \frac{1}{16\pi^2}\sum_j \int_0^1 dz \ln(\mu^2) \Bigg[\Gamma_j m \Gamma_j + \\
&\quad + (1-z)\frac{\rho_S^2}{v_0^2} \Bigg(\frac{\not{p}}{2} \Big(|v_j\rangle\langle v_0|v_0\rangle\langle v_j| P_L + |v_0\rangle\langle v_j|v_j\rangle\langle v_0| P_R \Big) + \\
&\quad + \Big(|v_j\rangle\langle v_0|v_0\rangle\langle v_j| P_R + |v_0\rangle\langle v_j|v_j\rangle\langle v_0| P_L \Big) \frac{\not{p}}{2} \Bigg) \Bigg].
\end{aligned} \tag{5.99}$$

Taking $\not{p} = m$ results in

$$\begin{aligned}
\Sigma(p)|_{\not{p}=m} &= \frac{1}{16\pi^2}\frac{\rho_S^2}{v_0^2}\sum_j \int_0^1 dz \ln(\mu^2) \Bigg[|v_j\rangle\langle v_0|m|v_j\rangle\langle v_0| P_R + \\
&\quad + \frac{(1-z)}{2} \left(|v_j\rangle\langle v_0|v_0\rangle\langle v_j| m P_R + m |v_0\rangle\langle v_j|v_j\rangle\langle v_0| P_R \right) \Bigg] + h.c. \\
&= \frac{\ln\mu^2}{16\pi^2}\frac{\rho_S^2}{v_0^2}\sum_j \Bigg[|v_j\rangle\langle v_0|m|v_j\rangle\langle v_0| P_R + \\
&\quad + \frac{1}{4}\Bigg(|v_j\rangle\langle v_0|v_0\rangle\langle v_j| m P_R + m |v_0\rangle\langle v_j|v_j\rangle\langle v_0| P_R \Bigg) \Bigg] + h.c.
\end{aligned} \tag{5.100}$$

We can now insert $m = \frac{\zeta_S \rho_S}{v_0} |v_0\rangle\langle v_0|$ to give

$$\begin{aligned}
\Sigma(p)|_{\not{p}=m} = \frac{\ln\mu^2}{16\pi^2}\frac{\zeta_S \rho_S^3}{v_0^3}\sum_j \Bigg[& |v_j\rangle\langle v_0|v_0\rangle\langle v_0|v_j\rangle\langle v_0| P_R + \\
& \frac{1}{4}\Bigg(|v_j\rangle\langle v_0|v_0\rangle\langle v_j|v_0\rangle\langle v_0| P_R + |v_0\rangle\langle v_0|v_0\rangle\langle v_j|v_j\rangle\langle v_0| P_R \Bigg) \Bigg] + h.c.
\end{aligned} \tag{5.101}$$

In evaluating these six terms it is useful to separate the contributions coming from $\Gamma_{1\ldots6}$ and $\Gamma_{7,8,9}$. The phases in each component of $|v_j\rangle$ agree so we will call $V_{1\ldots6}$ and $V_{7,8,9}$ 'real' and 'imaginary' framon fields respectively, though of course this is only accurate if $\beta_1 = \beta_2 = \beta_3 = 0$. In appendix A.2 we show that

$$\sum_{j=1\ldots6} \langle v_0|v_j\rangle|v_j\rangle = |v_0\rangle. \tag{5.102}$$

We can then define $|gvI\rangle := \sum_{j=7,8,9}\langle v_0|v_j\rangle|v_j\rangle$ so that $\sum_j\langle v_0|v_j\rangle|v_j\rangle = |v_0\rangle + |gvI\rangle$ and $\sum_j\langle v_j|v_0\rangle|v_j\rangle = |v_0\rangle - |gvI\rangle$. Finally, using $\delta m = -\Sigma(p)|_{\not{p}=m}$, we get

$$\delta m = -\frac{\ln(\mu^2)}{16\pi^2}\frac{\zeta_S\rho_S^3}{v_0}\left(\frac{5}{4}|v_0\rangle + \frac{3}{4}|gvI\rangle + \frac{1}{4}\left(\sum_j\langle v_j|v_j\rangle\right)|v_0\rangle\right)\langle v_0|P_R + h.c. \tag{5.103}$$

The Yukawa term in the Lagrangian can now be written

$$\mathcal{L}_{\mathrm{YK}} \;=\; \overline{\Psi}m\Psi \tag{5.104}$$

with

$$m = \frac{\zeta_S\rho_S}{v_0}|v_0\rangle\langle v_0|P_R + h.c. + \delta m. \tag{5.105}$$

We can see that

$$\frac{d}{d\ln\mu^2}(m) = -\frac{1}{16\pi^2}\frac{\zeta_S\rho_S^3}{v_0}\left(\frac{5}{4}|v_0\rangle + \frac{3}{4}|gvI\rangle + \frac{1}{4}\left(\sum_j\langle v_j|v_j\rangle\right)|v_0\rangle\right)\langle v_0|P_R + h.c. \tag{5.106}$$

5.7 The One-Loop Mass Matrix RGE

Although this gives the behaviour of the mass matrix with scale, we want to extract from this the behaviour of the variables $R, \theta, \phi, \beta_1, \beta_2$ and β_3. Note that the $\frac{\rho_S}{v_0}\langle v_0|P_R$ part of the mass matrix does not change with scale, so we can capture the behaviour of these variables under renormalisation by considering only

$$\frac{d}{d\ln\mu^2}(\zeta_S|v_0\rangle) = -\frac{\zeta_S\rho_S^2}{16\pi^2}\left(\frac{5}{4}|v_0\rangle + \frac{3}{4}|gvI\rangle + \frac{1}{4}\left(\sum_j\langle v_j|v_j\rangle\right)|v_0\rangle\right). \tag{5.107}$$

We know that the rank-one mass matrix can be parameterised by $R, \theta, \phi, \beta_1, \beta_2$ and β_3, so by using the chain rule we can write

$$\frac{d}{d\ln\mu^2}(\zeta_S|v_0\rangle) = \dot{\zeta}_S\frac{\partial}{\partial\zeta_S}(\zeta_S|v_0\rangle) + \dot{\theta}\frac{\partial}{\partial\theta}(\zeta_S|v_0\rangle) + \dot{\phi}\frac{\partial}{\partial\phi}(\zeta_S|v_0\rangle) + \dot{\beta}_1\frac{\partial}{\partial\beta_1}(\zeta_S|v_0\rangle) + \dot{\beta}_2\frac{\partial}{\partial\beta_2}(\zeta_S|v_0\rangle) + \dot{\beta}_3\frac{\partial}{\partial\beta_3}(\zeta_S|v_0\rangle), \tag{5.108}$$

where a dot denotes differentiation with respect to $\ln\mu^2$. Equating the right hand sides of (5.107) and (5.108) we can extract the renormalisation group equations for $R, \theta, \phi, \beta_1, \beta_2$ and β_3.

We can differentiate $\zeta_S|v_0\rangle$ directly to yield

$$\frac{\partial}{\partial\zeta_S}(\zeta_S|v_0\rangle) = \frac{1}{\sqrt{3}}\begin{pmatrix} \frac{1}{\sqrt{1+2R}}\cos\theta e^{i\beta_1} \\ -\frac{1}{\sqrt{1-R}}\frac{\sin\theta\cos\theta\sin\phi}{\sqrt{\cos^2\theta+\sin^2\theta\cos^2\phi}}e^{-i\beta_2+i\beta_1} \\ -\frac{1}{\sqrt{1-R}}\frac{\sin\theta\cos\phi}{\sqrt{\cos^2\theta+\sin^2\theta\cos^2\phi}}e^{-i\beta_3} \end{pmatrix}, \tag{5.109}$$

$$\frac{\partial}{\partial\theta}(\zeta_S|v_0\rangle) = \frac{\zeta_S}{\sqrt{3}}\begin{pmatrix} -\sqrt{1+2R}\sin\theta e^{i\beta_1} \\ -\sqrt{1-R}\frac{\sin\phi(\cos^4\theta-\sin^4\theta\cos^2\phi)}{(\cos^2\theta+\sin^2\theta\cos^2\phi)^{3/2}}e^{-i\beta_2+i\beta_1} \\ -\sqrt{1-R}\frac{\cos\theta\cos\phi}{(\cos^2\theta+\sin^2\theta\cos^2\phi)^{3/2}}e^{-i\beta_3} \end{pmatrix}, \tag{5.110}$$

$$\frac{\partial}{\partial\phi}(\zeta_S|v_0\rangle) = \frac{\zeta_S}{\sqrt{3}}\begin{pmatrix} 0 \\ -\sqrt{1-R}\frac{\sin\theta\cos\theta\cos\phi}{(\cos^2\theta+\sin^2\theta\cos^2\phi)^{3/2}}e^{-i\beta_2+i\beta_1} \\ \sqrt{1-R}\frac{\sin\theta\cos^2\theta\sin\phi}{(\cos^2\theta+\sin^2\theta\cos^2\phi)^{3/2}}e^{-i\beta_3} \end{pmatrix}, \tag{5.111}$$

$$\frac{\partial}{\partial\beta_1}(\zeta_S|v_0\rangle) = \zeta_S\begin{pmatrix} i\sqrt{\frac{1+2R}{3}}\cos\theta e^{i\beta_1} \\ -i\sqrt{\frac{1-R}{3}}\frac{\sin\theta\cos\theta\sin\phi}{\sqrt{\cos^2\theta+\sin^2\theta\cos^2\phi}}e^{-i\beta_2+i\beta_1} \\ 0 \end{pmatrix}, \tag{5.112}$$

$$\frac{\partial}{\partial\beta_2}(\zeta_S|v_0\rangle) = \zeta_S\begin{pmatrix} 0 \\ i\sqrt{\frac{1-R}{3}}\frac{\sin\theta\cos\theta\sin\phi}{\sqrt{\cos^2\theta+\sin^2\theta\cos^2\phi}}e^{-i\beta_2+i\beta_1} \\ 0 \end{pmatrix}, \tag{5.113}$$

$$\frac{\partial}{\partial\beta_3}(\zeta_S|v_0\rangle) = \zeta_S\begin{pmatrix} 0 \\ 0 \\ i\sqrt{\frac{1-R}{3}}\frac{\sin\theta\cos\phi}{\sqrt{\cos^2\theta+\sin^2\theta\cos^2\phi}}e^{-i\beta_3} \end{pmatrix}. \tag{5.114}$$

Equating the right hand sides of (5.107) and (5.108) gives us three equations, one from each component of the vectors. We have noted before that the phases agree in each component of $|v_0\rangle$ and $|v_j\rangle$. When we equate (5.107) and (5.108) these factors cancel out of the equations. Also note that $\dot{\beta}_1, \dot{\beta}_2$ and $\dot{\beta}_3$ are proportional to i. Once the phases have cancelled out they are the only imaginary terms the equations. It thus must be the case that

$$\dot{\beta}_1 = \dot{\beta}_2 = \dot{\beta}_3 = 0. \tag{5.115}$$

The right hand side of equation (5.103) has two terms which we calculate in appendix A:

$$\sum_j \langle v_j | v_j \rangle = \frac{3}{2+R}(1+E), \tag{5.116}$$

where

$$E = 1 + 2R - 3R\cos^2\theta, \tag{5.117}$$

and

$$|gvI\rangle := \sum_{j=7,8,9} \langle v_0 | v_j \rangle | v_j \rangle = -\frac{3R\sin\theta\cos\theta}{2+R} \begin{pmatrix} \sqrt{\frac{1+2R}{3}}\sin\theta e^{i\beta_1} \\ \sqrt{\frac{1-R}{3}}\frac{\cos^2\theta\sin\phi}{\sqrt{\cos^2+\sin^2\theta\cos^2\phi}} e^{i\beta_1 - i\beta_2} \\ \sqrt{\frac{1-R}{3}}\frac{\cos\theta\cos\phi}{\sqrt{\cos^2+\sin^2\theta\cos^2\phi}} e^{-i\beta_3} \end{pmatrix}. \tag{5.118}$$

Finally, noticing that

$$\left(\frac{\partial}{\partial\zeta_S}(\zeta_S|v_0\rangle)\right) \cdot \left(\frac{\partial}{\partial\theta}(\zeta_S|v_0\rangle)\right)^\dagger = 0, \tag{5.119}$$

$$\left(\frac{\partial}{\partial\zeta_S}(\zeta_S|v_0\rangle)\right) \cdot \left(\frac{\partial}{\partial\phi}(\zeta_S|v_0\rangle)\right)^\dagger = 0, \tag{5.120}$$

$$\left(\frac{\partial}{\partial\theta}(\zeta_S|v_0\rangle)\right) \cdot \left(\frac{\partial}{\partial\phi}(\zeta_S|v_0\rangle)\right)^\dagger = 0, \tag{5.121}$$

we can take the inner product of equation (5.107) and each of these vectors to obtain the renormalisation group equations:

$$\dot{R} = \frac{\rho_S^2}{16\pi^2}\frac{R(1+2R)(1-R)}{E}\left[\frac{5}{2} + \frac{3(1+E)}{2(2+R)}\right], \tag{5.122}$$

$$\dot{\theta} = \frac{\rho_S^2}{16\pi^2}\frac{R\sin 2\theta}{E}\frac{3}{2}\left[\frac{5}{4} + \frac{3}{4(2+R)}\right], \tag{5.123}$$

$$\dot{\phi} = \frac{\rho_S^2}{16\pi^2}\frac{R\sin^2\theta\sin 2\phi}{E}\frac{3}{2}\left[\frac{5}{4} + \frac{3}{4(2+R)}\right], \tag{5.124}$$

$$\dot{\beta}_1 = \dot{\beta}_2 = \dot{\beta}_3 = 0. \tag{5.125}$$

Inspection of these equations yields the following fixed points:

	R	θ	ϕ
$F1$	0	any	any
$F2$	-1/2	0	any
$F3_1$	+1	$\pi/2$	0
$F3_2$	+1	$\pi/2$	$\pi/2$

We can determine the stability of these fixed points by studying the linearised flow in their neighbourhood. The linearised flow equations are

$$\dot{y_i} = M_{ij} y_j, \tag{5.126}$$

where $y_1 = R - R_*$, $y_2 = \theta - \theta_*$, $y_3 = \phi - \phi_*$, $*$ denotes a fixed point and

$$M = \left(\begin{array}{ccc} \partial_R \dot{R} & \partial_\theta \dot{R} & \partial_\phi \dot{R} \\ \partial_R \dot{\theta} & \partial_\theta \dot{\theta} & \partial_\phi \dot{\theta} \\ \partial_R \dot{\phi} & \partial_\theta \dot{\phi} & \partial_\phi \dot{\phi} \end{array} \right) \Bigg|_* . \tag{5.127}$$

The linearised flow equations are solved by $\tilde{y}_i = \mu^{2\lambda_i}$ where λ_i are the eigenvalues of M and $\tilde{y}$ are fluctuations along the eigenvectors. The sign of the eigenvalues thus tells us about the behaviour near the fixed point. Ignoring the $\rho_S^2/16\pi^2$ prefactor we get

	Eigenvalues			Stability
$F1$	4	0	0	stable as $\mu \to 0$
$F2$	-5	-1.75	0	stable as $\mu \to \infty$
$F3_1$	-4.5	-1.5	1.5	unstable
$F3_2$	-4.5	-1.5	-1.5	stable as $\mu \to \infty$

In the neighbourhood of $F3_2$ and F_2 the flow is directed towards these points as scale increases. Conversely, the flow is directed towards $F1$ in its neighbourhood as scale decreases. $F3_1$ is unstable, and in its neighbourhood the flow is directed away from this point as the scale increases or decreases. The zero eigenvalue in $F2$ arises as the coordinate system becomes degenerate at this point. This is reflected in the fact that there is a fixed point for any value of ϕ. The different values of ϕ label the same point.

Chapter 6

Modifications to the Mass Leakage Mechanism

Now that we have found the RGE for the mass matrix we are almost in a position to start considering whether the rotation can match experimental data. There are, however, two features of the FSM which we must investigate before we can employ the mass leakage mechanism.

We recall that the framons have the geometric meaning of frame vectors in the internal symmetry space, explored in [18]. The vector $\boldsymbol{\alpha}$, for which we now have a RGE, is a vector in $\widetilde{su}(3)$ space. The mass leakage mechanism requires us to take inner products in the internal symmetry space. Since, for a general vacuum, the strong framons are not orthonormal this implies that they will generate a non-trivial metric on the internal symmetry space which will have to be taken into account when taking inner products. In the first half of this chapter we will discuss the behaviour of this metric and how we modify the mass leakage mechanism to take it into account.

It has also been suggested [29] that there may be QCD effects which alter the single eigenvalue of the quark mass matrices as scales changes. The running of the quark masses, partly through the running of the fine structure constant, is well known in the standard model. We consider the suggestion that the quark mass matrix eigenvalue runs in the same way, i.e.,

$$m_U(\mu) = m_t(\mu), \tag{6.1}$$

$$m_D(\mu) = m_b(\mu). \tag{6.2}$$

6.1 Evolution of the Metric with Scale

6.1.1 From Framons to the Metric

We can find the metric on $\widetilde{su}(3)$ space by considering the configuration of the strong framon fields in a vacuum of the theory. The form of the framon vacuum depends on the gauge chosen. An $\widetilde{su}(3)$ gauge can always be chosen so that at a particular scale $\boldsymbol{\alpha}$ points in a given direction. Here we will choose the gauge such that $\boldsymbol{\alpha} = (1, 0, 0)$ at $\mu = \infty$. The RGE equations then tell us how the vacuum, parameterised by $\boldsymbol{\alpha}$, changes with scale, whilst remaining in the same gauge. We can fix the $su(3)$ gauge so that the situation is equivalent to $(T_0, \boldsymbol{\alpha}_0, \boldsymbol{\alpha}_0)$ set up, where the framon vacuum is

$$\Phi = \frac{\zeta_S}{\sqrt{3}} \begin{pmatrix} \sqrt{1+2R} & 0 & 0 \\ 0 & \sqrt{1-R} & 0 \\ 0 & 0 & \sqrt{1-R} \end{pmatrix}, \tag{6.3}$$

where the columns of the matrix are the frame vectors $\hat{\phi}^{\tilde{a}}$ normalised so that

$$\sum_{\tilde{a}} |\hat{\phi}^{\tilde{a}}|^2 = 3. \tag{6.4}$$

The metric is then given by

$$g^{\tilde{a}\tilde{b}} = \sum_a (\hat{\phi}^{\tilde{a}}_a)^* \hat{\phi}^{\tilde{b}}_a, \tag{6.5}$$

or

$$\tilde{g} = g^{\tilde{a}\tilde{b}} = \begin{pmatrix} 1+2R & 0 & 0 \\ 0 & 1-R & 0 \\ 0 & 0 & 1-R \end{pmatrix}, \tag{6.6}$$

$$g = g_{\tilde{a}\tilde{b}} = \begin{pmatrix} \frac{1}{1+2R} & 0 & 0 \\ 0 & \frac{1}{1-R} & 0 \\ 0 & 0 & \frac{1}{1-R} \end{pmatrix}, \tag{6.7}$$

which tends to the identity matrix as $R \to 0$.

We can then use this metric to find how vectors in $\widetilde{su}(3)$ space parallel transport as scale changes. We will need to know this to be able to define the inner product. Here we work out explicitly, by calculating the Christoffel symbols, the parallel transport matrix. To do this we extend the space by adding an extra dimension for scale. We use superscripts to denote vector components, $\boldsymbol{\alpha} = (0, \alpha^1, \alpha^2, \alpha^3)$, and subscripts to denote scale, $\boldsymbol{\alpha}_1 = \boldsymbol{\alpha}(\mu = \mu_1)$.

Taking coordinates (t, x, y, z) indexed by $(0, 1, 2, 3)$ with Greek indices, we start with the metric

$$g = \begin{pmatrix} 1 & 0 & 0 & 0 \\ 0 & \frac{1}{1+2R} & 0 & 0 \\ 0 & 0 & \frac{1}{1-R} & 0 \\ 0 & 0 & 0 & \frac{1}{1-R} \end{pmatrix}. \tag{6.8}$$

If we take the normal Levi-Civita connection then the Christoffel symbols are given by

$$\Gamma^c_{ab} = \frac{1}{2} g^{cd}(\partial_a g_{db} + \partial_b g_{ad} - \partial_d g_{ab}). \tag{6.9}$$

From this we find the non-zero Christoffel symbols,

$$\begin{aligned} \Gamma^0_{11} &= -\frac{1}{2}\frac{\partial}{\partial t}\left(\frac{1}{1+2R}\right), & (6.10)\\ \Gamma^0_{22} = \Gamma^0_{33} &= -\frac{1}{2}\frac{\partial}{\partial t}\left(\frac{1}{1-R}\right), & (6.11)\\ \Gamma^1_{10} = \Gamma^1_{01} &= \frac{1}{2}(1+2R)\frac{\partial}{\partial t}\left(\frac{1}{1+2R}\right), & (6.12)\\ \Gamma^2_{20} = \Gamma^2_{02} = \Gamma^3_{30} = \Gamma^3_{03} &= \frac{1}{2}(1-R)\frac{\partial}{\partial t}\left(\frac{1}{1-R}\right). & (6.13) \end{aligned}$$

We have the covariant derivative of a vector $\boldsymbol{\alpha}$ in the t direction given by

$$\nabla_t \boldsymbol{\alpha} = \left(\frac{\partial \alpha^\mu}{\partial t} + \alpha^\nu \Gamma^\mu_{0\nu}\right) e_\mu. \tag{6.14}$$

If we now consider just the x component of this we find, using $\Gamma^\mu_{0\nu} = 0$ for $\mu \neq \nu$,

$$(\nabla_t \boldsymbol{\alpha})^1 = \frac{\partial \alpha^1}{\partial t} + \alpha^1 \Gamma^1_{01}. \tag{6.15}$$

Parallel transport means that $(\nabla_t \boldsymbol{\alpha})^1 = 0$ so

$$\frac{\partial \alpha^1}{\partial t} = -\frac{1}{2}(1+2R)\frac{\partial}{\partial t}\left(\frac{1}{1+2R}\right)\alpha^1. \tag{6.16}$$

Now we know that $\frac{d}{dx}(\ln x) = \frac{1}{x}$, so that $\frac{d}{dt}(\ln x) = \frac{1}{x}\frac{dx}{dt}$ and taking $x = \frac{1}{1+2R}$ we find

$$\begin{aligned} \frac{\partial}{\partial t}\left(\ln\left(\frac{1}{1+2R}\right)\right) &= (1+2R)\frac{\partial}{\partial t}\left(\frac{1}{1+2R}\right), & (6.17)\\ \frac{\partial}{\partial t}\left(\ln\left(\frac{1}{1+2R}\right)^{-\frac{1}{2}}\right) &= -\frac{1}{2}(1+2R)\frac{\partial}{\partial t}\left(\frac{1}{1+2R}\right). & (6.18) \end{aligned}$$

Since $\boldsymbol{\alpha}$ and R only depend on t the partial derivatives are in fact total derivatives and we can now easily integrate

$$\int_{t_1}^{t_2} \frac{d}{dt}\left(\ln \alpha^1\right) dt = \int_{t_1}^{t_2} \frac{d}{dt}(\ln(1+2R)^{\frac{1}{2}})dt, \tag{6.19}$$

$$\ln\left(\frac{\alpha_2^1}{\alpha_1^1}\right) = \ln\left(\frac{1+2R_2}{1+2R_1}\right)^{\frac{1}{2}}, \tag{6.20}$$

$$\left(\frac{\alpha_2^1}{\alpha_1^1}\right) = \left(\frac{1+2R_2}{1+2R_1}\right)^{\frac{1}{2}}. \tag{6.21}$$

Similarly if we consider the y and z components of the covariant derivative we find

$$\frac{\partial \alpha^2}{\partial t} = -\frac{1}{2}(1-R)\frac{\partial}{\partial t}\left(\frac{1}{1-R}\right)\alpha^2, \tag{6.22}$$

$$\frac{\partial \alpha^3}{\partial t} = -\frac{1}{2}(1-R)\frac{\partial}{\partial t}\left(\frac{1}{1-R}\right)\alpha^3, \tag{6.23}$$

which we can integrate to give

$$\left(\frac{\alpha_2^2}{\alpha_1^2}\right) = \left(\frac{\alpha_2^3}{\alpha_1^3}\right) = \left(\frac{1-R_2}{1-R_1}\right)^{\frac{1}{2}}. \tag{6.24}$$

We can now write parallel transport of the original 3-vector with scale as

$$\boldsymbol{\alpha}_2 = \begin{pmatrix} \frac{P_2}{P_1} & 0 & 0 \\ 0 & \frac{Q_2}{Q_1} & 0 \\ 0 & 0 & \frac{Q_2}{Q_1} \end{pmatrix} \boldsymbol{\alpha}_1, \tag{6.25}$$

with $P_i^2 = 1+2R_i$ and $Q_i^2 = 1-R_i$, for $i = 1, 2$.

6.2 Mass Leakage and the Strong CP Solution in the Presence of a Metric

With this parallel transport we can find the inner product and the cross product. Writing

$$\mathrm{PT}(\mu_1 \to \mu_2)\mathbf{v}(\mu_1) := \begin{pmatrix} \sqrt{\frac{1+2R(\mu_2)}{1+2R(\mu_1)}} & 0 & 0 \\ 0 & \sqrt{\frac{1-R(\mu_2)}{1-R(\mu_1)}} & 0 \\ 0 & 0 & \sqrt{\frac{1-R(\mu_2)}{1-R(\mu_1)}} \end{pmatrix} \mathbf{v}(\mu_1) = \mathbf{v}(\mu_2) \tag{6.26}$$

as the parallel transport of a vector $\mathbf{v}$ from μ_1 to μ_2 we can calculate the inner product and cross product with respect to this metric by noting that it is equal to the identity at $\mu = 0$. To find the inner product between two vectors we can simply parallel transport them both to $\mu = 0$ and then take the normal inner product,

$$\begin{aligned}
\mathrm{IP}[\mathbf{v}, \mathbf{w}; \mu] &= \big(\mathrm{PT}(\mu \to 0)\mathbf{v}(\mu)^\dagger\big) \cdot \big(\mathrm{PT}(\mu \to 0)\mathbf{w}(\mu)\big) \\
&= \begin{pmatrix} \frac{\mathrm{v}_1^*}{P} & \frac{\mathrm{v}_2^*}{Q} & \frac{\mathrm{v}_3^*}{Q} \end{pmatrix} \cdot \begin{pmatrix} \frac{\mathrm{w}_1}{P} \\ \frac{\mathrm{w}_2}{Q} \\ \frac{\mathrm{w}_3}{Q} \end{pmatrix} \\
&= \frac{\mathrm{v}_1^* \mathrm{w}_1}{P^2} + \frac{\mathrm{v}_2^* \mathrm{w}_2}{Q^2} + \frac{\mathrm{v}_3^* \mathrm{w}_3}{Q^2} \\
&= \mathbf{v}(\mu)^\dagger g(\mu) \mathbf{w}(\mu),
\end{aligned} \tag{6.27}$$

as expected. Although we've written an explicit dependence on the scale in the final line the inner product is independent of scale. The important thing is that all three quantities on the right hand side need to be at the same scale.

Similarly, we can find the cross product by parallel transporting the vectors to $\mu = 0$, performing a normal cross product, and returning the resulting vector to the original scale,

$$\begin{aligned}
\mathrm{CP}[\mathbf{v}, \mathbf{w}; \mu] &= \mathrm{PT}(0 \to \mu)\Big[\Big(\mathrm{PT}(\mu \to 0)\mathbf{v}(\mu)\Big) \times \Big(\mathrm{PT}(\mu \to 0)\mathbf{w}(\mu)\Big)\Big] \\
&= \begin{pmatrix} P & 0 & 0 \\ 0 & Q & 0 \\ 0 & 0 & Q \end{pmatrix} \left[\begin{pmatrix} \frac{\mathrm{v}_1}{P} \\ \frac{\mathrm{v}_2}{Q} \\ \frac{\mathrm{v}_3}{Q} \end{pmatrix} \times \begin{pmatrix} \frac{\mathrm{w}_1}{P} \\ \frac{\mathrm{w}_2}{Q} \\ \frac{\mathrm{w}_3}{Q} \end{pmatrix} \right] \\
&= \begin{pmatrix} P & 0 & 0 \\ 0 & Q & 0 \\ 0 & 0 & Q \end{pmatrix} \begin{pmatrix} \frac{\mathrm{v}_2 \mathrm{w}_3}{Q^2} - \frac{\mathrm{v}_3 \mathrm{w}_2}{Q^2} \\ \frac{\mathrm{v}_3 \mathrm{w}_1}{PQ} - \frac{\mathrm{v}_1 \mathrm{w}_3}{PQ} \\ \frac{\mathrm{v}_1 \mathrm{w}_2}{PQ} - \frac{\mathrm{v}_2 \mathrm{w}_1}{PQ} \end{pmatrix} \\
&= \begin{pmatrix} \frac{P}{Q^2}(\mathrm{v}_2 \mathrm{w}_3 - \mathrm{v}_3 \mathrm{w}_2) \\ \frac{1}{P}(\mathrm{v}_3 \mathrm{w}_1 - \mathrm{v}_1 \mathrm{w}_3) \\ \frac{1}{P}(\mathrm{v}_1 \mathrm{w}_2 - \mathrm{v}_2 \mathrm{w}_1) \end{pmatrix} \\
&= \sqrt{1+2R} \begin{pmatrix} \frac{(\mathrm{v}_2 \mathrm{w}_3 - \mathrm{v}_3 \mathrm{w}_2)}{1-R} \\ \frac{(\mathrm{v}_3 \mathrm{w}_1 - \mathrm{v}_1 \mathrm{w}_3)}{1+2R} \\ \frac{(\mathrm{v}_1 \mathrm{w}_2 - \mathrm{v}_2 \mathrm{w}_1)}{1+2R} \end{pmatrix},
\end{aligned} \tag{6.28}$$

where the result now depends on scale and everything on the right is taken at scale μ.

Now we know the inner product and cross product with respect to the metric we can modify the mass leakage mechanism to take account of the non-trivial metric. We will illustrate the process by finding the $(\mathbf{v}_u, \mathbf{v}_c, \mathbf{v}_t)$ triad. With respect to the new metric $\boldsymbol{\alpha}$ is no longer normalised. We will use $\boldsymbol{\alpha}$, which obeys the RGE, to construct a new vector,

$$\widehat{\boldsymbol{\alpha}}(\mu) = \frac{\boldsymbol{\alpha}(\mu)}{\sqrt{\mathrm{IP}[\boldsymbol{\alpha}(\mu), \boldsymbol{\alpha}(\mu); \mu]}}. \tag{6.29}$$

The position of the top quark state vector is then given by the position of $\widehat{\boldsymbol{\alpha}}(\mu = m_t)$. We can find the position of the top quark state vector at any scale by parallel transporting to a new scale,

$$\mathbf{v}_t(\mu) = \mathrm{PT}(m_t \to \mu)\widehat{\boldsymbol{\alpha}}(m_t). \tag{6.30}$$

Note that parallel transport preserves the norm under the metric, so $\mathbf{v}_t(\mu)$ will have unit length with respect to the metric at all scales.

We then consider the situation at a scale equal to the mass of the charm quark. Previously we projected onto the subspace orthogonal to $\boldsymbol{\alpha}(m_c)$. Here we find it more convenient, rather than performing this projection, to proceed using the cross product, though the end result is equivalent. At the scale of the charm quark we can define the up quark state vector as we know it must be orthogonal to both $\widehat{\boldsymbol{\alpha}}(m_c)$, as prescribed by the mass leakage mechanism, and $\mathbf{v}_t(m_c)$, so the CKM matrix is unitary. The up quark state vector is then

$$\mathbf{v}_u(\mu) = \mathrm{PT}(m_c \to \mu)\mathrm{CP}[\widehat{\boldsymbol{\alpha}}(m_c), \mathbf{v}_t(m_c); m_c]. \tag{6.31}$$

Similarly we know that $\mathbf{v}_c(\mu)$ must be orthogonal, with respect to the metric, to $\mathbf{v}_u(\mu)$ and $\mathbf{v}_t(\mu)$ at $\mu = m_c$ so that

$$\mathbf{v}_c(\mu) = \mathrm{PT}(m_c \to \mu)\mathrm{CP}[\mathbf{v}_t(m_c), \mathbf{v}_u(m_c); m_c], \tag{6.32}$$

giving a right handed triad. The down-type and charged lepton state vector triads are similarly defined.

As in the first part of this thesis we will want to effect chiral transformations on the state vectors. As in the first section we will, from this point, take state vectors to mean those for left handed fields, so we can again make the substitution

$$e^{i\gamma_5\theta_f} \to e^{i\theta_f}. \tag{6.33}$$

When we go on to discuss Higgs decay we must again bear this in mind.

To effect the chiral transformation on quark fields which remain massless under infinitesimal changes in scale we need to find the modified Darboux triad. By modified we mean a Darboux triad with respect to the metric in $\widetilde{su}(3)$ space. We will find it using the new, normalised vector $\widehat{\boldsymbol{\alpha}}(\mu)$. The normal is again given by $\widehat{\boldsymbol{\alpha}}$. Next we use the cross product with respect to the metric to find the new $\widehat{\boldsymbol{\nu}}(\mu)$, which must be orthogonal, with respect to the metric, to the normal and the derivative of $\widehat{\boldsymbol{\alpha}}(\mu)$ with respect to scale, $\dot{\widehat{\boldsymbol{\alpha}}}(\mu)$:

$$\widehat{\boldsymbol{\nu}}(\mu) = \mathrm{CP}[\dot{\widehat{\boldsymbol{\alpha}}}(\mu), \widehat{\boldsymbol{\alpha}}(\mu); \mu]. \tag{6.34}$$

The new tangent is then given by

$$\widehat{\boldsymbol{\tau}}(\mu) = \mathrm{CP}[\widehat{\boldsymbol{\alpha}}(\mu), \widehat{\boldsymbol{\nu}}(\mu); \mu]. \tag{6.35}$$

As before we want to effect the chiral transformation on a state vectors in the $\widehat{\boldsymbol{\nu}}(\mu)$ direction. Rather than use rotation matrices, as we did previously, to effect the chiral transformation we here find it more convenient, due to the added complication of the metric, to decompose the state vectors along the components of the modified Darboux triad. We will now write the state vector as a function of the angle, θ_{CP},

$$\begin{aligned}\mathbf{v}_i(\mu;\theta_{CP}) = &\ \mathrm{IP}[\mathbf{v}_i(\mu), \widehat{\boldsymbol{\alpha}}(\mu), \mu]\widehat{\boldsymbol{\alpha}}(\mu) \\ &+ \mathrm{IP}[\mathbf{v}_i(\mu), \widehat{\boldsymbol{\tau}}(\mu), \mu]\widehat{\boldsymbol{\tau}}(\mu) \\ &+ \mathrm{IP}[\mathbf{v}_i(\mu), \widehat{\boldsymbol{\nu}}(\mu), \mu]\widehat{\boldsymbol{\nu}}(\mu)e^{-i\theta_{CP}/2},\end{aligned} \tag{6.36}$$

for $i \in (t, c, u; b, s, d)$.

The CKM matrix is given by the inner products of state vectors, as usual,

$$V_{ud}(\theta_{CP}) = \mathrm{IP}[\mathbf{v}_u(\mu;\theta_{CP}), (\mathbf{v}_d(\mu);\theta_{CP})^*, \mu], \tag{6.37}$$

and similarly for the other elements of V, where the complex conjugate of $\mathbf{v}_d(\mu;\theta_{CP})$ is taken since the state vectors are now in general complex. This process relates θ_{CP} and the Jarlskog invariant,

$$J = a\sin\left(\frac{\theta_{CP}}{2}\right) + b\sin(\theta_{CP}), \tag{6.38}$$

where $a, b \in \mathbb{R}$ depend on the trajectory. As long as either a or b is sufficiently large the experimental value of J can be used to fit θ_{CP}.

The mass matrix is now given by

$$m = m_T \widehat{\boldsymbol{\alpha}}(\mu)^\dagger \widehat{\boldsymbol{\alpha}}(\mu). \tag{6.39}$$

We have, for the top quark,

$$\begin{aligned} m_t &= m_U \mathrm{IP}[\widehat{\boldsymbol{\alpha}}(m_t), \widehat{\boldsymbol{\alpha}}(m_t); m_t] \\ &= m_U, \end{aligned} \tag{6.40}$$

as expected. The mass of the charm quark is given by

$$m_c = m_U \mathrm{IP}[\mathbf{v}_c(m_c), \widehat{\boldsymbol{\alpha}}(m_c); m_c]^2 \tag{6.41}$$

and similarly for the up quark.

There is an extra complication in that the experimental values of the light quarks are given at $\mu = 2$ GeV rather than at their mass. The mass leakage mechanism tells us that we should take

$$m_u(2\text{ GeV}) = m_U \mathrm{IP}[\mathbf{v}_u(2\text{ GeV}), \widehat{\boldsymbol{\alpha}}(2\text{ GeV}); 2\text{ GeV}]^2, \tag{6.42}$$

$$m_d(2\text{ GeV}) = m_D \mathrm{IP}[\mathbf{v}_d(2\text{ GeV}), \widehat{\boldsymbol{\alpha}}(2\text{ GeV}); 2\text{ GeV}]^2, \tag{6.43}$$

$$m_s(2\text{ GeV}) = m_D \mathrm{IP}[\mathbf{v}_s(2\text{ GeV}), \widehat{\boldsymbol{\alpha}}(2\text{ GeV}); 2\text{ GeV}]^2. \tag{6.44}$$

It is, however, difficult to compare these values with the experimental values due to complications of the strong force at low scales.

6.3 Running of the Quark Masses

There has been a suggestion [29] that the eigenvalues of the mass matrix may run with scale, due to the inclusion of gluon loops, in a way analogous to quarks in the standard model. We will investigate the feasibility of this by studying the effect of introducing this QCD running. In this section we discuss the QCD running of the top and bottom quarks in the standard model and the application of this to the FSM eigenvalues.

The 4-loop expansions for the running $\overline{\mathrm{MS}}$ quark masses are given in [31]:

$$m_t(\mu^2) = \hat{m}_t \left(\frac{\alpha_s(\mu^2)}{\pi}\right)^{4/7} \left[1 + 1.39796 \left(\frac{\alpha_s(\mu^2)}{\pi}\right) + 1.79348 \left(\frac{\alpha_s(\mu^2)}{\pi}\right)^2 + \right.$$
$$\left. - 0.683433 \left(\frac{\alpha_s(\mu^2)}{\pi}\right)^3\right], \tag{6.45}$$

$$m_b(\mu^2) = \hat{m}_b \left(\frac{\alpha_s(\mu^2)}{\pi}\right)^{12/23} \left[1 + 1.17549 \left(\frac{\alpha_s(\mu^2)}{\pi}\right) + 1.50071 \left(\frac{\alpha_s(\mu^2)}{\pi}\right)^2 + \right.$$
$$\left. + 0.172478 \left(\frac{\alpha_s(\mu^2)}{\pi}\right)^3\right], \tag{6.46}$$

where $\hat{m}_{t,b}$ are set by experimental measurements of the running masses. The scale dependence is a function only of the running of the strong coupling constant, α_s. Recent experimental results (2009) and a 4-loop expansion of α_s is given in [6], and we will outline their results here. They use the 4-loop expansion of α_s given in [30]:

$$\mu^2 \frac{\partial \alpha_s(\mu^2)}{\partial \mu^2} = -\beta_0 \alpha_s^2(\mu^2) - \beta_1 \alpha_s^3(\mu^2) - \beta_2 \alpha_s^4(\mu^2) - \beta_3 \alpha_s^5(\mu^2) + O(\alpha_s^6) \tag{6.47}$$

with

$$\beta_0 = \frac{33 - 2N_f}{12\pi}, \tag{6.48}$$
$$\beta_1 = \frac{153 - 19N_f}{24\pi^2}, \tag{6.49}$$
$$\beta_2 = \frac{77139 - 15099N_f + 325N_f^2}{3456\pi^3}, \tag{6.50}$$
$$\beta_3 \approx \frac{29243 - 6946.3N_f + 406.089N_f^2 + 1.49931N_f^3}{256\pi^4}, \tag{6.51}$$

where N_f is the number of active quark flavours at the scale μ. Given the value of α_s at a given energy (an experimentally convenient scale is the Z^0 boson mass, $\mu = m_{Z^0}$) we can then run to another scale. It is becoming increasingly common to parameterise $\alpha_s(\mu^2)$ with a dimensionful parameter, Λ, which denotes the scale at which α_s becomes infinite, i.e.,

$$\Lambda^2 = \frac{\mu^2}{e^{1/(\beta_0 \alpha_s(\mu^2))}}, \tag{6.52}$$

rather than to specify $\alpha_s(\mu^2)$ at a given energy. The only complication comes at quark thresholds. We know that since α_s is a physical quantity it must be continuous

when crossing quark thresholds (ignoring its uncontrolled behaviour below 1 GeV). Since the running depends on the number of active quark flavours Λ must change when crossing a quark threshold. We use a 3-loop matching condition where $\alpha_s(\mu^2)$ and its derivative are matched across a quark threshold, which we take to be the pole mass (we could use the running mass; in the case of 3-loop matching the difference is negligible). To indicate this we will relabel Λ as $\Lambda_{\overline{MS}}^{(N_f)}$. The matching condition [15] is

$$\alpha_s^{(N_f-1)} = \alpha_s^{(N_f)} + c_2\frac{\left(\alpha_s^{(N_f)}\right)^2}{\pi} + c_3\frac{\left(\alpha_s^{(N_f)}\right)^3}{\pi^2}, \tag{6.53}$$

where

$$c_2 = -\frac{7}{24}, \tag{6.54}$$

$$c_3 = -\frac{80507}{27648}\zeta(3) - \frac{2}{3}\zeta(2)\left(\frac{1}{3}\ln 2 + 1\right) - \frac{58933}{124416} + \frac{(N_f-1)}{9}\left(\zeta(2) + \frac{2479}{3456}\right), \tag{6.55}$$

and ζ is Riemann's zeta function.

We found $\Lambda_{\overline{MS}}^{(N_f=5)} = 212.2$ MeV for $m_{Z^0} = 91.1876$ GeV [24]. The matching conditions then give different Λ's in regions where different numbers of quarks are active. We found $\Lambda_{\overline{MS}}^{(N_f=4)} = 299.2$ MeV and $\Lambda_{\overline{MS}}^{(N_f=3)} = 339.0$ MeV for pole masses $m_c = 1.5$ GeV and $m_b = 4.7$ GeV. There is good agreement between these values and those quoted in [6]. Since we are interested in high energy behaviour we also found $\Lambda_{\overline{MS}}^{(N_f=6)} = 90.8$ MeV for $m_t = 171.3$ GeV. The running of $\alpha_s(\mu^2)$ is shown in figure 6.1.

We then, through the 4-loop running mass expansions (equations (6.45) and (6.46)), found the QCD running behaviour of $m_t(\mu^2)$ and $m_b(\mu^2)$, figure 6.2. We can now ask what effect QCD running will have on the masses of the fermions obtained through the mass leakage scheme. Previously the mass leakage scheme gave

$$m_U = m_t, \tag{6.56}$$

$$m_D = m_b, \tag{6.57}$$

for the mass matrix eigenvalues. Now there is QCD running we simply have

$$m_U(\mu) = m_t(\mu), \tag{6.58}$$

$$m_D(\mu) = m_b(\mu). \tag{6.59}$$

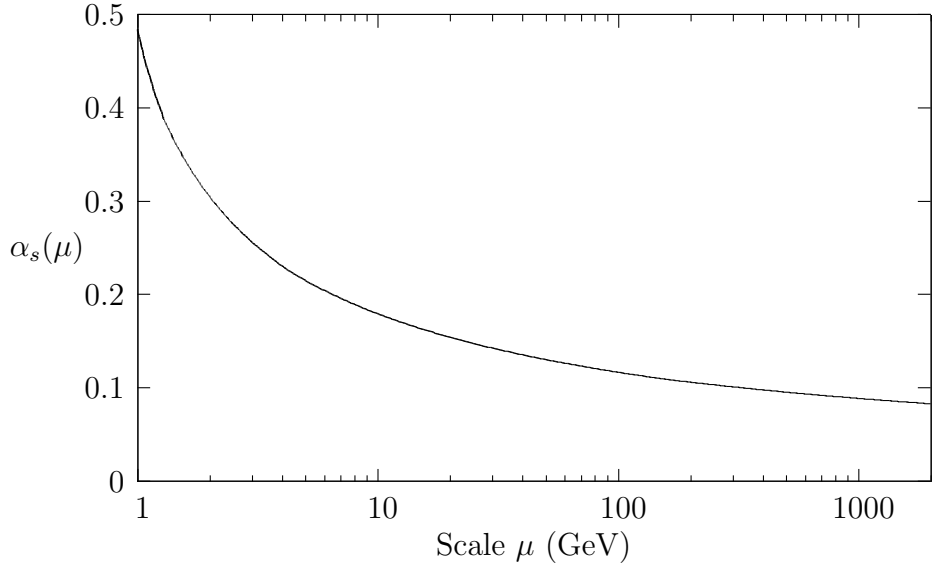

Figure 6.1: The running of $\alpha_s(\mu)$.

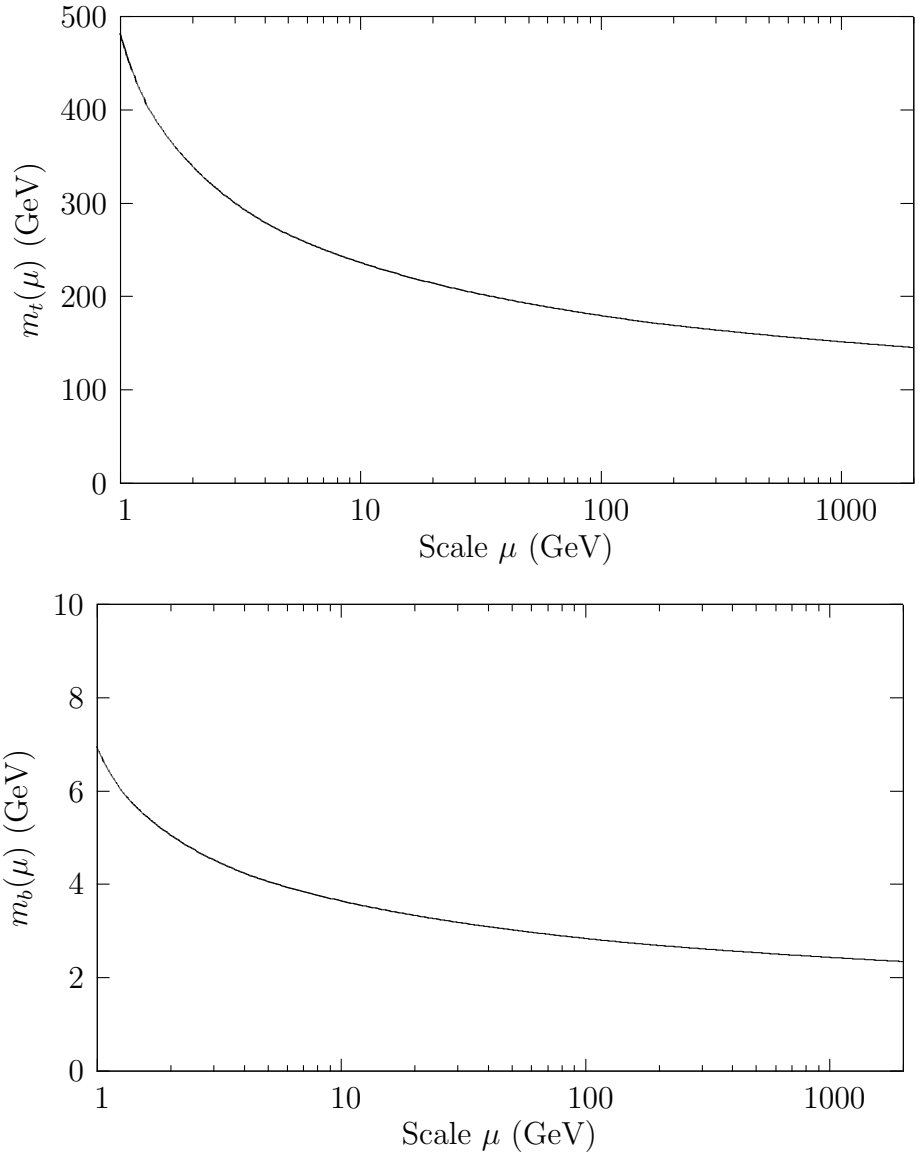

Figure 6.2: The running of m_t and m_b.

Chapter 7

Comparing the FSM to Data

Matching the FSM trajectory to data can be done with the lattice scan and simplex optimisation techniques used in the first part, though now the process is simpler as we know the underlying trajectory of $\boldsymbol{\alpha}$. We can use it directly to find values to compare with the experimental values. We again have a parameter space, this time the space of the integration constants coming from the RGE and one parameter resulting from the coupling constants of the theory. Here again we chose to use a lattice scan to give us a view over the whole parameter space followed by simplex optimisation to improve the resolution in the most promising areas of parameter space. Since we don't need to match experimental outputs with a measure of 'smoothness' we can be more rigorous in defining the measure used on the parameter space. Since the strange quark scale must be used to find the CKM matrix, and it is poorly determined by experiment, we also allow the strange quark mass to range over quite a large set of values, so this parameter becomes an extra dimension in our parameter space. Since we have the trajectory of $\boldsymbol{\alpha}$ we can go slightly further than in the first part and estimate $|U_{\mu 3}|$.

As inputs, to yield estimates from each trajectory, we use the initial values of θ, ϕ and R and the values of $\frac{\rho_S^2}{16\pi^2}$, m_t, m_b, m_τ, m_s and J. From these inputs we obtain estimates for m_t, m_c, m_u; m_b, m_s, m_d; m_τ, m_μ, m_e; 3 CKM mixing angles, J, θ_{CP} and $|U_{\mu 3}|$. This scheme replaces 15 independent variables in the standard model with 9.

7.1 Fitting the FSM to Data

We now have a 5 dimensional parameter space to investigate. Here the variables are $\theta_0 = \theta(\mu = \mu_0), \phi_0 = \phi(\mu = \mu_0), R_0 = R(\mu = \mu_0), c = \frac{\rho_S^2}{16\pi^2}$ and m_s. We took $\mu_0 = 250$ GeV. Although the choice is arbitrary we will mostly be interested in the trajectory around the heavy quarks. There are some conditions we can place on the

values that the variables may take: $0 \leq R_0 \leq 1$, $0 \leq \theta_0, \phi_0 \leq \pi/2$, $c \geq 0$ and $0.03 \text{ GeV} \leq m_s \leq 0.4 \text{ GeV}$.

Recall that $R = \nu_2 \zeta_W^2 / 2\kappa_S \zeta_S^2$. In the framon potential, equation (5.22), there was no condition on the sign of ν_2, so R can take either sign. We performed some preliminary studies and found that a positive R was better able to match experimental data, so we enforce $R_0 \geq 0$. We do not consider $R_0 \geq 1$, since the vacuum solution has terms containing factors of $\sqrt{1-R}$.

Naturally we must have $0 \leq \theta_0, \phi_0 \leq 2\pi$. However, the RGEs exhibit symmetry, up to sign, under both $\theta \to \pi - \theta$ and $\phi \to \pi - \phi$. The RGEs are also symmetric, up to sign, around $\theta, \phi = \pi/2$. The effect of the signs is only to change the handedness of the resulting trajectories which has no effect for us as we are free to choose the handedness of our resulting triads so that they are always right handed. This means that we can look at all distinct trajectories by considering only $0 \leq \theta_0, \phi_0 \leq \pi/2$. It is clear that $c = \frac{\rho_S^2}{16\pi^2}$ must be positive. We choose $0.03 \text{ GeV} \leq m_s \leq 0.4 \text{ GeV}$ which is the largest range which seems plausible given the experimental data.

For the lattice scan we chose values evenly across this range of parameters. For the simplex optimisation, however, we must ensure that the simplex does not walk out of these bounds. To achieve this we transformed our parameter space with the following functions:

$$f_R(R) = \operatorname{arctanh}(2R - 1), \tag{7.1}$$

$$f_\theta(\theta) = \operatorname{arctanh}\left(\frac{4\theta}{\pi} - 1\right), \tag{7.2}$$

$$f_\phi(\phi) = \operatorname{arctanh}\left(\frac{4\phi}{\pi} - 1\right), \tag{7.3}$$

$$f_c(c) = \ln(c), \tag{7.4}$$

$$f_{m_s}(m_s) = \operatorname{arctanh}\left(\frac{2(m_s - 0.03)}{0.4 - 0.03} - 1\right). \tag{7.5}$$

Using these functions we can walk around freely in the new parameter space and the simplex optimisation will not go outside the bounds that we have set. We chose equal size steps in the new parameter space, meaning that the steps will not be of equal size in each direction in the original parameter space. The size of the steps in the original parameter space will depend on how close to the boundary of the region we are. This is very useful, since the results from the trajectory have a greater dependence on the initial parameters when they are near a boundary, e.g., the difference in results in starting from $R_0 = 0.99$ and 0.999 is much greater than the difference in starting

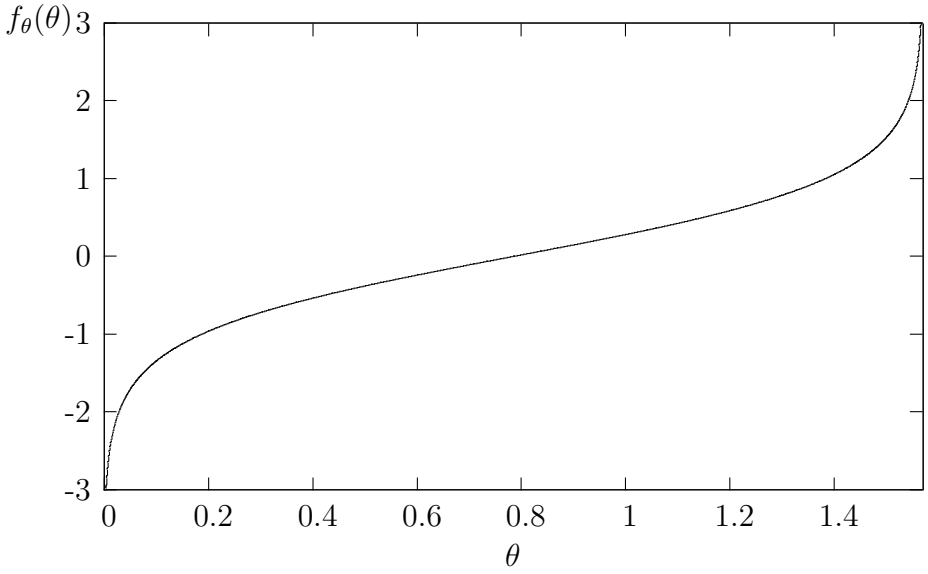

Figure 7.1: A plot showing $f_\theta(\theta)$.

from $R_0 = 0.49$ and 0.499. We did not investigate the precise correlation but the behaviour of the arctanh can be seen qualitatively to be very useful for our purposes.

Again we will use a measure on the parameter space to allow us to automate the search. The fact that we will compare all the results to experimentally measured quantities, and will not be interested in attributes such as 'smoothness', allows us to be more rigorous in choosing our weighting functions. We used the measure

$$W = \sum_i W_i = \sum_i N_i \frac{(x_i - x_{i,\mathrm{Exp}})^2}{(x_i + x_{i,\mathrm{Exp}})^2}, \tag{7.6}$$

where x_i is a value estimated from the trajectory and $x_{i,\mathrm{Exp}}$ is the experimental value. Now all of the values are on an equal footing we can consider a 'distance' in our parameter space, so we square each term. We want to minimise this 'distance' so we will be searching for the point in parameter space with the smallest measure. We determined the weighting N_i partly through the experimental errors on quantities and partly using our judgment. We chose the N_i's so that $W_i = 1$ when x_i is 1σ away from the central value, i.e.,

$$N_i = \frac{(x_{i,\mathrm{Exp}} + (x_{i,\mathrm{Exp}} + \sigma_i))^2}{(x_{i,\mathrm{Exp}} - (x_{i,\mathrm{Exp}} + \sigma_i))^2}, \tag{7.7}$$

for most of our outputs. The charged lepton masses are measured very accurately. We do not expect the trajectory to capture all of the data perfectly so we introduce some flexibility. For the muon we chose to use $0.1 \times m_\mu$ instead of 1σ. Since the electron

	N_i
m_c	1070
m_μ	441
m_e	1.49
m_u	0
m_d	0
V_{us}	416000
V_{ub}	1970
V_{cb}	5710
$\lvert U_{\mu 3}\rvert$	1300

Table 7.1: The weighting factors, N_i, used for each quantity in our measure. A higher value of N_i gives a tighter constraint for that quantity.

is very light we do not expect the trajectory to reproduce it's mass very well so we chose $10 \times m_e$ instead of 1σ. We did not include m_u or m_d in the measure as their masses are poorly defined. The values of N_i used are shown in table 7.1. We only included 3 elements from the CKM matrix to reflect its 3 independent mixing angles. The other elements, when the phase has been fixed, are then fixed by unitarity.

In the first part we had to ignore the PMNS matrix and neutrino masses as the experimental data only weakly constrained the trajectory. Here, however, the trajectory of $\boldsymbol{\alpha}$ allows us to estimate $|U_{\mu 3}|$ as the angle between $\mathbf{v}_\mu$ and $\boldsymbol{\alpha}(\mu = 0.05 \text{ eV})$, where we have assumed $m_{\nu_3} = \sqrt{\Delta m^2_{23}}$.

Not all trajectories give sufficiently large values of either a or b in equation (6.38) to be able to match $J(\theta_{CP})$ to J_{Exp} for any θ_{CP}. We artificially gave points which don't return sufficiently large values for a or b a very large W.

This weighting function was designed to help us automate the search. Once we completed the automated search we spent some time investigating the best regions in parameter space by hand and we used our judgment to find what we considered to be the best matching.

In this part we used updated experimental data [24] which was released after the first part was completed.

7.2 Results

In this section we look at the results from the lattice scan and subsequent simplex optimisation. First we report the results when there is no QCD running. We go on to compare these results with the behaviour found in the first part of this thesis.

Then we look at the trajectory which best matches the experimental values when we include QCD running. We cannot compare this scenario to the first part of the thesis since there we did not include QCD running.

7.2.1 FSM Trajectory

The lattice scan, which looked at 360 000 points in parameter space, identified one region where the trajectories most closely matched the experimental data. We then did a simplex optimisation around the 10 points with the smallest measure for a variety of simplex sizes. Deciding which simplex size to take, and how many trajectories to consider, depended on judgment gained from experience. The simplex optimisation ran until the measure at all vertices of the simplex agreed to $\sim 1\%$, demonstrating that we were probing the parameter space at a sufficiently fine scale to see all of its features. One must bear in mind that many aspects of the measure were quite arbitrary so in judging one trajectory against another there is more to take into account than just the numerical value of the measure. We found, broadly, that we could change the trajectory to either have better fermion masses or a better CKM matrix. Table 7.2 shows a trajectory which we deemed to be among the best, but is perhaps on the side of having a better CKM matrix at the expense of the fermion masses.

The values for R_0, θ_0 and ϕ_0 are taken at 250 GeV. We can see that R_0 (0.993747), θ_0 (1.40098) and ϕ_0 (1.55169) are close to the values at the $F3_2$ fixed point, 1, $\pi/2$ and $\pi/2$ respectively. This is a general feature of all of the good trajectories that we found: $\boldsymbol{\alpha}(250\text{ GeV})$ is very close to the $F3_2$ fixed point. The constant $\rho_S^2/16\pi^2$, which can be thought of controlling the overall speed of rotation, has a value of 0.131487. The strange quark has a mass of 54 MeV, which is on the low side of the experimental range. The only effect of changing the strange mass is in changing the CKM matrix elements, but a light strange quark seemed to be favoured.

The masses and the CKM matrix can be seen to follow qualitatively the correct behaviour. There is a large hierarchy in masses between generations. The CKM matrix has very large components on the diagonal, with the sizes reducing towards the corners. The value of $|U_{\mu 3}|$ is in line with the experimental value, and fitting to the Jarlskog invariant gives a θ_{CP} of order unity.

We can, however, see that the agreement is not perfect. We have noted alongside the results an approximation of the error in each of the quantities. It must be stressed that this error is approximate and only intended as a guide to save the reader comparing the numbers by eye. This approximate error was calculated by taking the difference between the experimental value and the estimated value and dividing by

R_0	θ_0	ϕ_0	$\frac{\rho_S^2}{16\pi^2}$	m_s	$(m_{s\mathrm{Exp}})$
0.993747	1.40098	1.55169	0.131487	0.0542 GeV	$(101^{+29}_{-21}$ MeV)

	Experimental	FSM Trajectory	Approximate Error
m_c	$1.27^{+0.07}_{-0.09}$ GeV	1.12 GeV	1.7σ, 12%
m_u	$2.49^{+0.81}_{-0.79}$ MeV (2 GeV)	0.8 MeV (2 GeV)	2.1σ, 68%
m_d	$5.05^{+0.75}_{-0.95}$ MeV (2 GeV)	0.04 MeV (2 GeV)	-
m_μ	106 MeV	79 MeV	25%
m_e	0.511 MeV	5.6 MeV	1000%

	Absolute Values of the CKM elements
Experimental Values	$\begin{pmatrix} 0.97428 \pm 0.00015 & 0.2253 \pm 0.0007 & 0.00347^{+0.00016}_{-0.00012} \\ 0.2252 \pm 0.0007 & 0.97345^{+0.00015}_{-0.00016} & 0.0410^{+0.0011}_{-0.0007} \\ 0.00862^{+0.00026}_{-0.00020} & 0.0403^{+0.0011}_{-0.0007} & 0.999152^{+0.000030}_{-0.000045} \end{pmatrix}$
FSM Trajectory	$\begin{pmatrix} 0.97437 & 0.2249 & 0.00504 \\ 0.2245 & 0.97351 & 0.0432 \\ 0.01391 & 0.0412 & 0.999056 \end{pmatrix}$
Approximate Error	$\begin{pmatrix} 0.6\sigma,\ 0.009\% & 0.6\sigma,\ 0.1\% & 9.8\sigma,\ 45\% \\ 1\sigma,\ 0.3\% & 0.4\sigma,\ 0.006\% & 2\sigma,\ 5\% \\ 20\sigma,\ 61\% & 0.8\sigma,\ 2\% & 2.1\sigma,\ 0.01\% \end{pmatrix}$

	Experimental	FSM Trajectory
$\lvert U_{\mu_3}\rvert$	$0.5832 \leq \lvert U_{\mu 3}\rvert \leq 0.819$ at 99.73% C.L. (3σ)	0.82
θ_{CP}	Fitting J=2.91×10^{-5}	0.28

Table 7.2: The point in parameter space and the resulting estimates for the best trajectory with no QCD running. See text for notes.

the error in the experimental value (or by the experimental value itself for the percentage errors). Calculating the error this way does not take into account the fact that the masses cannot be negative so we cannot produce a sensible error for the down quark mass.

We see that the charm quark and the muon masses are reproduced quite well. The lightest quarks are not reproduced well, but as we have said there is much uncertainty in the definition of their mass. This scheme gives a down quark which is lighter than the up quark. Given that the top quark is around 40 times heavier than the bottom quark it seems that this scheme will have difficulty in reproducing an up quark which is lighter than the down quark. The electron is not well matched, although it disagrees by a factor of 10 which follows from our weighting. We would not expect the trajectory to reproduce the light fermion masses perfectly. Since the tightest experimental constraints come between $\mu = m_c$ and $\mu = m_t$ (i.e., from the heavy quark masses and the CKM matrix) this region of the curve can be thought to be strongly fixed by experiment, and so this region is best approximated by the one-loop RGE. As we move further from this region the contributions due to the higher order effects accumulate and our confidence in the trajectory reduces.

The absolute values in the CKM matrix match the experimental values very well. The top left 2×2 matrix has all of the values within the error bars. The far top right and bottom left components are the furthest from the experimental values, but much like the mass hierarchy these elements are expected to be changed the greatest amount by higher order corrections. The value of $|U_{\mu 3}|$ obtained is 3σ away from the experimental value. Whilst looking at neighbouring points in parameter space this was among the lowest values of $|U_{\mu 3}|$ seen.

Figure 7.2 shows the trajectory along with its stereographic projection. The box projected onto the sphere is the boundary box of the stereographic projection. The positions of $\boldsymbol{\alpha}$ at various particle masses is shown on the stereographic projection. The trajectory starts from the axis which corresponds to the $F3_2$ fixed point. The trajectory then moves towards the $\theta = 0$ axis, remaining very close to the $\phi = \pi/2$ plane. From the stereographic projection we can see that the bulk of the rotation occurs between the scale of the top quark and the electron.

Figure 7.3 shows the cumulative arc length of the trajectory. Again we can see that most of the rotation occurs between the mass of the top quark and the electron. In the next section we compare these results to those found in the top down approach in the first part of this thesis.

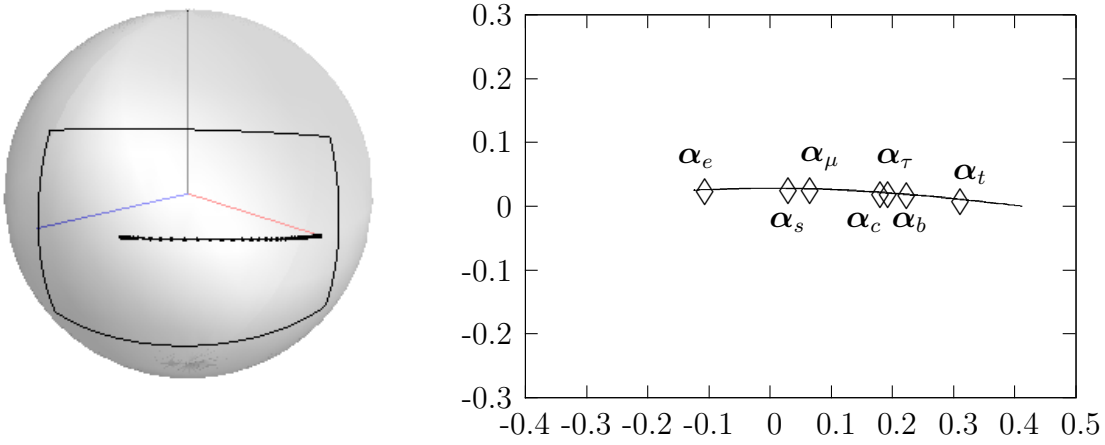

Figure 7.2: On the left (a), the trajectory with no QCD running, table 7.2. The axis on the right is the $F3_2$ fixed point while the axis on the left is at $\theta = 0$. On the right (b), a stereographic projection of the trajectory with diamonds to denote the position of $\boldsymbol{\alpha}$ at various scales. The bounding box has been projected onto the sphere in (a).

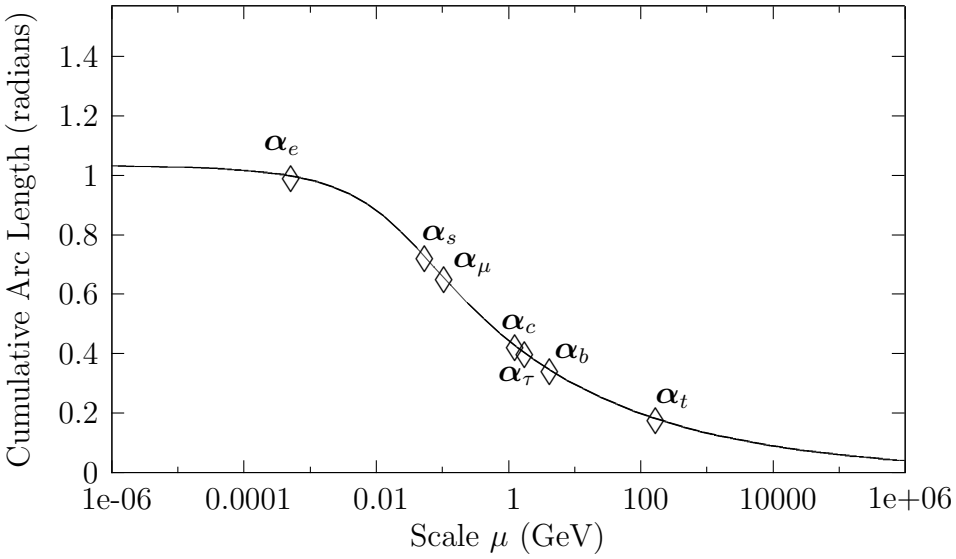

Figure 7.3: The cumulative arc length as the scale reduces from $\mu = \infty$ along the trajectory with no QCD running, table 7.2. Diamonds denote the cumulative arc length at various scales.

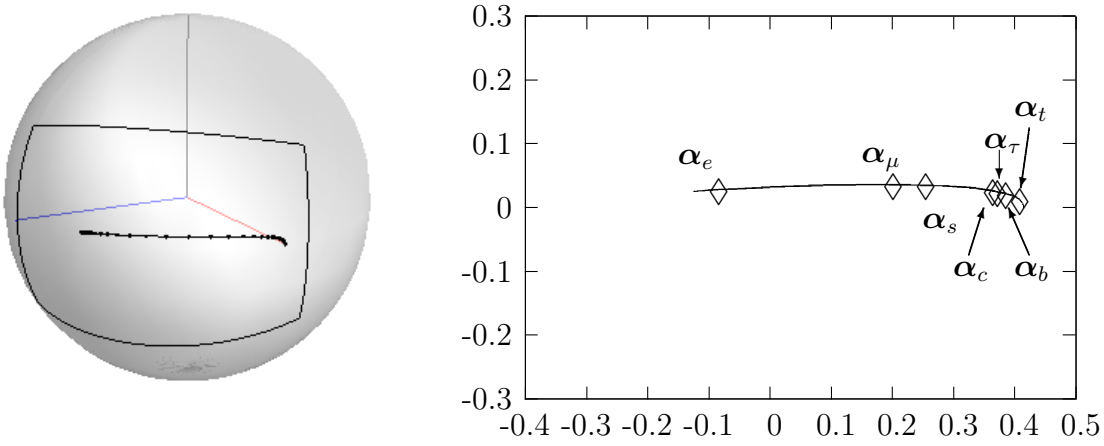

Figure 7.4: On the left (a), the effective trajectory corresponding to the trajectory with no QCD running, table 7.2. On the right (b), a stereographic projection of the effective trajectory with diamonds to denote the position of $\boldsymbol{\alpha}$ at various scales.

7.2.2 Comparing the FSM trajectory to the fit found in Part I

To compare these results with the general results found in the first part we have to take the metric, which did not figure in the first part, into account. We can do this by talking about the trajectory which would give the same results if the metric were not present, or an 'effective trajectory'. We can find the effective trajectory by parallel transporting the actual trajectory to $\mu = 0$,

$$\boldsymbol{\alpha}_{\text{EFF}}(\mu) = \text{PT}(\mu \to 0)\hat{\boldsymbol{\alpha}}(\mu). \tag{7.8}$$

The effective trajectory is shown in figure 7.4. We can see that there has been two major changes. Firstly the non-planarity of the trajectory is accentuated. We see that a knuckle has developed near the high energy fixed point. It is mostly this knuckle which gives rise to the form of the CKM matrix. The second effect has been to bunch the positions of $\boldsymbol{\alpha}(m_t)$, $\boldsymbol{\alpha}(m_b)$, $\boldsymbol{\alpha}(m_\tau)$ and $\boldsymbol{\alpha}(m_c)$ towards the high energy fixed point.

Figure 7.5 shows the effective trajectory along with the best fit curve from the first part of the thesis. The position of $\boldsymbol{\alpha}$ at various scales is also shown. To match the two curves the positions of $\boldsymbol{\alpha}(\mu = m_\tau)$ and the gradient of the curve at this point were matched. In the high energy region there is good agreement between the two trajectories. As the scale reduces from m_c to m_s the two curves diverge. For the trajectory found in this section the position of $\boldsymbol{\alpha}(m_s)$ is off of the plot. It was noted

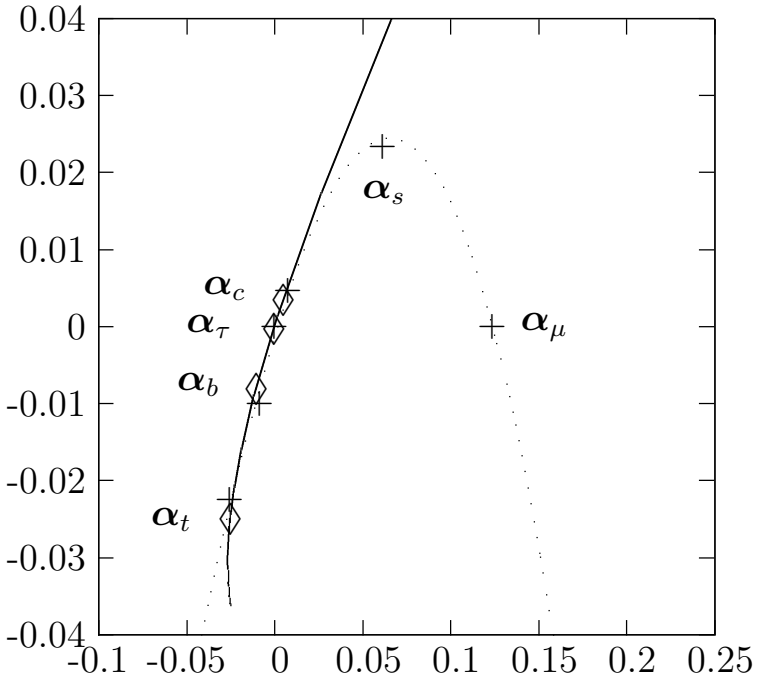

Figure 7.5: A stereographic projection of the effective trajectory corresponding to the trajectory with no QCD running, table 7.2 (solid line), along with the best fit curve found in part I (dotted line). The position of $\boldsymbol{\alpha}$ at various scales is given by diamonds for the effective trajectory and with crosses for the best fit trajectory. The positions of $\boldsymbol{\alpha}_s$ and $\boldsymbol{\alpha}_\mu$ for the effective trajectory are off of the plot.

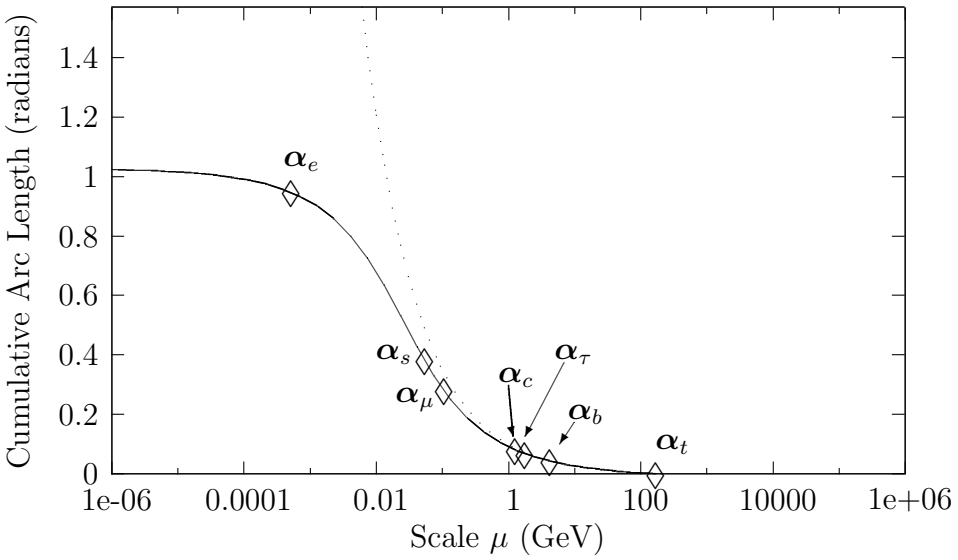

Figure 7.6: The cumulative arc length as the scale reduces from $\mu = \infty$ along the trajectory with no QCD running, table 7.2, (solid line) along with the cumulative arc length fit found in part I (dotted line). Diamonds denote the cumulative arc length at various scales for the effective trajectory.

in the first section that there is no physical constraint on the relationship between the quark and the lepton sectors. It is this matching that causes the curve from the top down approach to curve dramatically and go back to the bottom of the plot. This matching has no physical significance so is not an important disagreement. The large distance between the two positions of $\boldsymbol{\alpha}(m_s)$ is mostly due to the difference in the value of the mass taken, 105 MeV in the top down approach and 54 MeV here.

Figure 7.6 shows the cumulative arc length of the effective trajectory. We can see that the cumulative arc length from the top down approach closely matches the arc length here for all the fermions above 1 GeV. The agreement is good for the strange quark and the muon, but it should be remembered that in this effective trajectory the mass of the strange quark is quite different to the experimental masses used in the top down approach.

In the top down approach $\boldsymbol{\alpha}(m_e)$ occurred after around 0.35 radians, whereas here it is much closer to 1 radian. This is related to the fact that the matching between the quark and lepton sectors is quite different. This difference has no physical relevance. This is also because, as argued above, the RGE becomes less accurate as it moves away from the heavy quarks.

R_0	θ_0	ϕ_0	$\frac{\rho_S^2}{16\pi^2}$	m_s	$(m_{s\mathrm{Exp}})$
0.995965	1.21066	1.54293	0.0847614	0.0508349 GeV	$(101^{+29}_{-21}$ MeV)

	Experimental	FSM Trajectory	Approximate Error
m_c	$1.27^{+0.07}_{-0.09}$ GeV	2.17 GeV	13σ, 71%
m_u	$2.49^{+0.81}_{-0.79}$ MeV (2 GeV)	1.1 MeV (2 GeV)	2.2σ, 56%
m_d	$5.05^{+0.75}_{-0.95}$ MeV (2 GeV)	0.04 MeV (2 GeV)	-
m_μ	106 MeV	82 MeV	23%
m_e	0.511 MeV	6.9 MeV	1250%

	Absolute Values of the CKM elements
Experimental Values	$\begin{pmatrix} 0.97428 \pm 0.00015 & 0.2253 \pm 0.0007 & 0.00347^{+0.00016}_{-0.00012} \\ 0.2252 \pm 0.0007 & 0.97345^{+0.00015}_{-0.00016} & 0.0410^{+0.0011}_{-0.0007} \\ 0.00862^{+0.00026}_{-0.00020} & 0.0403^{+0.0011}_{-0.0007} & 0.999152^{+0.000030}_{-0.000045} \end{pmatrix}$
FSM Trajectory	$\begin{pmatrix} 0.97427 & 0.2254 & 0.00448 \\ 0.2251 & 0.97350 & 0.0405 \\ 0.01254 & 0.0388 & 0.999168 \end{pmatrix}$
Approximate Error	$\begin{pmatrix} 0.07\sigma,\ 0.001\% & 0.14\sigma,\ 0.04\% & 6.3\sigma,\ 26\% \\ 0.14\sigma,\ 0.04\% & 0.3\sigma,\ 0.005\% & 0.7\sigma,\ 1\% \\ 15\sigma,\ 45\% & 2.1\sigma,\ 4\% & 0.5\sigma,\ 0.002\% \end{pmatrix}$

	Experimental	FSM Trajectory
$\lvert U_{\mu_3}\rvert$	$0.5832 \leq \lvert U_{\mu 3}\rvert \leq 0.819$ at 99.73% C.L. (3σ)	0.97
θ_{CP}	Fitting J=2.91×10^{-5}	0.31

Table 7.3: The point in parameter space and the resulting estimates for the best trajectory with QCD running. See text for notes.

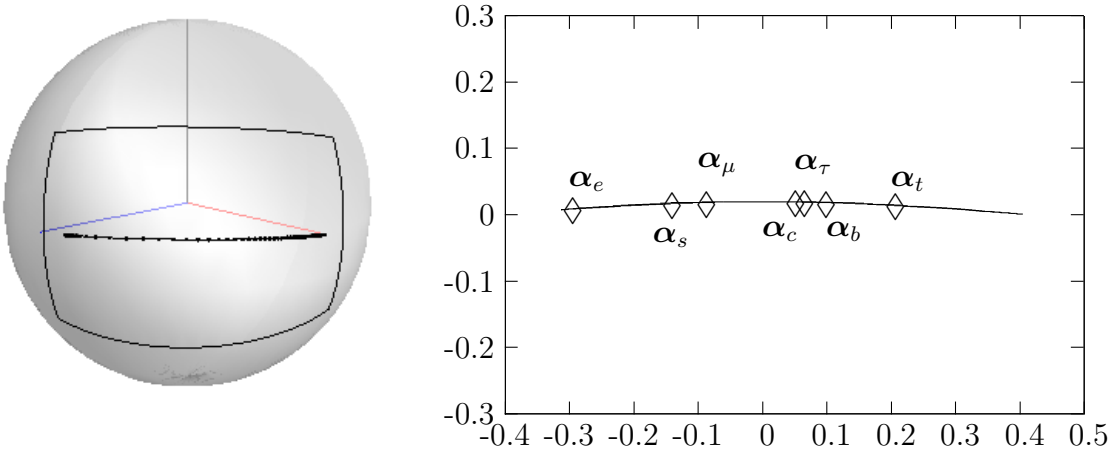

Figure 7.7: On the left (a), the trajectory with QCD running, table 7.3. On the right (b), a stereographic projection of the effective trajectory with diamonds to denote the position of $\boldsymbol{\alpha}$ at various scales.

7.2.3 FSM Trajectory with QCD running

We next introduced QCD running into the mass matrices' eigenvalues. Here we also performed a lattice scan over 360 000 points in parameter space. There was one region of parameter space which gave the most favourable results. We again performed simplex optimisation around the best points and used this combined with our judgment to find the most promising trajectory. Again there was a trade off between obtaining better masses or a better CKM matrix. For all of the trajectories which showed reasonable agreement with the data $|U_{\mu 3}|$ was greater than 0.95.

Table 7.3 shows the inputs and estimates of one of the better trajectories. We can see that again the values of R_0, θ_0 and ϕ_0 are close to the $F3_2$ fixed point at $\mu = 250$ GeV, although θ_0 (1.21) is further away than in the trajectory with no QCD running. QCD running has the effect of, below the bottom quark mass, increasing the eigenvalues compared to their counterpart with no QCD running. A larger eigenvalue means that $\boldsymbol{\alpha}$ doesn't need such a large component in the direction of the state vector to give the same mass. This means that $\boldsymbol{\alpha}$ doesn't need to rotate so far from, e.g., $\mu = m_t$ to $\mu = m_c$, so $\boldsymbol{\alpha}(250\text{ GeV})$ can be further from the fixed point. The same reasoning lets us understand why the speed parameter, $\rho_S^2/16\pi^2$, is smaller when QCD running is included. The strange quark mass is similar to the case of no QCD running and is quite light.

The results still exhibit roughly the correct pattern of hierarchy, but there is still difficulty in making a close match. We can see that the charm mass is not so

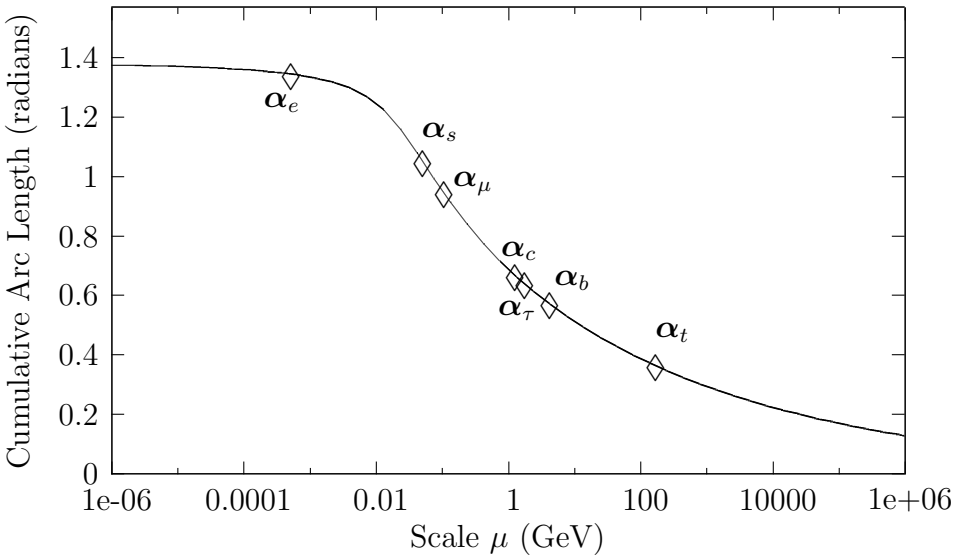

Figure 7.8: The cumulative arc length as the scale reduces from $\mu = \infty$ along the trajectory with QCD running, table 7.3. Diamonds denote the cumulative arc length at various scales.

well matched in this case, though agreement for the other masses is comparable. It did not seem possible to get a good charm quark mass whilst retaining all of the other quantities. The CKM matrix is a little better matched than without the QCD running. The top left 2×2 section is very well matched. The top right and bottom left corner elements still do not show good agreement. The value of $|U_{\mu 3}|$ is very large. Bearing in mind that it comes from the inner product of $\boldsymbol{\alpha}(m_\mu)$ and $\boldsymbol{\alpha}(m_{\nu_3})$ so here it's very close to its maximum value. The trajectory would need to be quite different to giving a significantly different value. The θ_{CP} angle is again of order 1.

Figure 7.7 shows the trajectory of $\boldsymbol{\alpha}$. Again we can see that the trajectory is very nearly planar. In line with the smaller value of θ_0, $\boldsymbol{\alpha}(m_t)$ is further from the $F3_2$ fixed point. We can see that the trajectory spans a larger distance on the sphere, which is responsible for the large $|U_{\mu 3}|$ associated with this trajectory. Figure 7.8 shows the cumulative arc length for this trajectory. We see that the overall behaviour is very similar to the trajectory with no QCD running. The points mentioned above can be seen in evidence here too. The larger value of $|U_{\mu 3}|$ is represented in the fact that the total arc length covered is around 1.4 radians, whereas in figure 7.3 it reached just over 1 radian. Also, the larger value of θ_0 at $\mu = 250$ GeV is represented by the fact that the trajectory reaches $\boldsymbol{\alpha}(m_t)$ after around 0.4 radians, whereas previously it was 0.2 radians.

7.3 Ambiguities in the FSM Metric

At the beginning of chapter 6 we described how the framons gives rise to the metric on flavour space. This process is not completely clear and there has been a suggestion [29] that the metric, given in equation (6.7), may be

$$g_{\tilde{a}\tilde{b}} = A \begin{pmatrix} \frac{1}{1+2R} & 0 & 0 \\ 0 & \frac{1}{1-R} & 0 \\ 0 & 0 & \frac{1}{1-R} \end{pmatrix} A^\dagger, \tag{7.9}$$

where A is the unitary transformation which gives

$$A\boldsymbol{\alpha}_0 = \boldsymbol{\alpha}. \tag{7.10}$$

Although we have not calculated the Christoffel symbols a reasonable guess at the parallel transport is

$$\mathbf{v}(\mu_2) = A_2 D_2^{-1} A_2^\dagger A_1 D_1 A_1^\dagger \mathbf{v}(\mu_1), \tag{7.11}$$

where $A_i = A(\mu_i)$,

$$D_i = \begin{pmatrix} \frac{1}{P_i} & 0 & 0 \\ 0 & \frac{1}{Q_i} & 0 \\ 0 & 0 & \frac{1}{Q_i} \end{pmatrix}, \tag{7.12}$$

$P_i = \sqrt{1+2R(\mu_i)}$ and $Q_i = \sqrt{1-R(\mu_i)}$. We can see that the inner product of two vectors remains independent of scale:

$$\begin{aligned} \langle \mathbf{u}_1, \mathbf{v}_1 \rangle &= \langle \mathbf{u}_1 | A_1 D_1^2 A_1^\dagger | \mathbf{v}_1 \rangle \\ &= \langle \mathbf{u}_2 | A_2 D_2 A_2^\dagger A_1 D_1^{-1} A_1^\dagger A_1 D_1^2 A_1^\dagger A_1 D_1^{-1} A_1^\dagger A_2 D_2 A_2^\dagger \mathbf{v}_2 \rangle \\ &= \langle \mathbf{u}_2 | A_2 D_2^2 A_2^\dagger | \mathbf{v}_2 \rangle \\ &= \langle \mathbf{u}_2, \mathbf{v}_2 \rangle, \end{aligned} \tag{7.13}$$

where we have used the fact that D is hermitian and A is unitary.

When applied to $\boldsymbol{\alpha}$ we find that this parallel transport alters the length, but not the orientation, of $\boldsymbol{\alpha}$:

$$\begin{aligned} \boldsymbol{\alpha}(\mu_2) &= A_2 D_2^{-1} A_2^\dagger A_1 D_1 A_1^\dagger \boldsymbol{\alpha}(\mu_1) \\ &= \frac{P_2}{P_1} \boldsymbol{\alpha}(\mu_1). \end{aligned} \tag{7.14}$$

When applied to the mass leakage scheme given in section 6.2, where all the vectors are normalised, the effect of the metric is removed. We have performed some preliminary studies without the metric and found it difficult to match the experimental data. If the proposed metric, equation (7.9), and parallel transport, equation (7.11), are to give a good match to experimental data then the scheme laid out in section 6.2 will need to be modified. The simplest modification is to remove the normalisation of $\boldsymbol{\alpha}$. This will not alter the shape of a given trajectory but will change the fermion masses, which receive their mass via an inner product with $\boldsymbol{\alpha}$.

7.4 Higgs Decay Revisited

In this section we will look at what the trajectories we have found predict for Higgs decay, in a similar vein to the first part. We will only consider the trajectory with no QCD running (i.e., table 7.2), but there is no substantial difference between the Higgs decay predictions for this trajectory than for the trajectory when QCD running is included. The Yukawa term is of the same form considered in part I. We will again consider ratios of branching ratios,

$$\frac{\Gamma(H \to x\bar{y})}{\Gamma(H \to b\bar{b})} = \frac{\rho_{T_x}^2}{\rho_D^2} \frac{|\mathbf{v}_x \cdot \boldsymbol{\alpha}_H|^2 |\mathbf{v}_y \cdot \boldsymbol{\alpha}_H|^2}{|\mathbf{v}_b \cdot \boldsymbol{\alpha}_H|^4}. \tag{7.15}$$

As we explained earlier, when considering masses and mixing angles we can use only the left handed fields. However, when considering Higgs decay we have to use the full wavefunction, not just the left handed state vectors. This means we have to be much more precise in considering the effect of the chiral transformation. Here, however, since we are only interested in order of magnitude predictions of Higgs decay we will take the simplest approach and remove the chiral transformation. This will have the effect of rendering our state vectors real and removing the CP violation in the CKM matrix. In the first section we used real vectors coming from the fitted trajectory. This was effectively the same approximation.

We can estimate the error introduced by removing the CP violation in the CKM matrix. Using the usual parameterisation

$$V_{\text{CKM}} = \begin{pmatrix} c_{12}c_{13} & s_{12}c_{13} & s_{13}e^{-i\delta} \\ -s_{12}c_{23} - c_{12}s_{23}s_{13}e^{i\delta} & c_{12}c_{23} - s_{12}s_{23}s_{13}e^{-i\delta} & s_{23}c_{13} \\ s_{12}s_{23} - c_{12}c_{23}s_{13}e^{i\delta} & -c_{12}s_{23} - s_{12}c_{23}s_{13}e^{i\delta} & c_{23}c_{13} \end{pmatrix}, \tag{7.16}$$

and the experimental absolute values [24] we can see that $\sin\theta_{12} \approx 0.2$, $\sin\theta_{23} \approx 0.04$ and $\sin\theta_{13} \approx 0.004$. There are four terms which are the sum of two parts, one of

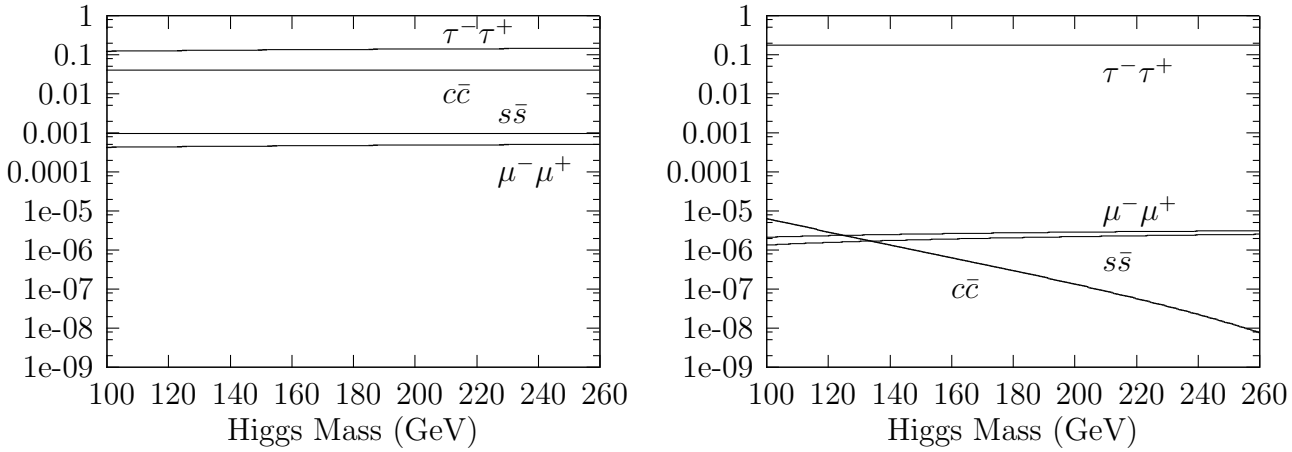

Figure 7.9: $\Gamma(H \to x\bar{x})/\Gamma(H \to b\bar{b})$ for various final state particles as predicted by the standard model (left, a) and the FSM (right, b).

which depends on the phase, δ. Except for the bottom-left term the absolute value of each component is dominated by the term which does not depend on the phase. Since $s_{12}s_{23} \approx 0.008$ and $|V_{td}| = 0.00862$ the absolute value of the bottom-left element is well approximated by the term which does not depend on phase. Setting $\delta = 0$ then introduces an error less than 2% in all elements except the bottom-left element where the error is less than 10%.

In figure 7.9a we see again the standard model predictions for Higgs decay. Figure 7.9b show the corresponding predictions from the FSM. We can see that the conclusions from part I are reproduced here. The branching ratio to $\tau^-\tau^+$ is similar to that in the standard model while that to $s\bar{s}$ and $\mu^-\mu^+$ are around a factor of 10^3 smaller. The branching ratio to $c\bar{c}$ is between 10^4 and 10^7 times smaller, depending on the Higgs mass.

Again the scheme predicts flavour violating decays. These are in agreement with the general predictions in part I, except $\Gamma(H \to c\bar{u})/\Gamma(H \to b\bar{b})$ is considerably higher for a low mass Higgs. Here it ranges between 10^{-6} for a low mass Higgs to 10^{-9} for a 260 GeV Higgs boson.

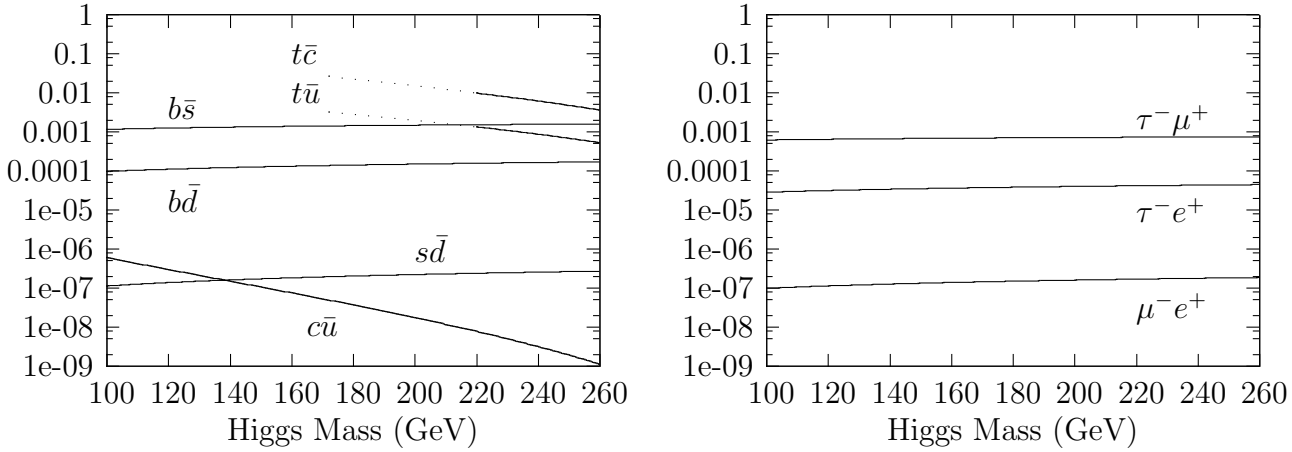

Figure 7.10: $\Gamma(H \to x\bar{y})/\Gamma(H \to b\bar{b})$ for various flavour violating decays as predicted by the FSM. Note that $\Gamma(H \to y\bar{x}) = \Gamma(H \to x\bar{y})$. Below around 220 GeV, indicated by the dotted lines, threshold effects will influence the $t\bar{c}$ and $t\bar{u}$ decay modes.

Part III

The FSM Framon Mass Spectrum

Chapter 8

Finding the Framon Mass Spectrum in the Hermitian Gauge

In this section we find the strong framon mass matrix using the hermitian gauge. We use the vacuum of the framon potential and discover that none of the framon fields are massless. We do not find the eigenvalues in terms of the coupling constants of the theory as the resulting expressions are too complicated to be useful analytically. We find the masses are in agreement with those calculated in the triangular gauge, as expected.

We recall that the framon potential was given by

$$\begin{aligned} V[\Phi] &= -\mu_W|\phi|^2 + \lambda_W(|\phi|^2)^2 \\ &\quad -\mu_S\sum_a|\phi_a|^2 + \lambda_S\left(\sum_a|\phi_a|^2\right)^2 + \kappa_S\sum_{a,b}|(\phi_a^*\cdot\phi_b)|^2 \\ &\quad +\nu_1|\phi|^2\sum_a|\phi_a|^2 - \nu_2|\phi|^2\sum_a|(\boldsymbol{\alpha}^*\cdot\phi_a)|^2. \end{aligned} \tag{8.1}$$

In [2, 19] the vacuum of this potential is found. It has an invariance, parameterised by $\boldsymbol{\alpha}$, and satisfies the following vacuum equations:

$$3\mu_S = 6\lambda_S\zeta_S^2 + 3\nu_1\zeta_W^2 + 2\kappa_S\zeta_S^2 - \nu_2\zeta_W^2, \tag{8.2}$$

$$6\lambda_W\zeta_W^2 = 3\mu_W - 3\nu_1\zeta_S^2 + \nu_2\zeta_S^2(1+2R), \tag{8.3}$$

where

$$R = \frac{\nu_2\zeta_W^2}{2\kappa_S\zeta_S^2}. \tag{8.4}$$

In the $(H, \boldsymbol{\alpha}_0, \boldsymbol{\alpha}_0)$ set up we can write fluctuations around the vacuum as

$$\phi^\dagger = (\zeta_W + H, 0, 0) \tag{8.5}$$

for the weak framon field and

$$\Phi = \begin{pmatrix} X + c_1 & a_1 + ib_1 & a_2 + ib_2 \\ a_1 - ib_1 & Y + c_2 & a_3 + ib_3 \\ a_2 - ib_2 & a_3 - ib_3 & Y + c_3 \end{pmatrix} \tag{8.6}$$

for the strong framon field, where

$$X = \zeta_S \sqrt{\frac{1+2R}{3}}, \tag{8.7}$$

$$Y = \zeta_S \sqrt{\frac{1-R}{3}}. \tag{8.8}$$

To simplify calculations we will here choose the vacuum given by

$$\boldsymbol{\alpha}^\dagger = (1, 0, 0), \tag{8.9}$$

but the results will be independent of the vacuum chosen. We will now substitute these fields into the potential and write only the terms which are quadratic in the fluctuations,

$$-\mu_W |\phi|^2 \Big|_{\text{Quad}} = -\mu_W H^2, \tag{8.10}$$

$$\lambda_W (|\phi|^2)^2 \Big|_{\text{Quad}} = 6\lambda_W \zeta_W^2 H^2, \tag{8.11}$$

$$-\mu_S \sum_a |\phi_a|^2 \Big|_{\text{Quad}} = -\mu_S \sum_i c_i^2 + 2(a_i^2 + b_i^2), \tag{8.12}$$

$$\begin{aligned} \lambda_S \left(\sum_a |\phi_a|^2 \right)^2 \Big|_{\text{Quad}} = \lambda_S \Bigg(& 2(X^2 + 2Y^2) \left[\sum_i c_i^2 + 2(a_i^2 + b_i^2) \right] + \\ & + 4(X^2 c_1^2 + Y^2 (c_s^2 + c_3^2)) + \\ & + 8(XY c_1 c_2 + XY c_1 c_3 + Y^2 c_2 c_3) \Bigg), \end{aligned} \tag{8.13}$$

$$\kappa_S \sum_{a,b} |(\phi_a^* \cdot \phi_b)|^2 \Big|_{\text{Quad}} = 4\kappa_S \Big(X^2 a_1^2 + XY a_1^2 + X^2 b_1^2 + XY b_1^2 + Y^2 a_1^2 + Y^2 b_1^2 + \\ + X^2 a_2^2 + XY a_2^2 + X^2 b_2^2 + XY b_2^2 + Y^2 a_2^2 + Y^2 b_2^2 + \\ + Y^2 a_3^2 + Y^2 a_3^2 + Y^2 b_3^2 + Y^2 b_3^2 + Y^2 a_3^2 + Y^2 b_3^2 + \\ + \frac{3}{2}(X^2 c_1^2 + Y^2 c_2^2 + Y^2 c_3^2) \Big), \tag{8.14}$$

$$\nu_1 |\phi|^2 \sum_a |\phi_a|^2 \Big|_{\text{Quad}} = \nu_1 \Bigg(\zeta_W^2 \left[\sum_i c_i^2 + 2(a_i^2 + b_i^2) \right] + 4\zeta_W H (X c_1 + Y c_2 + Y c_3) + \\ + H^2 (X^2 + 2Y^2) \Bigg), \tag{8.15}$$

$$-\nu_2 |\phi|^2 \sum_a |\boldsymbol{\alpha}^* \cdot \phi_a|^2 \Big|_{\text{Quad}} = -\nu_2 \Big(\zeta_W^2 (c_1^2 + a_1^2 + b_1^2 + a_2^2 + b_2^2) + 4X\zeta_W H c_1 + X^2 H^2 \Big). \tag{8.16}$$

We can extract from these the terms quadratic in the fluctuations. For example, the coefficient for the H^2 term is

$$\begin{aligned} H^2 : & -\mu_W + 6\lambda_W \zeta_W^2 + \nu_1 (X^2 + 2Y^2) - \nu_2 X^2 \\ & = -\mu_W + 6\lambda_W \zeta_W^2 + \nu_1 \zeta_S^2 - \nu_2 \zeta_S^2 \frac{1+2R}{3} \\ & = 4\lambda_W \zeta_W^2, \end{aligned} \tag{8.17}$$

where we have used vacuum equation (8.3) to obtain the last line. We can see that these fluctuations are not eigenvalues of the mass matrix as some off diagonal coefficients are non-zero, e.g.,

$$\begin{aligned} H c_1 : & 4\nu_1 \zeta_W X - \nu_2 4\zeta_W X \\ & = 4\nu_1 \zeta_W \zeta_S \sqrt{\frac{1+2R}{3}} - 4\nu_2 \zeta_W \zeta_S \sqrt{\frac{1+2R}{3}} \\ & = 4(\nu_1 - \nu_2) \zeta_W \zeta_S \sqrt{\frac{1+2R}{3}}. \end{aligned} \tag{8.18}$$

We also write the coefficient for a_1^2,

$$
\begin{aligned}
a_1^2 :\ & -2\mu_S + \lambda_S 4(X^2+2Y^2) + \kappa_S(4X^2+4XY+4Y^2) + 2\nu_1\zeta_W^2 - \nu_2\zeta_W^2 \\
&= -2\mu_S + 4\lambda_S\zeta_S^2 + 2\kappa_S\zeta_S^2\frac{4+2R+2\sqrt{(1+2R)(1-R}}{3} + 2\nu_1\zeta_W^2 - \nu_2\zeta_W^2 \\
&= 2\kappa_S\zeta_S^2\frac{2+2R+2\sqrt{(1+2R)(1-R}}{3} - \frac{1}{3}\nu_2\zeta_W^2 \\
&= 2\kappa_S\zeta_S^2\frac{2+R+2\sqrt{(1+2R)(1-R}}{3}, \qquad (8.19)
\end{aligned}
$$

where we have used the vacuum equation (8.2) and the expression for R, equation (8.4).

Now, we note that when we introduced the fluctuations in equation (8.6) we did not ensure that they were normalised. We must now do this, in a similar manner to our treatment of the strong framon fields in the triangular gauge in section 5.2. The orthonormal fields are

$$
\Phi = \begin{pmatrix} X+\delta\phi_1^{\tilde{1}} & \delta\phi_1^{\tilde{2}} & \delta\phi_1^{\tilde{3}} \\ \delta\phi_2^{\tilde{1}} & Y+\delta\phi_2^{\tilde{2}} & \delta\phi_2^{\tilde{3}} \\ \delta\phi_3^{\tilde{1}} & \delta\phi_3^{\tilde{2}} & Y+\delta\phi_3^{\tilde{3}} \end{pmatrix}. \qquad (8.20)
$$

To put these in the $(H, \boldsymbol{\alpha}_0, \boldsymbol{\alpha}_0)$ set up we need to act on the left with

$$
\Omega = \begin{pmatrix} 1-\frac{i}{X}\delta\phi_{1I}^{\tilde{1}} & -\frac{1}{X+Y}(\delta\phi_1^{\tilde{2}} - \delta\phi_2^{\tilde{1}*}) & -\frac{1}{X+Y}(\delta\phi_1^{\tilde{3}} - \delta\phi_3^{\tilde{1}*}) \\ -\frac{1}{X+Y}(\delta\phi_2^{\tilde{1}} - \delta\phi_1^{\tilde{2}*}) & 1-\frac{i}{Y}\delta\phi_{2I}^{\tilde{2}} & -\frac{1}{X+Y}(\delta\phi_2^{\tilde{3}} - \delta\phi_3^{\tilde{2}*}) \\ -\frac{1}{X+Y}(\delta\phi_3^{\tilde{1}} - \delta\phi_1^{\tilde{3}*}) & -\frac{1}{X+Y}(\delta\phi_3^{\tilde{2}} - \delta\phi_2^{\tilde{3}*}) & 1-\frac{i}{Y}\delta\phi_{3I}^{\tilde{3}} \end{pmatrix}, \qquad (8.21)
$$

so then

$$
\tilde{a}_1 = \frac{X}{X+Y}\delta\phi_{1R}^{\tilde{2}} + \frac{Y}{X+Y}\delta\phi_{2R}^{\tilde{1}}. \qquad (8.22)
$$

To normalise we fix

$$
\begin{aligned}
\tilde{a}_1^2 &= \frac{X^2+Y^2}{(X+Y)^2}a_1^2 \\
&= \frac{2+R}{2+R+2\sqrt{1+2R}\sqrt{1-R}}a_1^2. \qquad (8.23)
\end{aligned}
$$

We then get the coefficient for $\tilde{a}_1^2$ to be

$$\tilde{a}_1^2 : 2\kappa_S\zeta_S^2\frac{2+R}{3}. \tag{8.24}$$

Performing similar steps for all of the fields results in the framon mass matrix,

$$\begin{pmatrix} 4\lambda_W\zeta_W^2 & 2\zeta_W\zeta_S(\nu_1-\nu_2)\sqrt{\frac{1+2R}{3}} & 2\zeta_W\zeta_S\nu_1\sqrt{\frac{1-R}{3}} & 2\zeta_W\zeta_S\nu_1\sqrt{\frac{1-R}{3}} & 0 \\ * & 4(\kappa_S+\lambda_S)\zeta_S^2(\frac{1+2R}{3}) & 4\lambda_S\zeta_S^2\frac{\sqrt{(1+2R)(1-R)}}{3} & 4\lambda_S\zeta_S^2\frac{\sqrt{(1+2R)(1-R)}}{3} & 0 \\ * & * & 4(\kappa_S+\lambda_S)\zeta_S^2(\frac{1-R}{3}) & 4\lambda_S\zeta_S^2(\frac{1-R}{3}) & 0 \\ * & * & * & 4(\kappa_S+\lambda_S)\zeta_S^2(\frac{1-R}{3}) & 0 \\ 0 & 0 & 0 & 0 & A \end{pmatrix}, \tag{8.25}$$

where

$$A = \begin{pmatrix} 4\kappa_S\zeta_S^2(\frac{1-R}{3}) & 0 & 0 & 0 & 0 & 0 \\ 0 & 4\kappa_S\zeta_S^2(\frac{1-R}{3}) & 0 & 0 & 0 & 0 \\ 0 & 0 & 2\kappa_S\zeta_S^2(\frac{2+R}{3}) & 0 & 0 & 0 \\ 0 & 0 & 0 & 2\kappa_S\zeta_S^2(\frac{2+R}{3}) & 0 & 0 \\ 0 & 0 & 0 & 0 & 2\kappa_S\zeta_S^2(\frac{2+R}{3}) & 0 \\ 0 & 0 & 0 & 0 & 0 & 2\kappa_S\zeta_S^2(\frac{2+R}{3}) \end{pmatrix} \tag{8.26}$$

and a * denotes the corresponding transpose element as the matrix is symmetric.

We do not diagonalise the framon mass matrix as the resulting expressions are too complicated to be useful. It can be done analytically since a unitary transformation with

$$\begin{pmatrix} 1 & 0 & 0 & 0 & 0 \\ 0 & 1 & 0 & 0 & 0 \\ 0 & 0 & \frac{1}{\sqrt{2}} & \frac{1}{\sqrt{2}} & 0 \\ 0 & 0 & \frac{1}{\sqrt{2}} & -\frac{1}{\sqrt{2}} & 0 \\ 0 & 0 & 0 & 0 & \mathbf{1} \end{pmatrix} \tag{8.27}$$

diagonalises all but the top left 3×3 part. We can see, however, that all of the framons are massive, so no experimental data is immediately violated.

The calculation in the hermitian gauge agrees, as expected, with the equivalent calculation in the triangular gauge [2]. This mass matrix can be used to put necessary and sufficient conditions on the coupling constants for positive framon masses [2]. When all of the coupling constants are unity these conditions are satisfied.

Part IV

Conclusions

Chapter 9

Conclusions

9.1 Conclusions: Part I

In the first part of this thesis we defined a rank-one rotating mass matrix and described the mass leakage mechanism. We went on to discuss a solution to the strong CP problem in this setting. We were then in a position to ask whether the scheme is consistent with experimental results. To answer this question we reversed the mass leakage scheme, so we could restrict the trajectory of $\boldsymbol{\alpha}$ with experimental data, and outlined a parameter space search technique to fit a smooth trajectory for $\boldsymbol{\alpha}$.

We found that the general rank-one rotating mass matrix hypothesis with the strong CP solution is consistent with the experimental CKM matrix, including the CP violating phase. The $\boldsymbol{\alpha}_x$'s can be placed on a smooth trajectory, modelled with a cubic fit on the stereographic projection, so that they give the correct masses for all but the light quarks. Fitting the Jarlskog invariant gives a θ_{CP} of 1.45 radians. As the strong coupling constant, α_s, is larger than 1 below 1 GeV it is unclear how the experimentally measured masses of the lightest quarks relate to the definition of masses within the mass leakage mechanism. The strange quark has an intermediate mass and does not fit perfectly into this scheme, but it may be heavy enough to give us some insight into how we should treat the light quarks.

We have found that for the heavy quarks and the charged leptons a simple exponential fit can model the cumulative arc length for scales above m_μ, though it is unlikely to be a realistic fit below this scale. This behaviour has previously been captured by both a phenomenological model (DSM [7]) and a field theory (FSM [19]), which have rotating mass matrices and predict fixed points in the rotation at $\mu = 0$ and $\mu = \infty$.

Since we do not know neutrino masses with sufficient accuracy, whether neutrino oscillations violate CP symmetry, nor whether they are Majorana particles we cannot

place constraints on $\boldsymbol{\alpha}(\mu)$ using neutrino data.

The cubic best fit line and the exponential cumulative arc length fit allowed us to predict branching ratios for a range of Higgs masses. These give large $H \to c\bar{c}$ suppression, in line with a previous planar approximation [13], along with $\mu^-\mu^+$ and $s\bar{s}$ suppression. The scheme generically predicts flavour violating decays. We find a notable branching ratio to $\tau^-\mu^+$ and give estimates for other flavour violating decays. The level of flavour violation seen has been shown to be consistent with experimental bounds [13].

9.2 Conclusions: Part II

In the second part we studied the framed standard model and derived the strong framon one-loop contribution to the mass matrix rotation. The resulting RGE has one low scale fixed point and two high scale fixed points. The unconstrained sign of a coupling constant, ν_2, determines which high scale fixed point the trajectory is attracted to. There is also an unstable fixed point.

The framing of the standard model led to a metric on the internal symmetry space, which modified the mass leakage mechanism from part I. We calculated the new procedure in the presence of the non-trivial metric. We went on to consider the possible effects of QCD running on the mass leakage mechanism.

We then used a lattice scan and simplex optimisation to search the parameter space of constants of integration for the RGE and coupling constant values to find the rotation of the mass matrix which best matched experimental data. We also allowed the strange quark mass to vary from 0.03 GeV to 0.4 GeV due to the difficulties arising from the strong coupling nature of QCD below 1 GeV.

Preliminary studies showed that the experimental data is better matched with $\nu_2 > 0$. Ignoring any QCD effects we found that the general hierarchical behaviour seen in experiments could be reproduced. It was not possible to match the experimental values exactly, but this may be expected as we have only considered one one-loop contribution to the rotation. However, the charm quark mass, the muon mass and the CKM matrix showed good agreement with the experimental values. We found a large but plausible value for $|U_{\mu 3}|$ of 0.82 and fit the Jarlskog invariant with a θ_{CP} of 0.28 radians. We found that the trajectory passes from the high scale fixed point to the low scale fixed point along an almost planar trajectory which does not pass near the unstable fixed point. The cumulative arc length showed a $\tanh(\ln \mu)$ like behaviour.

We compared this trajectory to the results from the top down approach taken in the first part of this thesis. We found that there was good agreement between the trajectories in the high scale region, above $\mu = m_c$. The position of $\boldsymbol{\alpha}(m_s)$ was quite different as the masses assumed for each result was quite different. At lower scales the two trajectories diverged. There are two factors contributing to this. Firstly, as there are not many fermions we were restricted, in the first part, to fitting the trajectory with a cubic fit on the stereographic projection. Though this can model the behaviour well for a small range of scales, as the range increases the fit gets considerably worse. The relation between the quark and lepton sectors cannot be constrained by experiment so a large amount of curvature can be introduced in relating the two. Secondly, since the tightest experimental constraints are placed on the one-loop RGE between $\mu = m_c$ and $\mu = m_t$, as we move outside of this range higher order effects begin to make large contributions to the trajectory.

When QCD running was introduced the general hierarchy was retained but the accuracy of the details was not improved. The best trajectory found roughly reproduced the fermion masses and the CKM matrix, but the trajectory was very long resulting in a large $|U_{\mu 3}|$ of 0.97. Taking $\theta_{CP} = 0.31$ radians fit the Jarlskog invariant.

The predictions for Higgs decay from the trajectory ignoring QCD running were similar to those found in part I. There is a large (greater than a factor of 10^4) suppression in the $H \to c\bar{c}$ decay mode compared to the standard model. The $H \to s\bar{s}$ and $H \to \mu^-\mu^+$ modes are also suppressed. Flavour violating modes are also predicted in line with that seen in part I. There is still a large branching ratio to $\tau^-\mu^+$ and τ^-e^+ which may be detectable in experiments.

9.3 Conclusions: Part III

In the final part we expand around the framon vacuum to find the framon mass matrix in the Hermitian gauge. The resulting spectrum is in agreement with the spectrum found in the triangular gauge [2]. We find that all of the framons are massive.

9.4 Overall Conclusions and Outlook

In summary, we have found that the rank-one rotating mass matrix hypothesis augmented with the strong CP solution can, from both a generic and a model dependent point of view, give a good account of the hierarchy seen in fermion masses and mixing angles. We have found that the strong CP solution suggests that θ_{CP} is of

order unity, as expected on naturalness grounds, and introduces a KM phase into the CKM matrix. Without the strong CP solution the hypothesis has, historically, had difficulties in accounting for the KM phase. We find that the scheme predicts a suppression of $\Gamma(H \to c\bar{c})$ and non-zero flavour violating Higgs decays, including a sizable $H \to \tau^- \mu^+$ branching ratio. These features will, in time, be tested at the LHC.

We were forced to exclude almost all of the data coming from the neutrino sector. As terrestrial, solar and cosmological neutrino experiments become more sensitive we can start to utilise these constraints. If neutrinos have a Majorana mass term then this will need to be incorporated into the mass leakage mechanism. Improved neutrino data would also provide a motivation for increasing the range of applicability of the mass matrix RGE in the FSM, so it can be trusted at lower scales. This would require a more careful consideration of all of the contributions to the RGE and calculation to higher loop order.

Appendix A

Some Ancillary Calculations

In this appendix we present some algebra necessary for results in section 5.7. In that section we need to calculate $\sum_j \langle v_j|v_j\rangle$, $\sum_{j=1\ldots6}\langle v_0|v_j\rangle|v_j\rangle$ and $|gvI\rangle := \sum_{j=7,8,9}\langle v_0|v_j\rangle|v_j\rangle$.

A.1 $\sum_j \langle v_j|v_j\rangle$

Using equations (5.83) to (5.91) we can write

$$\begin{aligned}\sum_j \langle v_j|v_j\rangle &= \cos\theta^2 + \frac{\cos^2\theta\sin^2\theta\sin^2\phi}{\cos^2\theta+\sin^2\theta\cos^2\phi} + \frac{\sin^2\theta\cos^2\phi}{\cos^2\theta+\sin^2\theta\cos^2\phi} + \\ &+ \frac{\sin^2\theta\cos^2\phi}{2(\cos^2\theta+\sin^2\theta\cos^2\phi)} + \frac{\cos^2\theta\sin^2\theta\sin^2\phi}{2(\cos^2\theta+\sin^2\theta\cos^2\phi)} + \\ &+ \frac{1+2R}{2+R}\frac{\sin^2\theta\cos^2\phi}{\cos^2\theta+\sin^2\theta\cos^2\phi} + \frac{1-R}{2+R}\cos^2\theta + \\ &+ \frac{1+2R}{2+R}\frac{\cos^2\theta\sin^2\theta\sin^2\phi}{\cos^2\theta+\sin^2\theta\cos^2\phi} + \frac{1-R}{2+R}\cos^2\theta \\ &= \frac{3}{2+R}(1+1+2R-3R\cos^2\theta). \end{aligned} \tag{A.1}$$

We will introduce $E = 1+2R-3R\cos^2\theta$ to simplify the RGE, so then

$$\sum_j \langle v_j|v_j\rangle = \frac{3}{2+R}(1+E). \tag{A.2}$$

A.2 $\sum_{j=1\ldots6}\langle v_0|v_j\rangle|v_j\rangle$

Using equation (5.77), equations (5.83) to (5.91) and (5.92) to (5.94) we will first write down $\langle v_0|v_j\rangle$:

$$\langle v_0|v_1\rangle = \sqrt{\frac{1+2R}{3}}\cos^2\theta, \tag{A.3}$$

$$\langle v_0|v_2\rangle = \sqrt{\frac{1-R}{3}}\frac{\cos^2\theta\sin^2\theta\sin^2\phi}{\cos^2\theta+\sin^2\theta\cos^2\phi}, \tag{A.4}$$

$$\langle v_0|v_3\rangle = \sqrt{\frac{1-R}{3}}\frac{\sin^2\theta\cos^2\phi}{\cos^2\theta+\sin^2\theta\cos^2\phi}, \tag{A.5}$$

$$\langle v_0|v_4\rangle = -\sqrt{\frac{2+R}{3}}\frac{\cos^2\theta\sin\theta\sin\phi}{\sqrt{\cos^2\theta+\sin^2\theta\cos^2\phi}}, \tag{A.6}$$

$$\langle v_0|v_5\rangle = -\sqrt{\frac{2+R}{3}}\frac{\cos\theta\sin\theta\cos\phi}{\sqrt{\cos^2\theta+\sin^2\theta\cos^2\phi}}, \tag{A.7}$$

$$\langle v_0|v_6\rangle = \sqrt{\frac{2-2R}{3}}\frac{\cos\theta\sin^2\theta\sin\phi\cos\phi}{\cos^2\theta+\sin^2\theta\cos^2\phi}. \tag{A.8}$$

Looking at each component we then obtain,

$$\begin{aligned}\left(\sum_{j=1\ldots6}\langle v_0|v_j\rangle|v_j\rangle\right)_1 &= \sqrt{\frac{1+2R}{3}}\cos^3\theta e^{i\beta_1} + \sqrt{\frac{1+2R}{3}}\frac{\cos^3\theta\sin^2\theta\sin^2\phi e^{i\beta_1}}{\cos^2\theta+\sin^2\theta\cos^2\phi}+\\ &\quad+\sqrt{\frac{1+2R}{3}}\frac{\cos\theta\sin^2\theta\cos^2\phi e^{i\beta_1}}{\cos^2\theta+\sin^2\theta\cos^2\phi}\\ &= \sqrt{\frac{1+2R}{3}}\cos\theta e^{i\beta_1}\\ &= |v_0\rangle_1,\end{aligned} \tag{A.9}$$

$$\begin{aligned}\left(\sum_{j=1\ldots6}\langle v_0|v_j\rangle|v_j\rangle\right)_2 &= -\sqrt{\frac{1-R}{3}}\frac{\cos^3\theta\sin^3\theta\sin^3\phi e^{i(\beta_1-\beta_2)}}{(\cos^2\theta+\sin^2\theta\cos^2\phi)^{\frac{3}{2}}}+\\ &\quad-\sqrt{\frac{1-R}{3}}\frac{\cos^3\theta\sin\theta\sin\phi e^{i(\beta_1-\beta_2)}}{\sqrt{\cos^2\theta+\sin^2\theta\cos^2\phi}}+\\ &\quad-\sqrt{\frac{1-R}{3}}\frac{\cos\theta\sin^3\theta\sin\phi\cos^2\phi e^{i(\beta_1-\beta_2)}}{(\cos^2\theta+\sin^2\theta\cos^2\phi)^{\frac{3}{2}}}\\ &= -\sqrt{\frac{1-R}{3}}\frac{\cos\theta\sin\theta\sin\phi e^{i(\beta_1-\beta_2)}}{\sqrt{\cos^2\theta+\sin^2\theta\cos^2\phi}}\\ &= |v_0\rangle_2,\end{aligned} \tag{A.10}$$

$$\left(\sum_{j=1...6}\langle v_0|v_j\rangle|v_j\rangle\right)_3 = -\sqrt{\frac{1-R}{3}}\frac{\sin^3\theta\cos^3\phi e^{-i\beta_3}}{(\cos^2\theta+\sin^2\theta\cos^2\phi)^{\frac{3}{2}}}+$$
$$-\sqrt{\frac{1-R}{3}}\frac{\cos^2\theta\sin\theta\cos\phi e^{-i\beta_3}}{\sqrt{\cos^2\theta+\sin^2\theta\cos^2\phi}}+$$
$$-\sqrt{\frac{1-R}{3}}\frac{\cos^2\theta\sin^3\theta\sin^2\phi\cos\phi e^{-i\beta_3}}{(\cos^2\theta+\sin^2\theta\cos^2\phi)^{\frac{3}{2}}}$$
$$= -\sqrt{\frac{1-R}{3}}\frac{\sin\theta\cos\phi e^{-i\beta_3}}{\sqrt{\cos^2\theta+\sin^2\theta\cos^2\phi}}$$
$$= |v_0\rangle_3. \tag{A.11}$$

We thus have that

$$\sum_{j=1...6}\langle v_0|v_j\rangle|v_j\rangle = |v_0\rangle. \tag{A.12}$$

A.3 $\sum_{j=7,8,9}\langle v_0|v_j\rangle|v_j\rangle$, the Governing Vector

The governing vector is given by

$$|gvI\rangle = \sum_{j=7,8,9}\langle v_0|v_j\rangle|v_j\rangle. \tag{A.13}$$

We will first calculate $\langle v_0|v_j\rangle$:

$$\langle v_0|v_7\rangle = i\frac{[(1-R)-(1+2R)]}{\sqrt{3(2+R)}}\frac{\cos^2\theta\sin\theta\sin\phi}{\sqrt{\cos^2\theta+\sin^2\theta\cos^2\phi}}$$
$$= -i\frac{3R}{\sqrt{3(2+R)}}\frac{\cos^2\theta\sin\theta\sin\phi}{\sqrt{\cos^2\theta+\sin^2\theta\cos^2\phi}}, \tag{A.14}$$

$$\langle v_0|v_8\rangle = i\frac{[(1-R)-(1+2R)]}{\sqrt{3(2+R)}}\frac{\cos\theta\sin\theta\cos\phi}{\sqrt{\cos^2\theta+\sin^2\theta\cos^2\phi}}$$
$$= -i\frac{3R}{\sqrt{3(2+R)}}\frac{\cos\theta\sin\theta\cos\phi}{\sqrt{\cos^2\theta+\sin^2\theta\cos^2\phi}}, \tag{A.15}$$

$$\langle v_0|v_9\rangle = i\left(\sqrt{\frac{1-R}{6}}-\sqrt{\frac{1-R}{6}}\right)\frac{\cos\theta\sin^2\theta\cos\phi\sin\phi}{\cos^2\theta+\sin^2\theta\cos^2\phi}$$
$$= 0. \tag{A.16}$$

We can now write

$$
\begin{aligned}
|gvI\rangle &= \sum_{j=7,8,9} \langle v_0|v_j\rangle |v_j\rangle \\
&= \langle v_0|v_7\rangle |v_7\rangle + \langle v_0|v_8\rangle |v_8\rangle \\
&= \begin{pmatrix} -\frac{3R}{2+R}\sqrt{\frac{1+2R}{3}}\cos\theta\sin^2\theta e^{i\beta_1} \\ -\frac{3R}{2+R}\sqrt{\frac{1-R}{3}}\frac{\cos^3\theta\sin\theta\sin\phi}{\sqrt{\cos^2+\sin^2\theta\cos^2\phi}}e^{i\beta_1-i\beta_2} \\ -\frac{3R}{2+R}\sqrt{\frac{1-R}{3}}\frac{\cos^2\theta\sin\theta\cos\phi}{\sqrt{\cos^2+\sin^2\theta\cos^2\phi}}e^{-i\beta_3} \end{pmatrix} \\
&= -\frac{3R\sin\theta\cos\theta}{2+R}\begin{pmatrix} \sqrt{\frac{1+2R}{3}}\sin\theta e^{i\beta_1} \\ \sqrt{\frac{1-R}{3}}\frac{\cos^2\theta\sin\phi}{\sqrt{\cos^2+\sin^2\theta\cos^2\phi}}e^{i\beta_1-i\beta_2} \\ \sqrt{\frac{1-R}{3}}\frac{\cos\theta\cos\phi}{\sqrt{\cos^2+\sin^2\theta\cos^2\phi}}e^{-i\beta_3} \end{pmatrix}. \qquad \text{(A.17)}
\end{aligned}
$$

Bibliography

[1] C. Amsler et al. Review of Particle Physics. *Phys.Lett.B*, **667**, 1 (2008) and 2009 partial update for the 2010 edition.

[2] Michael J. Baker, José Bordes, Chan Hong-Mo, and Tsou Sheung Tsun. Developing the Framed Standard Model. In preperation.

[3] Michael J. Baker, José Bordes, Chan Hong-Mo, and Tsou Sheung Tsun. Mass Hierarchy, Mixing, CP-Violation and Higgs Decay – or Why Rotation is Good for Us. 2011. arXiv: 1103.5615.

[4] Michael J. Baker and Tsou Sheung Tsun. The Rotating Mass Matrix, the Strong CP Problem and Higgs Decay. *Eur.Phys.J.*, **C70**:1009–1015, 2010.

[5] Tom Banks and Eliezer Rabinovici. Finite Temperature Behavior of the Lattice Abelian Higgs Model. *Nucl. Phys.*, **B160**:349, 1979.

[6] Siegfried Bethke. The 2009 World Average of α_s. *Eur.Phys.J.*, **C64**:689–703, 2009.

[7] José Bordes, Chan Hong-Mo, Jacqueline Faridani, Jakov Pfaudler, and Tsou Sheung Tsun. CKM Matrix and Fermion Masses in the Dualized Standard Model. *Phys. Rev.*, **D58**:013004, 1998.

[8] José Bordes, Chan Hong-Mo, and Tsou Sheung Tsun. Fermion Mixing and Mass Hierarchy as Consequences of Mass Matrix Rotation. 2001. arXiv:hep-ph/0104036.

[9] José Bordes, Chan Hong-Mo, and Tsou Sheung Tsun. Implications of a Rotating Mass Matrix. *Phys. Rev.*, **D63**:016006, 2001.

[10] José Bordes, Chan Hong-Mo, and Tsou Sheung Tsun. Circumstantial Evidence for Rotating Mass Matrix From Fermion Mass and Mixing Data. *Eur. Phys. J.*, **C27**:189–200, 2003.

[11] José Bordes, Chan Hong-Mo, and Tsou Sheung Tsun. New Angle on the Strong CP and Chiral Symmetry Problems From a Rotating Mass Matrix. *Int.J.Mod.Phys.*, **A24**:101–112, 2009.

[12] José Bordes, Chan Hong-Mo, and Tsou Sheung Tsun. A Solution of the Strong CP Problem Transforming the theta-angle to the KM CP-violating Phase. *Int.J.Mod.Phys.*, **A25**:5897–5911, 2010.

[13] José Bordes, Chan Hong-Mo, and Tsou Sheung Tsun. Possible Anomalies in Higgs Decay: Charm Suppression and Flavour-Violation. *Eur.Phys.J.*, **C65**:537–542, 2010.

[14] T. P. Cheng, E. Eichten, and Ling-Fong Li. Higgs Phenomena in Asymptotically Free Gauge Theories. *Phys. Rev.*, **D9**:2259, 1974.

[15] K.G. Chetyrkin, Bernd A. Kniehl, and M. Steinhauser. Strong Coupling Constant with Flavor Thresholds at Four Loops in the MS Scheme. *Phys.Rev.Lett.*, **79**:2184–2187, 1997.

[16] Harald Fritzsch. Hierarchical Chiral Symmetries and the Quark Mass Matrix. *Phys.Lett.*, **B184**:391, 1987.

[17] Harald Fritzsch and Zhi-zhong Xing. Mass and Flavor Mixing Schemes of Quarks and Leptons. *Prog.Part.Nucl.Phys.*, **45**:1–81, 2000.

[18] Chan Hong-Mo and Tsou Sheung Tsun. Higgs Fields as Vielbeins of Internal Symmetry Space. 2006. arXiv: hep-ph/0611363.

[19] Chan Hong-Mo and Tsou Sheung Tsun. A Model Behind the Standard Model. *Eur. Phys. J.*, **C52**:635–663, 2007.

[20] C. Jarlskog. A Basis Independent Formulation of the Connection Between Quark Mass Matrices, CP Violation and Experiment. *Z.Phys.*, **C29**:491–497, 1985.

[21] Toshiaki Kaneko and Hirotaka Sugawara. Broken S_3 Symmetry in Flavor Physics. *Phys.Lett.*, **B697**:329–332, 2011.

[22] Ch. Kraus, B. Bornschein, L. Bornschein, J. Bonn, B. Flatt, et al. Final Results from Phase II of the Mainz Neutrino Mass Search in Tritium Beta Decay. *Eur.Phys.J.*, **C40**:447–468, 2005.

[23] Katherine J. Mack. Axions, Inflation and the Anthropic Principle. Submitted to *Phys. Rev. D.* 2009. Preprint arXiv:0911.0421.

[24] K. Nakamura et al. Review of Particle Physics. *J.Phys.G*, **G37**:075021, 2010.

[25] Th.M. Nieuwenhuizen. Do Non-Relativistic Neutrinos Constitute the Dark Matter? *Europhys.Lett.*, **86**:59001, 2009.

[26] R. D. Peccei and Helen R. Quinn. CP Conservation in the Presence of Instantons. *Phys. Rev. Lett.*, **38**:1440–1443, 1977.

[27] M. Spira. HDECAY version 3.51 (July 2009). Download available at http://people.web.psi.ch/spira/proglist.html.

[28] Gerard 't Hooft. *Acta Phys. Austr. Suppl. XXII*, page 531, 1980.

[29] Tsou Sheung Tsun. Private communication.

[30] T. van Ritbergen, J.A.M. Vermaseren, and S.A. Larin. The Four loop beta function in quantum chromodynamics. *Phys.Lett.*, **B400**:379–384, 1997.

[31] J.A.M. Vermaseren, S.A. Larin, and T. van Ritbergen. The Four Loop Quark Mass Anomalous Dimension and the Invariant Quark Mass. *Phys.Lett.*, **B405**:327–333, 1997.

[32] Steven Weinberg. The Quantum Theory of Fields. Vol. 2: Modern Applications. Cambridge, UK: Univ. Pr. (1996).

[33] Steven Weinberg. Perturbative Calculations of Symmetry Breaking. *Phys.Rev.*, **D7**:2887–2910, 1973.

[34] Steven Weinberg. A New Light Boson? *Phys.Rev.Lett.*, **40**:223–226, 1978.